# Leveraging the Rest-Ultraviolet and Rest-Optical Spectra of Star-Forming Galaxies at Redshifts $2 < z < 3$

Thesis by
Rachel Lauren Theios

In Partial Fulfillment of the Requirements for the
Degree of
Doctor of Philosophy


CALIFORNIA INSTITUTE OF TECHNOLOGY
Pasadena, California

2020
Defended June 1, 2020

Rachel Lauren Theios
ORCID: 0000-0002-4236-1037

*A long time ago in galaxies far, far away....*

# ACKNOWLEDGEMENTS

First and foremost, thank you to my advisor, Chuck Steidel—I could not have asked for a better mentor. You taught me that in astronomy (as in life), half the fun is just looking to see what's out there without knowing what you're going to find. I certainly didn't anticipate the direction this thesis would take, but I am glad I had an advisor who supported me through every roadblock (and there were many of them).

Thank you to my research group: to Allison, Ryan, and Gwen, for welcoming me into the world of observational astronomy, and every bit of advice and encouragement you've given me along the way. And thank you to Yuguang for helping me make sense of things when I got stuck, and humoring me on long observing nights when I started to get chatty. To the rest of my thesis committee: Evan Kirby, Lynne Hillenbrand, Chris Martin, and Phil Hopkins, thank you for all your valuable insight.

Thank you to my friends and colleagues at Caltech, who made my days here so much brighter. I've met so many amazing grad students over the years, both inside and outside of astronomy, who have provided me with the warmest and most supportive environment I could have asked for. Thank you to all my unofficial mentors: Scott, Donal, Nicha, and everyone else who showed me the ropes and gave me some much-needed perspective when I started to get tunnel vision. Thank you to Dillon, Mia, and Nitika for providing me with validation and support in all the right moments. Thank you to Marin, for all your friendship and support (and cat pictures). Thank you to my friends outside of astronomy: Peter, Ellen, Ellen, and Matt, for all the chill hangouts.

And thank you to my cohort, forever the cutest class of astronomy grads. Thank you to Denise, for all the homework help, companionship, and overall excellent advice you've provided me, even when I didn't think I needed it; and thank you to Jake, for sticking by my side through all the laughter and tears (sometimes both at the same time). I certainly wouldn't have made it this far without you both.

Thank you to Mackenzie, Sofia, and all of my fellow dancers in the Caltech Ballet Club. I've enjoyed every minute I've spent as your semi-fearless leader, and I hope I can keep dancing with you in the future.

Thank you to my friends outside of Caltech: Briana, Laurel, and Enrique, for always valuing me for who I was without judgment. I'm so glad we've stayed together even as our lives have taken different directions.

Thank you to my family for being a constant source of love and support in my life. Dad, you've always been there to throw me a life raft when I feel like I'm drowning, no matter how big or how small the crisis. Mom, you are the best listener I know and your unending love and empathy never ceases to amaze me. Jake, your perfect blend of compassion, common sense, and fun has helped me stay balanced and brightened so many of my dark moments.

And finally, to my two smallest and closest companions, Bailey and Juniper: I know you can't read this but I would be amiss if I didn't thank you anyway, so expect some cat treats in your near future. Thank you for all the joy, laughter, and unconditional love you've brought into my life. I wouldn't be here writing this without you.

# ABSTRACT

Galaxies at the peak of cosmic star formation ($z \sim 2-3$) are fundamentally different from local galaxies, in terms of the properties of their massive stellar populations and physical conditions in the interstellar medium (ISM). This thesis presents a detailed analysis of the stellar and nebular properties of high-redshift galaxies, using the rest-frame UV and rest-frame optical spectra of galaxies from the Keck Baryonic Structure Survey (KBSS), a large, targeted spectroscopic survey of galaxies at $z \sim 2-3$.

Chapter 2 compares inferences of dust attenuation, star formation, and metallicity from strong nebular emission lines, the far-UV continuum, and spectral energy distribution (SED) fits. These results indicate that the majority of high-redshift galaxies display different dust properties than those at low redshift, and that the assumption of a dust attenuation curve can dramatically change inferred properties such as star formation rates (SFRs). I find that SFRs estimated from H$\alpha$ and SED fitting only agree under specific combinations of assumptions, and caution that SFR calibrations established at low redshift do not apply at $z \sim 2-3$.

Chapter 3 utilizes rest-UV absorption lines to study the outflow kinematics of high-redshift galaxies. I compare several velocity metrics used in the literature, and search for correlations between outflow velocity and galaxy properties. These results are consistent with the picture of winds driven by momentum injected into the ISM by stellar feedback. I confirm that large-scale outflows are ubiquitous at high redshift due to these galaxies' high SFRs and compact sizes.

Finally, Chapter 4 analyzes the systematic uncertainties involved in fitting stellar population synthesis (SPS) models to rest-UV spectra as well as the full SEDs of galaxies. I quantify differences in galaxy parameters estimated using different combinations of models and assumptions, and explore the dependence of the rest-UV portion of model spectra on stellar metallicity and population age.

# PUBLISHED CONTENT AND CONTRIBUTIONS

Theios, R. L. et al. (2020). "Galactic Outflows in z ∼ 2-3 Galaxies from KBSS-MOSFIRE". (in preparation).
R.L.T. contributed to data aquisition and analysis, and wrote the manuscript.

Theios, R. L. et al. (Jan. 2019). "Dust Attenuation, Star Formation, and Metallicity in z ∼ 2-3 Galaxies from KBSS-MOSFIRE". In: *ApJ* 871, 128, p. 128. DOI: 10.3847/1538-4357/aaf386. arXiv: 1805.00016.
R.L.T. contributed to data aquisition and analysis, and wrote the manuscript.

# TABLE OF CONTENTS

# LIST OF ILLUSTRATIONS

# LIST OF TABLES

*Chapter 1*

# INTRODUCTION

One of the most important goals of modern astrophysics is characterizing the growth of galaxies over cosmic time. In the last few decades, the astronomical community has reached general agreement on the growth of large-scale structure via the hierarchical merging of dark matter halos. Galaxies accrete pristine gas from the intergalactic medium (IGM), which is then formed into stars, enriched with heavy elements through stellar mass loss and supernovae, and expelled back into the circumgalactic medium (CGM) and IGM via galactic winds.

Studies of the evolution of star formation rates over cosmic time (Madau and Dickinson, 2014) have revealed that the overall rate of star formation in the Universe rises smoothly with time, peaking between $1 < z < 3$ (corresponding to lookback times of $8 - 12$ Gyr), before declining to the levels seen today. This behavior makes sense within the framework in which growth of galaxies is regulated by a balance between gas accretion and feedback. However, the details of the baryonic physics that dominates galaxy formation on small scales remain largely unexplored.

Furthermore, a large majority of the stellar mass in the universe formed at $z > 1$, yet most observational effort towards characterizing the physical conditions of galaxies has been limited to the local Universe ($z \sim 0$), because galaxies over a wide range in stellar mass and star formation rate (SFR) are bright enough to be observed in large numbers. It stands to reason that many of the trends and scaling relations we observe in galaxies today were encoded at $z \sim 1 - 3$.

Indeed, galaxies at $z \sim 2$ are systematically different from their low-redshift counterparts in several ways—on average, they exhibit higher SFRs at fixed stellar mass, larger gas fractions, and more compact sizes (Erb et al., 2006b; Law et al., 2012; Tacconi et al., 2013). At these redshifts, however, detailed spectroscopic observations have historically been challenging. Furthermore, the effects of many of the baryonic processes contributing to galaxy evolution are degenerate with one another, and it can be difficult to disentangle them.

In order to break this degeneracy, it is necessary to leverage information from multiple sources across the electromagnetic spectrum—in particular, by studying both the interstellar medium (ISM) where star formation is taking place, and the

massive stars that enrich and irradiate this gas. The rest-frame UV and rest-frame optical portions of galaxy spectra contain many complementary features arising from both massive stars and the ISM. Fortunately, at $2.0 \leq z \leq 2.7$ many strong nebular emission lines fortuitously fall within near-IR atmospheric transmission windows, and the FUV (1000 – 2000 Å) portion of galaxy spectra falls above the atmospheric cutoff near 3100 Å. Galaxies at $2.0 \leq z \leq 2.7$ are thus ideal targets for ground-based observations, as it is possible to simultaneously study their stellar and nebular properties. This has been the focus of the near-IR component of the Keck Baryonic Structure Survey (KBSS-MOSFIRE) since the commissioning of MOSFIRE in 2012 (Steidel et al., 2014; Steidel et al., 2016; Strom et al., 2017, 2018; Theios et al., 2019).

The KBSS comprises 15 independent fields, each of which is centered on one of the brightest optical quasars in the sky ($m_V \approx 15 - 17$), with $z_{\rm QSO} \sim 2.5 - 2.85$. High-resolution spectroscopy of the central QSOs provides detailed information about the IGM and CGM along each QSO sightline (Rudie et al., 2012). The galaxies are selected from deep optical and near-infrared imaging so as to provide a large dynamic range of galaxy properties, and followed up with spectroscopy in the rest-UV with Keck/LRIS and in the rest-optical with Keck/MOSFIRE.

In the following sections, I discuss the utility of rest-optical and rest-UV galaxy spectra, and the progress that has been made thus far in jointly analyzing these spectra in order to characterize the properties of high-redshift galaxies.

### 1.1 Your eyes can deceive you. Don't trust them

Until recently, much of the information about galaxies at $z \gtrsim 1.5$ has come from the rest-UV portion of the spectra, observed with optical spectrographs on large ground-based telescopes. The far-UV spectra of these galaxies contain a wealth of features arising from hot stars, H II regions, dust, and outflowing gas. Figure 1.1 shows the composite FUV spectrum of 121 KBSS galaxies, with important features indicated.

These include H I Ly$\alpha$, seen in emission, absorption, or a combination of both; low-ionization interstellar metal absorption lines associated with neutral gas; interstellar absorption from higher-ionized species; P Cygni stellar wind features; photospheric features from hot stars; and nebular emission lines. All of these features are superposed on continuum emission dominated by OB stars, with a shape that is modified by dust reddening internal to the galaxy.

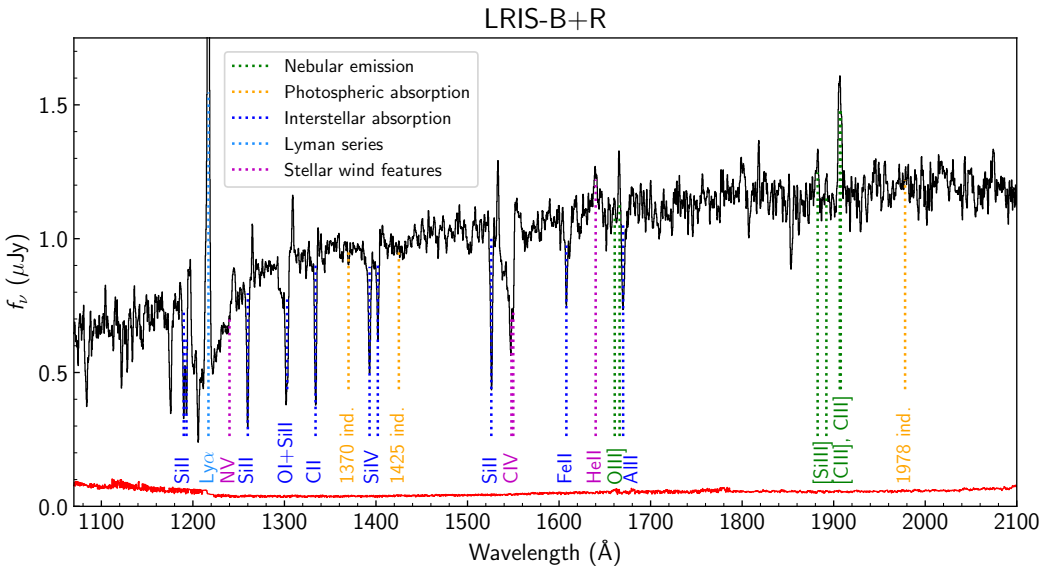


Figure 1.1: LRIS-B+R rest-UV spectrum of a stack of 121 KBSS galaxies (discussed in Section 3.2). Important spectral features are indicated by dotted lines: nebular emission lines in green, interstellar absorption lines in blue, regions of stellar photospheric absorption lines in orange, and stellar wind features in magenta. Note that the He II$\lambda$1640 stellar wind feature also has a nebular contribution, and the C IV P-Cygni stellar wind feature is superposed on interstellar absorption. The three photospheric absorption features indicated here are blends, proposed by Leitherer et al. (2001) and Rix et al. (2004) as metallicity indicators. Finally, H I Ly$\alpha$ is indicated in light blue, and can appear as emission, absorption, or a superposition of both (which is the case for this composite).

These features can vary significantly across the galaxy population. In general, however, the interstellar absorption lines are blueshifted with respect to Ly$\alpha$, indicating the presence of large-scale outflows. However, this makes it difficult to characterize the kinematics of the outflow, since Ly$\alpha$ is resonantly scattered, and the UV nebular emission lines that may be used to estimate the systemic redshift are typically faint relative to the interstellar (IS) absorption. And since the spectra of individual galaxies at these redshifts are typically not of sufficient quality to perform detailed analyses, it is often necessary to average the spectra of multiple galaxies together in order to increase the signal-to-noise (e.g. Shapley et al., 2003). However, generating these composites requires accurate measurements of the systemic redshift in order to shift each spectrum into the rest frame.

Thus, until recently, rest-UV spectra at $z \sim 2$ had only been studied in detail for a handful of gravitationally lensed galaxies (Pettini et al., 2002; Quider et al.,

2009, 2010). These preliminary works found IS absorption spread over a wide range of velocities; in the case of MS1512-cB58, Pettini et al. (2002) measured outflow velocities over the range $-800$ km/s $\lesssim v \lesssim +200$ km/s with a centroid of $v = -255$ km/s. The column density and covering fraction of outflowing gas appears to vary from galaxy to galaxy, and some show evidence for a "patchy" distribution. Most strikingly, cB58 appears to be "chemically young," in the sense that the chemical enrichment of its ISM is dominated by the byproducts of core-collapse supernovae (CCSNe).

Rix et al. (2004) developed a technique for estimating stellar abundances in the rest-UV spectra of high redshift galaxies by investigating the sensitivity of model spectra to metallicity, from 1/20 to twice solar. They identified a number of regions which are sensitive to metallicity but relatively clean of other features, the most robust of which is a blend of Fe III stellar photospheric absorption lines centered on 1978 Å. In recent years, higher-quality rest-UV spectra and the development of more sophisticated stellar population synthesis codes have made more robust studies possible. Still, this analysis presents several challenges, which we discuss in Section 1.3 below.

### 1.2 An elegant weapon for a more civilized age

With the advent of multi-object near-IR spectrographs such as Keck/NIRSPEC (and later MOSFIRE), it became possible to measure systemic redshifts for larger samples of galaxies at $z \sim 2-3$, using nebular emission lines in the rest-frame optical such as H$\alpha$ which originate in H II regions. Beyond their utility in measuring redshifts, the spectra of H II regions are valuable tools for characterizing the physical conditions of galaxies across cosmic time.

The suite of nebular emission lines available in the rest-frame optical spectra ($3600 \lesssim \lambda \lesssim 7000$Å) includes probes of ISM properties such as electron temperature ([O III]$\lambda\lambda$4960, 5008/[O III]$\lambda$4363), electron density ([O II]$\lambda\lambda$3727, 3729 and [S II]$\lambda\lambda$6718, 6732), ionization parameter ([O III]$\lambda\lambda$4960, 5008/[O II]$\lambda\lambda$3727, 3729)), and empirical "strong-line" metallicity indicators such as ([O III]+[O II])/H$\beta$ ("R23;" Kewley and Dopita 2002) and ([O III]$\lambda$5008/H$\beta$)/([N II]$\lambda$6585/H$\alpha$) ("O3N2;" Pettini and Pagel 2004). Figure 1.2 shows portions of the rest-optical spectum of the same stack of KBSS galaxies shown in Figure 1.1, with several of these strong emission lines indicated.

Diagnostic line ratio diagrams such as [N II]/H$\alpha$ vs. [O III]/H$\beta$ ("N2-BPT"; Baldwin

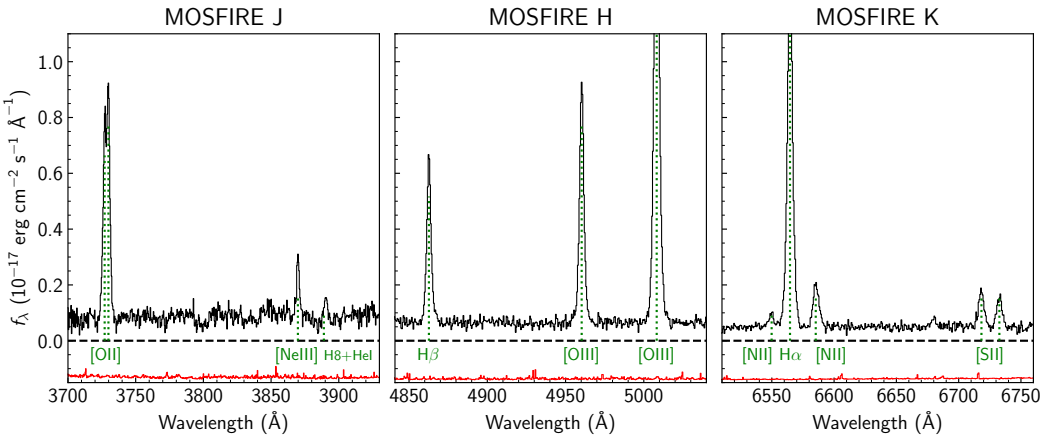


Figure 1.2: Portions of the MOSFIRE J, H, and K-band rest-optical spectra of a stack of 121 KBSS galaxies (discussed in Section 3.2). Strong nebular emission lines are indicated in green.

et al., 1981; Veilleux and Osterbrock, 1987) are often used to distinguish between excitation mechanisms in galaxies at both low and high redshift. Studies of large samples of galaxies from the Sloan Digital Sky Survey (SDSS) have shown that star-forming galaxies follow a tight locus in parameter space, moving from high [N II]/H$\alpha$ and low [O III]/H$\beta$ to low [N II]/H$\alpha$ and high [O III]/H$\beta$ with increasing gas-phase metallicity and decreasing ionization. On the other hand, galaxies hosting active galactic nuclei (AGN) occupy a distinct region of parameter space with high [N II]/H$\alpha$ and high [O III]/H$\beta$, due to enhanced collisional line emission caused by the harder ionizing spectrum from the active nucleus. Kewley et al. (2001) and Kauffmann et al. (2003) devised classification curves in N2-BPT parameter space that are commonly used to distinguish AGN from normal star-forming galaxies at low redshift.

While these lines are easily accessible in the local universe, at $z \sim 2-3$ they are shifted into the near-infrared, where the capabilities of most spectrographs have traditionally been limited relative to their optical counterparts. Still, early studies of nebular emission lines in high-redshift galaxies suggested that they occupy an entirely separate region of parameter space from both star-forming galaxies and AGN at low redshift (e.g. Shapley et al., 2005; Erb et al., 2006a). More recently, with the advances made by near-IR multi-object spectrographs and integral field unit (IFU) spectrographs on the *Hubble Space Telescope* (HST) and 8-10 m class ground-based telescopes, more robust studies have become feasible. Observations of larger samples of $z \sim 2-3$ galaxies from the KBSS and MOSDEF surveys

confirmed that these galaxies are indeed offset in the BPT plane (Masters et al., 2014; Steidel et al., 2014; Shapley et al., 2015; Strom et al., 2017). Figure 1.3 shows the N2-BPT diagram for KBSS-MOSFIRE galaxies compared to SDSS, with known AGN indicated.

Understanding the cause of this "BPT offset" has proven difficult, due to the variety of possible explanations, the effects of which are in many cases degenerate with one another. Several mechanisms have been proposed, including higher N/O at fixed O/H (Masters et al., 2014; Shapley et al., 2015; Masters et al., 2016; Sanders et al., 2016). Strom et al. (2017, 2018) came to the conclusion that the primary cause of this offset is an increase in the hardness of the ionizing spectrum at fixed N/O and O/H. This result can be explained by the effects of Fe-poor stellar populations including massive binaries, and is supported by several lines of reasoning (further discussed in Section 1.3 below).

This issue is one example of a fundamental problem with studies of physical conditions in high-redshift galaxies: owing to the inherent differences in the massive stellar populations generating the observed nebular emission, many scaling relations and calibrations often used at low redshift no longer apply. In particular, gas-phase metallicity indicators such as the empirical "strong line" ratios exhibit different correlations with N/O and ionization parameter, and the efficacy of these calibrations at high redshift is dubious (Steidel et al., 2014; Strom et al., 2017, 2018).

### 1.3 When $9 \times 10^7$ years old you reach, look as good you will not

Given the degeneracies between many observational probes of galaxy physical properties, it stands to reason that the best approach would be to tackle the problem from multiple angles. As discussed above, both the rest-UV and rest-optical spectra of galaxies at $2 < z < 2.7$ are accessible with ground-based telescopes, and these two spectral regimes are causally connected as well. The rest-frame far-UV contains the non-ionizing UV continuum from OB stars, encoding information about properties such as stellar metallicity, SFR, stellar population age, and initial mass function (IMF). The ionizing UV continuum, which cannot be observed directly, can be studied via nebular emission lines in the rest-optical and rest-UV that are the direct response of the galaxy ISM to this radiation. Simultaneously, these nebular emission lines can be used to probe the ISM properties of H II regions.

Steidel et al. (2016) demonstrated the diagnostic power of complementary rest-UV and rest-optical spectra for a pilot sample of 30 galaxies known as KBSS-LM1, taken

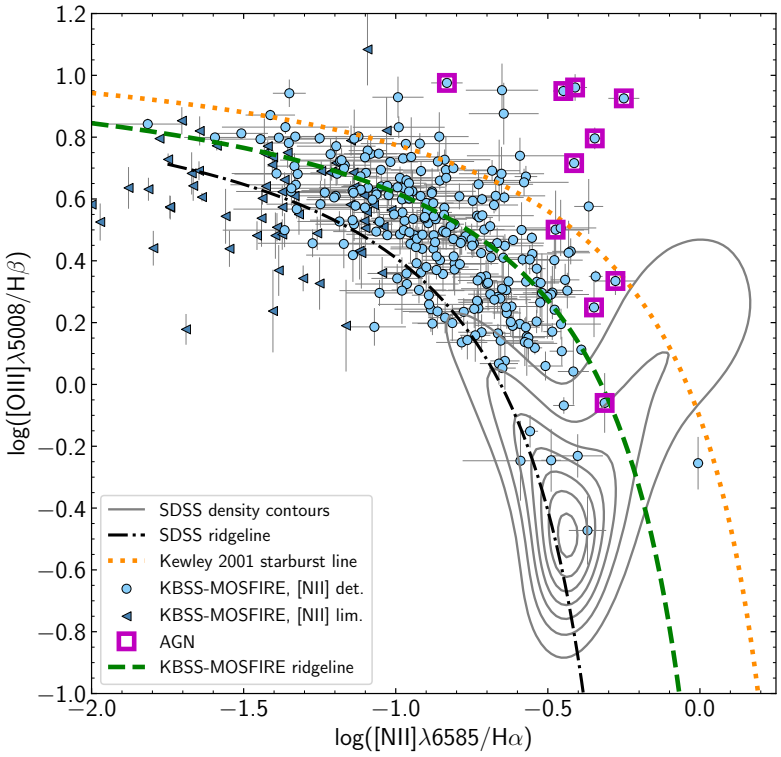


Figure 1.3: N2-BPT diagram for SDSS (gray contours), and the KBSS-MOSFIRE sample (blue points). Also shown are the Kewley et al. (2001) maximum starburst line and the polynomial fit to the locus of KBSS galaxies discussed by Strom et al. (2017). Upper limits in [N II]$\lambda$6585 ($2\sigma$) are shown as triangles, and known AGN are indicated by magenta squares.

from the first two slitmasks of the larger KBSS-LRIS+MOSFIRE (LM) project. The general approach taken by Steidel et al. (2016) was to compile a suite of high-resolution stellar population synthesis (SPS) models with a range of assumed stellar metallicity ($Z_*$) and IMF (slope and upper mass cutoff), find the subset of models that best fit the observed spectrum, and input the best-fit subset of SPS models as the ionizing radiation source in photoionization models (Cloudy; Ferland et al., 2013), which predict the observed nebular line ratios as a function of the ionization parameter $U$ and the gas-phase metallicity $Z_{\rm neb}$. Steidel et al. (2016) found that the stellar FUV spectrum is best matched by models with low stellar metallicity ($Z_* \simeq 0.001 - 0.002$, or $Z_*/Z_\odot \simeq 0.07 - 0.14$, assuming the solar abundance scale of Asplund et al. 2009); however, the observed nebular emission line ratios require relatively high gas-phase oxygen abundances ($Z_{\rm neb}/Z_\odot \simeq 0.5$, or 12 + log(O/H) $\simeq$ 8.39). The apparent discrepancy between $Z_*$ and $Z_{\rm neb}$ can be explained by the fact that the EUV and FUV stellar spectra are controlled primarily by Fe/H, whereas

$Z_{\rm neb}$ effectively is the gas-phase O/H. This requires a factor of $\sim 5$ enhancement in O/Fe relative to solar that is consistent with the expected yields from CCSNe (e.g. Nomoto et al., 2006), which makes sense given the short and rising star formation histories typical of galaxies at these redshifts (Reddy et al., 2012b).

Furthermore, Steidel et al. (2016) found that only models including the effects of massive star binary evolution—the "Binary Population and Spectral Synthesis" models (BPASS; Eldridge et al., 2017; Stanway and Eldridge, 2018)—are able to reproduce the observed level of nebular excitation, as well as the He II $\lambda$1640 stellar wind feature. It has been established that *most* massive stars evolve in binary systems (Crowther, 2007; Sana et al., 2012), and that this multiplicity can result in unique evolutionary pathways not possible in single stars. For example, massive stars with metallicities $Z_* < 0.004$ can undergo a phenomenon known as "quasi-homogenous evolution" (QHE; see, e.g. Eldridge and Stanway, 2012) in which the more massive star overflows its Roche lobe, and due to the weak stellar winds inherent to low metallicities, the companion accretes rapidly and spins up until it is fully mixed. This can result in stars with extreme-UV radiation similar to that of Wolf-Rayet stars, but over a much longer timescale, which is necessary to explain the high levels of nebular excitation in high-redshift galaxies.

### 1.4 Try not. Do, or do not. There is no try. (outline of this thesis)

It is clear that this paradigm shift in our understanding of stellar populations in high-redshift galaxies may result in revised estimates of many galaxy properties, beyond what has already been discussed. In this thesis, I aim to address several of these issues.

First, star formation rates can be estimated in a variety of ways, yet many of the most commonly-used calibrations depend on other parameters in a complex matter. In particular, estimates of SFR require a dust correction, and there is some evidence to suggest that the most appropriate dust attenuation curve at high redshift is different from what is commonly assumed in local galaxies. SFR calibrations also depend on the properties of the massive stellar populations; in particular, when SFRs are estimated from H$\alpha$, low-metallicity binary star models such as BPASS predict a higher H$\alpha$ per unit SFR as a natural consequence of their harder ionizing radiation fields, thus reducing the inferred SFR relative to most commonly used calibrations. In Chapter 2, I compare estimates of dust attenuation and SFR from rest-optical spectra of KBSS galaxies to those inferred from the rest-UV spectral shape and SED

fitting, and explore differences between high-redshift and low-redshift calibrations.

Second, it has long been known that while large-scale galactic winds are only observed in local starburst galaxies with a star formation rate surface density of $\Sigma_{\rm SFR} \gtrsim 0.1 M_{\odot}$ yr$^{-1}$ kpc$^{-2}$, outflows are observed in nearly *every* galaxy at $z \sim 2-3$. However, specific scaling relations between outflow kinematics and other galaxy properties have not been well-established. Due to the difficulty of obtaining large samples of high-quality rest-UV spectra of high-redshift galaxies, several studies in recent years have instead searched for signatures of ionized gas outflows via the broad wings of nebular emission lines in the rest-optical. In Chapter 3, I compare these two methods using rest-optical and rest-UV spectra from the KBSS dataset, and examine trends between outflow velocity and other galaxy properties.

While low-metallicity SPS models including binary stars are most likely to reproduce the observed physical conditions in high-redshift galaxies, very few studies have utilized these models in spectral energy distribution (SED) fits to broadband photometry. In Chapter 4, I explore the systematic uncertainties involved in SED fitting and compare results (e.g. stellar mass, SFR, reddening, and stellar population age) using the BPASS models to those assuming single-star, solar metallicity models. Finally, I revisit the issue of fitting SPS models to rest-UV spectra.

*Chapter 2*

# DUST ATTENUATION, STAR FORMATION, AND METALLICITY IN $z \sim 2-3$ GALAXIES FROM KBSS-MOSFIRE

Theios, R. L. et al. (Jan. 2019). "Dust Attenuation, Star Formation, and Metallicity in z ~ 2-3 Galaxies from KBSS-MOSFIRE". In: *ApJ* 871, 128, p. 128. DOI: 10.3847/1538-4357/aaf386. arXiv: 1805.00016.

Rachel L. Theios[1], Charles C. Steidel[1], Allison L. Strom[2], Gwen C. Rudie[2], Ryan F. Trainor[3], Naveen A. Reddy[4]

[1]Cahill Center for Astronomy and Astrophysics, California Institute of Technology, Pasadena, CA 91125, USA
[2]Carnegie Observatories, 813 Santa Barbara Street, Pasadena, CA 91101, USA
[3]Physics and Astronomy Department, Franklin & Marshall College, 415 Harrisburg Pike, Lancaster, PA 17603
[4]Department of Physics and Astronomy, University of California, Riverside, 900 University Avenue, Riverside, CA 92521, USA

**Abstract**

We present a detailed analysis of 317 $2.0 \leq z \leq 2.7$ star-forming galaxies from the Keck Baryonic Structure Survey (KBSS). Using complementary spectroscopic observations with Keck/LRIS and Keck/MOSFIRE, as well as spectral energy distribution (SED) fits to broadband photometry, we examine the joint rest-UV and rest-optical properties of the same galaxies, including stellar and nebular dust attenuation, metallicity, and star formation rate (SFR). The inferred parameters of the stellar population (reddening, age, SFR, and stellar mass) are strongly dependent on the details of the assumed stellar population model and he shape of the attenuation curve. Nebular reddening is generally larger than continuum reddening, but with large scatter. Compared to local galaxies, high-redshift galaxies have lower gas-phase metallicities (and/or higher nebular excitation) at fixed nebular reddening, and higher nebular reddening at fixed stellar mass, consistent with gas fractions that increase with redshift.We find that continuum reddening is correlated with 12 + $\log(\mathrm{O/H})_{\mathrm{O3N2}}$ at $3.0\sigma$ significance, whereas nebular reddening is correlated with only $1.1\sigma$ significance. This may reflect the dependence of both continuum reddening and O3N2 on the shape of the ionizing radiation field produced by the massive stars. Finally, we show that H$\alpha$-based and SED-based estimates of SFR exhibit significant scatter relative to one another, and agree on average only for particular

combinations of spectral synthesis models and attenuation curves. We find that the SMC extinction curve predicts consistent SFRs if we assume the sub-solar ($0.14Z_{\odot}$) binary star models that are favored for high-redshift galaxies.

## 2.1 Introduction

It is well-established that much of the stellar mass in the universe formed at $z > 1$ and that star-forming systems dominate the galaxy population at this epoch (Madau and Dickinson, 2014). Constraining details of the cosmic star formation rate evolution has long been a focus of extragalactic astrophysics, but it is a complex issue, as estimates of star formation rate (SFR) are subject to uncertainties in a wide variety of parameters, including dust attenuation corrections, the timescale of the current episode of star formation, the ionizing photon production rate (used to estimate SFRs from H$\alpha$ luminosities), and the assumed stellar initial mass function (IMF).

In order to recover the intrinsic SFR of a galaxy, one must first determine the effect of dust obscuration on the observations used to measure it. However, this determination is not always straightforward, as both the rest-UV stellar continuum and nebular emission lines can be used to estimate the SFR at high redshift (in cases where far-IR measurements are not available), and these two SFR indicators neccessitate different measures of the dust attenuation correction. Generally, such corrections involve measuring the dust reddening $E(B-V)$ relative to an SED template and translating it to an attenuation in magnitudes $A_{\lambda}$ assuming some attenuation curve, usually parameterized by the quantity $k(\lambda)$, which is defined such that $k(\lambda) = A_{\lambda}/E(B-V)$.

Attenuation affecting the far-UV stellar continuum has been estimated using a variety of methods, including the so-called IRX-$\beta$ relation, where the UV continuum slope $\beta$, sensitive to the reddening, is correlated with the ratio $L_{\rm IR}/L_{\rm UV}$ (IRX), which traces the attenuation (Calzetti et al., 1994; Meurer et al., 1999; Adelberger and Steidel, 2000; Reddy et al., 2006, 2010; Buat et al., 2011; Reddy et al., 2012a; Reddy et al., 2012b). Similarly, continuum attenuation can be measured by SFR comparisons (Erb et al., 2006a; Daddi et al., 2007; Reddy et al., 2010, 2012b) and SED fitting to broad- and medium-band photometry using stellar population synthesis (SPS) models (Kriek and Conroy, 2013; Reddy et al., 2015). At high redshift, the UV slope has been shown to be a reasonable tracer of dust attenuation on average (e.g. Reddy et al., 2006; Daddi et al., 2007; Reddy et al., 2010; Reddy et al., 2012a), although it is also sensitive to the stellar population age, metallicity,

star formation history, IMF, and binarity (Reddy et al., 2015, and references therein).

The standard method for measuring dust attenuation towards star-forming regions in local galaxies involves comparing the Balmer decrement (BD)—the observed ratio $I(\mathrm{H}\alpha)/I(\mathrm{H}\beta)$—to the intrinsic value expected with no nebular reddening, $I(\mathrm{H}\alpha)/I(\mathrm{H}\beta) = 2.86$ for $T_e = 10000$ K and Case B recombination (Osterbrock, 1989). The Balmer decrement is used to derive a value of nebular reddening $E(B-V)_{\mathrm{neb}}$, which is typically translated into a dust correction by assuming a line-of-sight extinction relation such as the Milky Way curve of Cardelli et al. (1989). At $z > 1$, however, H$\alpha$ and H$\beta$ are redshifted to near-IR wavelengths, where observations have historically been more difficult to obtain than in the optical. In recent years, with the advances made by slitless and multi-object near-IR spectrographs on the *Hubble Space Telescope* (HST) and 8-10 m class ground-based telescopes, it has become feasible to measure the Balmer decrement directly for large samples of galaxies at intermediate and high redshift (e.g. Price et al., 2014; Reddy et al., 2015; Nelson et al., 2016; Strom et al., 2017).

Although the general consensus is that the nebular reddening $E(B-V)_{\mathrm{neb}}$ should be used to derive a dust correction for emission lines and the continuum reddening $E(B-V)_{\mathrm{cont}}$ should be used to derive a dust correction for the continuum, the relationship between these two quantities remains uncertain at high redshift, as both values depend on the details of the assumed massive stellar populations. The detailed relationship between nebular and continuum reddening depends on complex effects such as geometry and the starburst age distribution.

There is an extensive body of literature comparing $E(B-V)_{\mathrm{neb}}$ and $E(B-V)_{\mathrm{cont}}$ (e.g. Calzetti et al., 2000; Kashino et al., 2013; Price et al., 2014; Reddy et al., 2015; Shivaei et al., 2016), with far from uniform results. Calzetti et al. (2000) found that in nearby starburst galaxies, reddening is higher towards star-forming regions, and on average $E(B-V)_{\mathrm{neb}} = 2.27E(B-V)_{\mathrm{cont}}$, where $E(B-V)_{\mathrm{cont}}$ is derived using the Calzetti et al. (2000) starburst attenuation relation, and $E(B-V)_{\mathrm{neb}}$ assumes a line-of-sight relation such as the Galactic extinction curve of Cardelli et al. (1989)[1]. At intermediate and high redshift ($z \sim 1.5-3$), some studies have found that reddening is higher towards star-forming regions relative to the stellar populations producing the FUV-NUV continuum, where both the nebulae and the stellar continuum are assumed to be reddened using attenuation curves established at low redshift (e.g. Kashino et al., 2013; Price et al., 2014; Reddy et al., 2015). Other studies have found

[1] Calzetti et al. (2000) used the Seaton (1979) extinction law.

that the assumption $E(B-V)_{\rm neb} \approx E(B-V)_{\rm cont}$ is sufficient to produce consistent SFRs between observations of H$\alpha$ and X-ray, mid-IR, and far-IR observations of similarly selected galaxies at $z \sim 2$ (Reddy and Steidel, 2004; Erb et al., 2006a; Reddy et al., 2006; Daddi et al., 2007; Reddy et al., 2010; Reddy et al., 2012a).

Many subsequent studies have used $E(B-V)_{\rm cont}$ as a proxy for $E(B-V)_{\rm neb}$ when direct measurements are not available. However, Steidel et al. (2014) noted that the equation relating $E(B-V)_{\rm cont}$ to $E(B-V)_{\rm neb}$ given by Calzetti et al. (2000) is often misinterpreted to mean that the attenuation in magnitudes affecting an H$\alpha$ photon is a factor of 2.27 higher than that affecting a continuum photon at the same wavelength. In fact, the equation $E(B-V)_{\rm neb} = 2.27E(B-V)_{\rm cont}$ is valid only if the same attenuation curve (Calzetti et al. 2000) and extinction curve (Cardelli et al. 1989) have been used. Thus, the difference in attenuation between H$\alpha$ and the continuum depends on the details of the two assumed attenuation curves.

Another issue that remains to be addressed is the appropriate attenuation curve to apply to high-redshift galaxies. While some recent studies (e.g. Álvarez-Márquez et al., 2016; Reddy et al., 2017) have found the SMC curve to best reproduce the conditions in high-redshift galaxies, other studies (e.g. Koprowski et al., 2018; McLure et al., 2018) have argued that the Calzetti et al. (2000) curve remains the most applicable attenuation curve.

Even after the appropriate dust correction has been determined, measurement of the intrinsic SFR of a galaxy depends on other parameters in a potentially complex manner. It is well-known that estimates of SFR for individual galaxies using different indicators can vary widely, particularly for the dustiest galaxies with $L_{\rm bol} \gtrsim 10^{12} L_{\odot}$ for which UV color-based methods systematically underpredict the SFR (e.g. Reddy et al., 2012b). Similarly, estimates of SFR may differ due to the timescale over which indicators are sensitive: H$\alpha$ luminosity is sensitive only to the stars producing significant numbers of ionizing photons, while the FUV continuum (1000-2000 Å) may have significant contributions from stars with lifetimes up to $\sim$ 100 Myr. In detail, converting an observation of H$\alpha$ luminosity or UV continuum slope to an SFR both depend on the timescale of the current episode of star formation and the star formation history (SFH) over the preceding $\sim$ 100 Myr.

Perhaps more importantly, estimates of the SFR depend on the nature of the population of massive stars that dominates the EUV and FUV light. Recent studies (e.g., Steidel et al., 2016) have indicated that developments in our understanding of massive stars, such as the significant role of binary evolution, may lead to revised

estimates of galaxy SFRs at high redshift. For the BPASSv2.2 models (Stanway and Eldridge, 2018) used in this paper, the H$\alpha$ luminosity per unit solar mass of stars formed per year is larger by a factor of $\sim 2$ (once differences in IMF have been accounted for) compared to the canonical conversion often used in the literature (Kennicutt, 1998; Kennicutt and Evans, 2012). The canonical values are based on modeling of solar-metallicity nebulae (and single-star SPS models) that are likely appropriate for most $z \sim 0$ galaxies; however, the ISM conditions at $z \sim 2$ are quite different, characterized by lower gas-phase metallicities than $z \sim 0$ galaxies at fixed stellar mass and harder ionizing radiation fields (Strom et al., 2017). Thus, comparing SFRs estimated from H$\alpha$ luminosity, dust-corrected using the Balmer decrement, to those estimated from the UV stellar continuum, dust-corrected using the UV continuum slope, can yield important insights into the nature of star formation at high redshift.

In this paper we analyze a sample of 317 galaxies with $2.0 \leq z \leq 2.7$ observed as part of the Keck Baryonic Structure Survey (KBSS; Rudie et al., 2012; Steidel et al., 2014; Strom et al., 2017), with high-quality near-IR spectra from Keck/MOSFIRE (McLean et al., 2012) together with deep optical spectra obtained with Keck/LRIS (Oke et al., 1995; Steidel et al., 2004), providing complementary rest-frame optical and rest-frame UV spectra of the same objects. KBSS is a large, targeted spectroscopic survey designed to jointly probe galaxies and the surrounding intergalactic medium (IGM) and circumgalactic medium (CGM) at the peak epoch of galaxy assembly, $z \sim 2-3$. The redshift range $2.0 \leq z \leq 2.7$ is ideal for ground-based observations due to the fortuitous placement of nebular emission lines with respect to atmospheric transmission windows. Additionally, at $2.0 \leq z \leq 2.7$, the FUV portion of galaxy spectra falls above the atmospheric cutoff near 3100 Å. Thus, this redshift range uniquely provides access to both the stellar FUV continuum and nebular emission lines, making it possible to directly compare stellar and nebular measures of reddening and star formation. Finally, the availability of strong nebular emission lines in this redshift range allows us to estimate gas-phase oxygen abundance using strong-line methods, as a function of stellar mass ($M_*$), SFR, and dust reddening.

The outline of the paper is as follows. In Section 2.2 we introduce the subset of the KBSS-MOSFIRE sample discussed in this paper, and in Section 2.3 we describe our methodology for modeling stellar populations and measuring galaxy parameters. In Section 2.4 we present composite rest-UV spectra to which we have fit spectral

synthesis models. We examine the relationship between stellar and nebular dust attenuation in Section 2.5. We compare dust attenuation with inferred gas-phase oxygen abundance and stellar mass in Section 2.5. Section 2.6 compares SFRs inferred from H$\alpha$ with those inferred from SED fitting. Section 2.7 discusses the implications of these results, and Section 2.8 summarizes our conclusions.

Throughout the paper, we adopt a $\Lambda$CDM cosmology with $H_0 = 70$ km s$^{-1}$ Mpc$^{-1}$, $\Omega_\Lambda = 0.7$, and $\Omega_\mathrm{m} = 0.3$. Conversion relative to solar metallicity assumes $Z_\odot = 0.0142$ (where $Z$ is the fraction of metals by mass), as in Asplund et al. (2009). Specific spectral features are referred to using their vacuum wavelengths, and magnitudes are given in the AB system.

## 2.2 Observations and data

### Photometric observations

Photometric data in the KBSS survey fields include broadband photometry in the optical ($U_nG\mathcal{R}$), near-IR ($J$, $H$, $K_s$, and WFC3-IR F140W and F160W), and mid-IR (*Spitzer*-Infrared Array Camera 3.6$\mu$m and 4.5$\mu$m). The near-IR photometry was corrected for the emission line contribution from H$\alpha$ and [O III] using measured fluxes from MOSFIRE. Most KBSS galaxies are selected by their rest-UV colors using a $U_nG\mathcal{R}$ color selection scheme designed to select Lyman Break Galaxy analogues at $z \gtrsim 2$. While this color selection technique may bias the sample against, massive, dusty galaxies, the inclusion of $\mathcal{R}K$ objects (discussed by Strom et al. 2017) alleviates this bias somewhat. Details of the photometric data and sample selection are described elsewhere (e.g. Adelberger et al., 2004; Steidel et al., 2004; Reddy et al., 2012b; Steidel et al., 2014; Strom et al., 2017).

### LRIS observations

Optical (rest-UV) spectra of KBSS galaxies were obtained with Keck/LRIS. LRIS observations in the KBSS survey fields have been obtained over the course of the past decade, and include observations with a variety of wavelength coverage, signal to noise ratio, and spectral resolution (for details, see Shapley et al., 2005; Steidel et al., 2010; Reddy et al., 2012b; Steidel et al., 2016). Here we used observations with the blue channel of LRIS (LRIS-B), using both the 600 line/mm grism, which achieves a resolving power of $R \sim 1400$ and covers the wavelength range 3300 – 5600 Å, and the 400 line/mm grism, which achieves $R \sim 800$, covers 3100 – 6200 Å, and is optimized for the highest throughput at wavelengths $\leq 4000$ Å.

Due to the variable signal to noise ratio of the LRIS spectra used in this paper, we

stack the spectra in bins of selected galaxy properties. For the stacking analysis, the spectra were interpolated onto a common rest wavelength scale of 0.35 Å/pixel and averaged without weighting; the rest wavelength range $1100 \leq \lambda_0 \leq 1700$ Å was used for fitting. To test that the relative flux calibration of the LRIS spectra was consistent with the photometry, we generated composite spectra in bins of $E(B-V)$ (as inferred from SED fits to broadband photometry of individual objects), and fit stellar spectral synthesis models to the composites to infer a continuum $E(B-V)$. The two measures of continuum reddening are comparable.

**MOSFIRE observations**

Near-IR (rest-optical) spectra of KBSS galaxies were obtained with Keck/MOSFIRE. The near-IR portion of the KBSS survey (KBSS-MOSFIRE) was designed to provide high-quality rest-optical spectra for galaxies in the KBSS survey fields with multiwavelength ancillary data as well as spectroscopic observations (primarily with LRIS-B). For a full description of KBSS-MOSFIRE observing strategies, data reduction, sample selection, and emission-line fitting, see Steidel et al. (2014) and Strom et al. (2017). In this work, we focus on the subset of KBSS-MOSFIRE galaxies with nebular redshifts $2.0 \lesssim z \lesssim 2.7$ in order to place important strong emission lines in the NIR atmospheric passbands, and with sufficiently deep $H$-band and $K$-band spectra to allow significant detections of the emission lines of interest: H$\alpha$ $\lambda$6564.61 and [N II]$\lambda$6585.27 in the $K$ band, and H$\beta$ $\lambda$4862.72 and [O III]$\lambda$5008.24 in the $H$ band. The Balmer lines have been corrected for underlying Balmer absorption based on the best-fit SED models, as detailed by Strom et al. (2017).

Of particular importance for the purposes of this paper is the issue of cross-band calibration—correcting emission line fluxes for relative slit losses so that the ratios of lines observed in different spectral bands are accurate. This cross-calibration is necessary for analyses involving the Balmer decrement, as H$\beta$ falls in $H$ band and H$\alpha$ in $K$ band for galaxies over the redshift range of interest for this study, $2.0 \leq z \leq 2.7$. The method used to estimate slit losses is described in detail by Strom et al. (2017). In brief, the cross-calibration combines separate observations of the same objects on independent slit masks with observations of a bright star placed on each mask in order to correct for slit losses for each object in each observed band.

Table 2.1: Sample Statistics

| Galaxy Sample | $N_{\rm gal}$ | $z_{\rm neb}$ (Median) | H$\alpha$/H$\beta$ (Median) |
|---|---|---|---|
| KBSS-MOSFIRE | 1103 | 2.23 | ... |
| $2.0 \leq z \leq 2.7$ | 735 | 2.30 | ... |
| H$\alpha$+H$\beta$[a] | 373 | 2.29 | 3.97 ± 1.90 |
| H$\alpha$/H$\beta > 3\sigma$[b] | 317 | 2.29 | 3.87 ± 1.60 |
| [O III]+[N II][c] | 270 | 2.29 | 3.88 ± 1.60 |
| LRIS+MOSFIRE[d] | 270 | 2.30 | 3.95 ± 1.83 |

Error bars on median values are the inter-quartile range.

[a]The subset of KBSS-MOSFIRE galaxies with $2.0 \leq z \leq 2.7$ and measurements of the Balmer decrement H$\alpha$/H$\beta$ at any significance.

[b]The main sample discussed in this paper is the subset of KBSS-MOSFIRE galaxies with $2.0 \leq z \leq 2.7$ and $S/N > 3$ on the Balmer decrement H$\alpha$/H$\beta$, including slit loss uncertainties in $H$ and $K$.

[c]The [O III]+[N II] sample is the subset of those galaxies with observations of [O III]$\lambda$5008 and [N II]$\lambda$6585, 32 of which are undetected ($< 2\sigma$) in [N II]$\lambda$6585.

[d]The LRIS+MOSFIRE sample is the subset of galaxies with complementary LRIS observations.

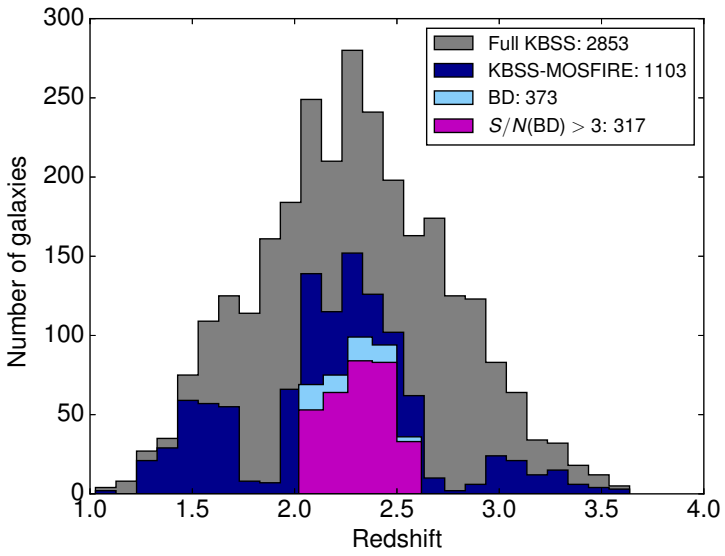


Figure 2.1: Histogram of the galaxy samples discussed in this paper (see Table 2.1).

**Sample statistics**

The full KBSS sample consists of 2844 galaxies with spectroscopically confirmed redshifts in the range $1.5 \leq z \leq 3.5$, 2345 of which have existing rest-frame UV spectra from Keck/LRIS-B. As of 2016 December 1, the near-IR portion of KBSS (KBSS-MOSFIRE) consists of 1103 galaxies with nebular redshifts obtained from Keck/MOSFIRE. AGN have been removed from the sample, as discussed by Steidel et al. (2014) and Strom et al. (2017).

Table 2.1 and Figure 2.1 give an overview of the galaxy samples discussed in this paper. We selected 317 KBSS-MOSFIRE galaxies in the redshift range $2.0 \leq z \leq 2.7$ with robust detections of both H$\alpha$ and H$\beta$ ($S/N > 3$ for the line ratio H$\alpha$/H$\beta$). The motivation for a significance cut on the Balmer decrement is discussed by Strom et al. (2017): since attenuation corrections scale nonlinearly with the measured value of the Balmer decrement, relatively small uncertainties in the Balmer decrement can translate to a large uncertainty in quantities that are dust-corrected using the Balmer decrement, such as the SFR. In practice, requiring $S/N > 3$ in the ratio BD $\equiv I(\mathrm{H}\alpha)/I(\mathrm{H}\beta)$, including the relative slit loss uncertainties in $H$ and $K$, means that $S/N > 3$ in H$\alpha$ and H$\beta$ individually. While it is possible that this significance cut biases the sample against the most heavily reddened objects, the median BD of the $3\sigma$ sample and the subset of 373 galaxies with measurements of BD at any significance are consistent within the errors (Table 2.1).

## 2.3 Derived galaxy properties

**SED fitting**

Stellar masses, SFRs (hereafter $\mathrm{SFR_{SED}}$), and continuum color excesses (hereafter $E(B-V)_{\mathrm{SED}}$) were estimated for KBSS-MOSFIRE galaxies based on SED fits to broadband photometry described in Section 2.2.

The SED fitting uses reddened "Binary Population and Spectral Synthesis" (BPASSv2.2; Stanway and Eldridge, 2018) models assuming a constant star formation history (SFH) and a minimum allowed age of 50 Myr. As discussed by Reddy et al. (2012a), this minimum age is approximately the central dynamical timescale and is imposed to prevent best-fit solutions with unrealistically young ages[2]. The BPASSv2.2 model used as the fiducial model for the SED fitting has a stellar metallicity of $Z_* = 0.002$ ($Z_*/Z_\odot \approx 0.14$) and binary evolution included. The

[2]While galaxies at these redshifts would likely have a rising SFH in reality, we expect the results assuming constant SFHs to be similar (Reddy et al., 2012a). Rising SFHs will be implemented in a future paper.

model we used has a Kroupa-type IMF, with a slope of $-2.35$ for masses $> 1M_{\odot}$ and an upper mass cutoff of $100M_{\odot}$.

The main feature of the BPASSv2.2 models is the inclusion of massive interacting binary stars, increasing the overall ionizing flux and producing a harder ionizing spectrum for models with continuous star formation histories. This is an advantage over previous models not only because most massive stars are known to be in binaries (Crowther, 2007; Sana et al., 2012) but because previous studies (e.g. Reddy et al., 2016b; Steidel et al., 2016; Strom et al., 2017) have found that these models are better able to simultaneously match the rest-UV stellar continuum and nebular emission lines than single-star models. Additionally, Steidel et al. (2016) noted that an important difference between the continuous star formation BPASS models including binary evolution and single-star models such as Starburst99 (Leitherer et al., 2014) and the single-star BPASS models is that the binary models predict a broad stellar He II $\lambda$1640 emission line (for constant SF models) not present in single-star models. This feature is detected in all our rest-UV composite spectra; see Section 2.4. We elect to employ the BPASSv2.2 models over the more commonly used Bruzual and Charlot (2003) solar metallicity models for these reasons.

The SED fitting procedure, characteristic uncertainties for each SED fit parameter, and comparisons to other stellar population synthesis (SPS) models are discussed in Section 4.2.

**Attenuation curves**

We fit SEDs to each galaxy assuming two attenuation curves for the stellar continuum: Calzetti et al. (2000) and SMC. For the nebular emission lines, we assume the Milky Way curve of Cardelli et al. (1989, with $R_V = 3.1$), or SMC for comparison when the continuum attenuation curve is assumed to be SMC.[3]. The "SMC" curve used here combines the empirical SMC extinction curve from Gordon et al. (2003, assuming $R_V = 2.74$) with an empirical extension to the far-UV using the method described by Reddy et al. (2016a). The version of the Calzetti et al. (2000) curve we use here has also been revised to include an extension to the far-UV using the same method. Similarly, we fit SEDs using an attenuation curve that combines the results of Reddy et al. (2015) based on the MOSDEF survey (Kriek et al., 2015)

[3]While the choice of attenuation curve used to correct the stellar continuum has a large effect on the SED-inferred SFRs, it makes very little difference which curve is used to correct nebular emission line ratios, as all the commonly employed curves have a very similar slope and normalization in the optical regime (see Figure 2.2). Note however that the Calzetti et al. 2000 curve has a slightly higher normalization due to the difference in $R_V$

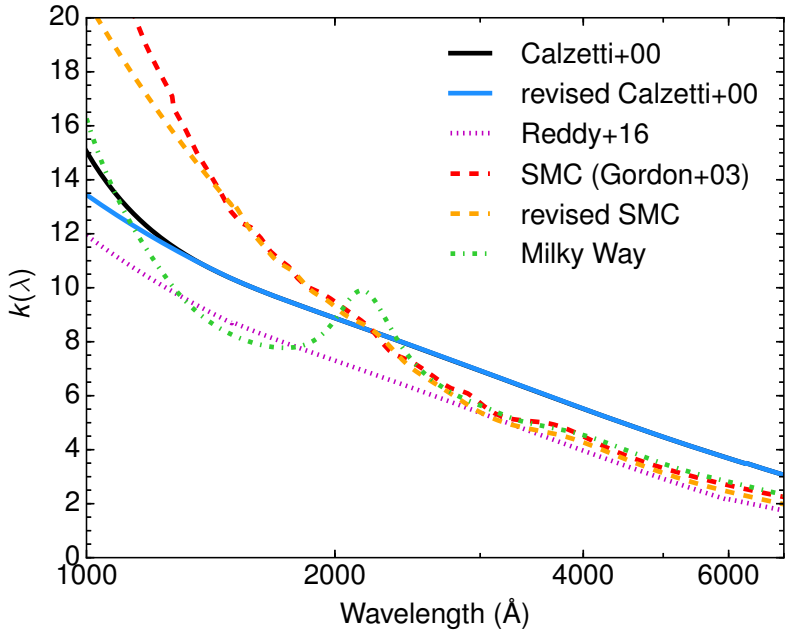


Figure 2.2: Comparison of attenuation curves discussed in this paper: the Calzetti et al. (2000) starburst attenuation relation, the attenuation curve of Reddy et al. (2016a), the SMC (Gordon et al., 2003), and the Milky Way extinction curve of Cardelli et al. (1989). The revised Calzetti et al. (2000) and SMC curves, used in this paper, include an empirical extension to the far-UV, using the method described in Reddy et al. (2016a).

with a new empirical extension to the far-UV described by Reddy et al. (2016a). The results using this curve are similar to Calzetti et al. (2000), so for simplicity we discuss only Calzetti et al. (2000) and SMC in this paper. The four curves discussed here are compared in Figure 2.2. The original versions of the Calzetti et al. (2000) and SMC curves are shown for reference.

Figures 2.3, 2.4, and 2.5 compare the distributions of $E(B-V)_{\rm SED}$, $\rm SFR_{SED}$, and $M_*$, for Calzetti et al. (2000) and SMC attenuation. While the inferred stellar masses are consistent within the errors, using SMC results in a lower $E(B-V)_{\rm SED}$ and $\rm SFR_{SED}$ due to the greater degree of attenuation per unit reddening in the UV. On average, $E(B-V)_{\rm SED}$ inferred for SMC is lower than that inferred for Calzetti et al. (2000) by a factor of 2.4, and $\rm SFR_{SED}$ is lower by a factor of 3.3, or 0.5 dex.

We find that 38% of galaxies in the sample are better fit by SMC, 16% are better fit by Calzetti et al. (2000), and 46% are comparably fit by either curve within the uncertainty. Details and example SED fits are given in Section 4.2. Throughout the paper, we compare results assuming each of the two curves.

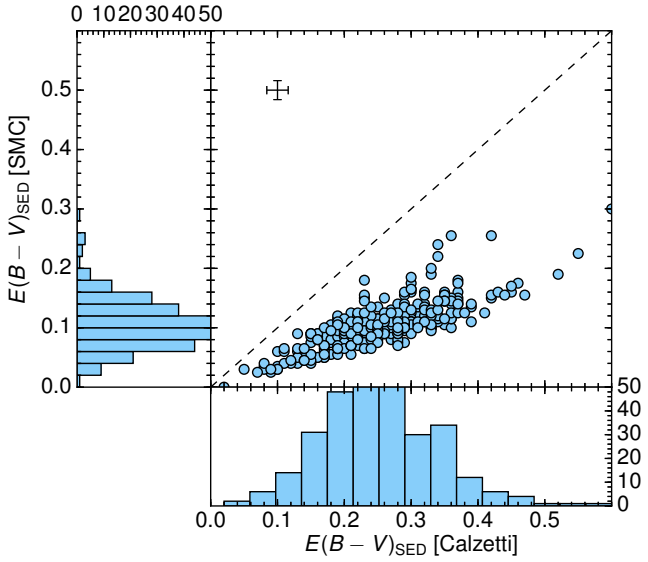


Figure 2.3: $E(B-V)_{\rm SED}$ assuming the Calzetti et al. (2000) attenuation curve versus $E(B-V)_{\rm SED}$ assuming the SMC extinction curve, for the 317 galaxies with $> 3\sigma$ measurements of BD (including the uncertainties on the slit loss corrections in $H$ and $K$). Here all quantities are derived from a BPASSv2.2 $Z_* = 0.002$ binary model. SMC predicts a lower $E(B-V)_{\rm SED}$ by a factor of 2.4 on average.

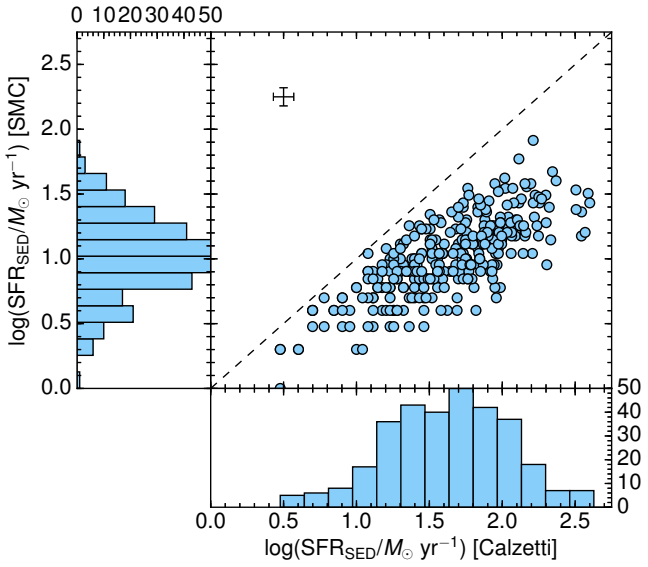


Figure 2.4: $\mathrm{SFR}_{\rm SED}$ assuming the Calzetti et al. (2000) attenuation curve versus $\mathrm{SFR}_{\rm SED}$ assuming the SMC extinction curve, for the 317 galaxies with $> 3\sigma$ measurements of BD (including the uncertainties on the slit loss corrections in $H$ and $K$). Here all quantities are derived from a BPASSv2.2 $Z_* = 0.002$ binary model. SMC predicts a lower $\mathrm{SFR}_{\rm SED}$ by 0.50 dex on average.

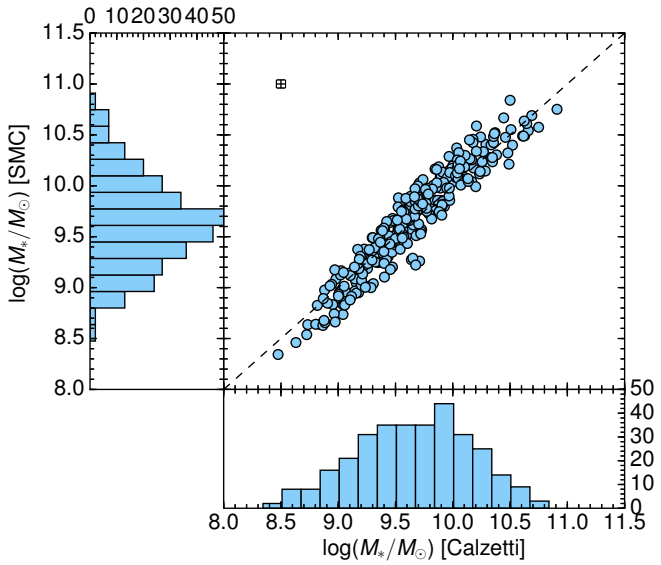


Figure 2.5: $M_*$ assuming the Calzetti et al. (2000) attenuation curve versus $M_*$ assuming the SMC extinction curve, for the 317 galaxies with $> 3\sigma$ measurements of BD (including the uncertainties on the slit loss corrections in $H$ and $K$). Here all quantities are derived from a BPASSv2.2 $Z_* = 0.002$ binary model. The stellar masses predicted by both curves are consistent on average.

Table 2.2: Star Formation Rate Calibrations

| Model | $\log(L_{\mathrm{H}\alpha})$ ($M_\odot$ yr$^{-1}$) | $\log(\nu L_\nu)$ [1500 Å] ($M_\odot$ yr$^{-1}$) | $\xi_{\mathrm{ion}}$ |
|---|---|---|---|
| BPASSv2.2 $300M_\odot$ $Z_* = 0.002$ | 41.78 | 43.51 | 25.44 |
| BPASSv2.2 $100M_\odot$ $Z_* = 0.002$ | 41.64 | 43.46 | 25.35 |
| BPASSv2.2 $100M_\odot$ $Z_* = 0.004$ | 41.59 | 43.46 | 25.30 |
| BPASSv2.2 $100M_\odot$ $Z_* = 0.020$ | 41.35 | 43.36 | 25.16 |
| Bruzual and Charlot (2003) $Z_* = 0.004$ | 41.37 | 43.44 | 25.10 |
| Bruzual and Charlot (2003) $Z_* = 0.020$ | 41.14 | 43.40 | 24.91 |
| Kennicutt and Evans (2012) | 41.30 | 43.35 | 25.12 |

All quantities are corrected to the default BPASS IMF. BPASSv2.2 and Bruzual and Charlot (2003) values assume a star formation timescale of $t = 10^{8.0}$ yr.

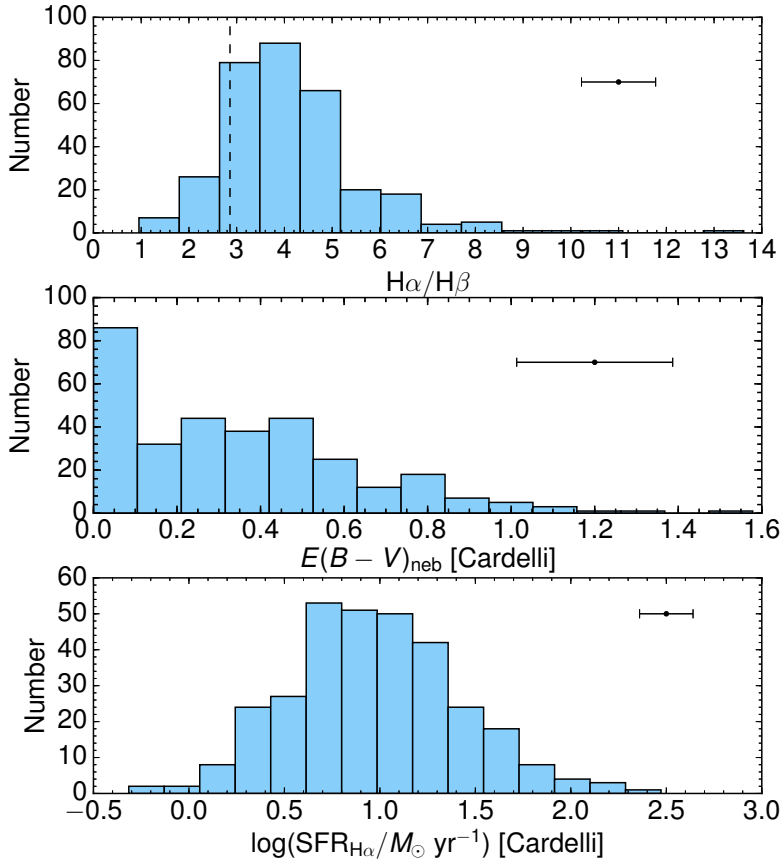


Figure 2.6: Histogram of H$\alpha$/H$\beta$, $E(B-V)_{\rm neb}$, and $\mathrm{SFR}_{\mathrm{H}\alpha}$ for the 317 galaxies with $> 3\sigma$ measurements of BD. The dashed line denotes the theoretical limit of BD in the case of no dust reddening, BD = 2.86. Galaxies with BD $\leq$ 2.86 (13% of the sample) are assigned $E(B-V)_{\rm neb} = 0$. Here $E(B-V)_{\rm neb}$ and $\mathrm{SFR}_{\mathrm{H}\alpha}$ assume Cardelli et al. (1989) extinction. The error bars represent the median uncertainty in each quantity.

### Nebular reddening and H$\alpha$ SFR

Nebular reddening $E(B-V)_{\rm neb}$ was calculated from BD using the equation

$$E(B-V)_{\rm neb} = \frac{2.5}{k(\mathrm{H}\beta) - k(\mathrm{H}\alpha)} \log_{10}\left(\frac{\mathrm{BD}}{2.86}\right), \tag{2.1}$$

where $k(\mathrm{H}\beta)$ and $k(\mathrm{H}\alpha)$ are the values of the attenuation curve evaluated at the wavelengths of H$\beta$ and H$\alpha$ respectively; recall that $k(\lambda) = A_\lambda / E(B-V)$.

The attenuation at H$\alpha$ is

$$\begin{aligned} A_{\mathrm{H}\alpha} &= k(\mathrm{H}\alpha) E(B-V)_{\rm neb} = 2.54 E(B-V)_{\rm neb} \\ &= 5.90 \log_{10}\left(\frac{\mathrm{BD}}{2.86}\right) \end{aligned} \tag{2.2}$$

assuming Cardelli et al. (1989) extinction and $R_V = 3.1$, or

$$\begin{aligned} A_{H\alpha} &= k(H\alpha)E(B-V)_{neb} = 2.17E(B-V)_{neb} \\ &= 4.95\log_{10}\left(\frac{BD}{2.86}\right) \end{aligned} \tag{2.3}$$

assuming SMC extinction and $R_V = 2.74$. The typical uncertainty on BD, accounting for the errors on the relative slit corrections in $H$ and $K$, is 14%. Of the 317 $z \sim 2.3$ galaxies studied in this paper, 51 (16% of the sample) have BD $< 2.86$, the nominal expectation for zero nebular reddening assuming Case B conditions and $T_e = 10,000$ K. All but 8 of these are consistent with BD $= 2.86$ within $2\sigma$. Galaxies with BD $\leq 2.86$ were assigned $E(B-V)_{neb} = 0$.

SFRs (hereafter $SFR_{H\alpha}$) were estimated using the observed H$\alpha$ recombination line luminosities, corrected using Equation 2.2, or Equation 2.3 in cases where $SFR_{H\alpha}$ was compared to a quantity where continuum attenuation assumes SMC.

To determine the appropriate conversion between H$\alpha$ luminosity and SFR for each galaxy, we calculated the ionizing photon production rate corresponding to the best-fit SED by integrating the SED up to 912 Å:

$$N(H^0) = \int_0^{912\text{Å}} \frac{\lambda f_\lambda}{hc} d\lambda. \tag{2.4}$$

The BPASSv2.2 SEDs are in units of $f_\lambda$ per $M_\odot$ yr$^{-1}$ of star formation, so the expected $L_{H\alpha}$ per $M_\odot$ yr$^{-1}$ of star formation can then be calculated using the equation from Leitherer and Heckman (1995):

$$L_{H\alpha}[\text{erg s}^{-1}] = \frac{1.36N(H^0)}{10^{12}}[\text{s}^{-1}]. \tag{2.5}$$

For $t = 10^8$ yr, assuming an IMF upper mass cutoff of $100M_\odot$:

$$\log(SFR_{H\alpha}/M_\odot\ \text{yr}^{-1}) = \log(L_{H\alpha}/\text{erg s}^{-1}) - 41.64 \tag{2.6}$$

For comparison, the constant value of 41.64 is 0.34 dex higher than the value of 41.30 from Kennicutt and Evans (2012), once they have been converted to the same IMF. H$\alpha$ conversion factors for different model assumptions are given in Table 2.2. The $L_{H\alpha}$/SFR ratio depends on the spectral shape in the EUV, and when emission line ratios are used to identify models with plausible EUV spectral shapes (as in Steidel et al., 2016) they are the models that produce significantly larger numbers of ionizing photons per $M_\odot$ of star formation. This issue is discussed in Section 2.7.

Also given in Table 2.2 are SFR calibrations evaluated at $\lambda = 1500$ Å, as well as values of the ionizing photon production efficiency $\xi_{\rm ion}$. Although these numbers are not explicitly used in this paper, they are illustrative because $\rm SFR_{SED}$ is primarily sensitive to the non-ionizing UV luminosity, rather than the ionizing photon production rate, since it is derived entirely longward of 912 Å. This can be seen in the fact that the 1500Å SFR calibrations for the $300M_\odot$ and $100M_\odot$ BPASSv2.2 models are similar, since the non-ionizing UV luminosity per unit SF has very limited IMF dependence.

Figure 2.6 shows the distribution of BD, $E(B-V)_{\rm neb}$, and $\rm SFR_{H\alpha}$, where $E(B-V)_{\rm neb}$ was calculated from BD assuming a Cardelli et al. (1989) extinction curve.

**Gas-phase oxygen abundances**

The values of gas-phase oxygen abundance quoted in this paper are inferred using the O3N2 index (O3N2 $\equiv \log[([\text{O III}]\lambda5008/\text{H}\beta)/([\text{N II}]\lambda6585/\text{H}\alpha)]$; Pettini and Pagel 2004). Steidel et al. (2014) showed that compared to the N2 index (N2 $\equiv \log([\text{N II}]\lambda6585/\text{H}\alpha)$; Pettini and Pagel 2004), oxygen abundances measured from the O3N2 index were less affected by bias and scatter relative to direct $T_{\rm e}$-based measurements of individual KBSS-MOSFIRE galaxies. In this paper, we use the recalibration of O3N2 proposed by Strom et al. (2017) based on the sample of extragalactic H II regions compiled by Pilyugin et al. (2012), with an 0.24 dex offset added to place the $T_e$ estimates (based on collisionally excited line ratios) onto the same scale as those measured from recombination lines (Esteban et al., 2014; Steidel et al., 2016)[4]:

$$12 + \log(\text{O/H})_{\rm O3N2} = 8.80 - 0.20\ \text{O3N2}. \tag{2.7}$$

Since $[\text{O III}]\lambda5008$ and $\text{H}\beta$ are close in wavelength and $[\text{N II}]\lambda6585$ and $\text{H}\alpha$ are also close in wavelength, the ratio O3N2 and thus $12 + \log(\text{O/H})_{\rm O3N2}$ is reddening-independent. An important point made by several authors (e.g. Steidel et al., 2014; Sanders et al., 2016; Strom et al., 2017) is that the "strong-line" metallicity calibrations established in the local universe may not be accurate at high redshift. The locus of the $z \sim 2.3$ KBSS-MOSFIRE sample is offset with respect to SDSS in the $\log([\text{O III}]\lambda5008/\text{H}\beta)$ versus $\log([\text{N II}]\lambda6585/\text{H}\alpha)$ (N2-BPT) plane, likely driven by harder ionizing spectra at fixed nebular O/H (Steidel et al., 2014; Steidel et al., 2016; Strom et al., 2017). Additionally, at high redshift, the strong-line

[4]This offset also makes $(\text{N/O}) = (\text{N/O})_\odot$ when $(\text{O/H}) = (\text{O/H})_\odot$ for the calibration sample.

ratios become less sensitive to the ionized gas-phase oxygen abundance and more sensitive to the overall spectral shape of the ionizing radiation field produced by massive stars. In practice, this means that the inference of gas-phase metallicity from the O3N2 index is uncertain at high redshift, since O3N2 also tracks excitation. We continue to use O3N2-based inferences of 12 + log(O/H) in this paper, with the caveat that trends of increasing 12 + $\log(\mathrm{O/H})_{\mathrm{O3N2}}$ may also be interpreted as trends of decreasing excitation.

### 2.4 Inferences from composite rest-UV spectra

Composite rest-UV spectra were generated for the subset of 270 galaxies out of 317 with complementary LRIS and MOSFIRE spectra described in Table 2.1 (hereafter the LRIS+MOSFIRE sample). To fit model spectra to the observed data, we used the far-UV spectra generated by the BPASSv2.2 model suite (Stanway and Eldridge, 2018) assuming a constant star formation history with an age of $10^8$ yr, an upper mass IMF cutoff of $100M_{\odot}$, and binary evolution included. The stellar metallicity $Z_*$ and reddening $E(B-V)_{\mathrm{cont}}$ were free parameters in the fitting procedure, and the best-fit combination of $Z_*$ and $E(B-V)_{\mathrm{cont}}$ was determined by a $\chi^2$ minimization. The composites are shown in Figure 2.7; details of the fitting procedure are described in Section 4.3.

Figure 2.8 shows the best-fit values of $E(B-V)_{\mathrm{cont}}$ as a function of each of the six binned quantities: $E(B-V)_{\mathrm{SED}}$, H$\alpha$/H$\beta$ (here converted to $E(B-V)_{\mathrm{neb}}$), 12 + $\log(\mathrm{O/H})_{\mathrm{O3N2}}$, $M_*$, $\mathrm{SFR}_{\mathrm{H}\alpha}$, and $\mathrm{SFR}_{\mathrm{SED}}$. Results are shown for both Calzetti et al. (2000) and SMC attenuation.

The bins in $E(B-V)_{\mathrm{SED}}$ served as a test case, to ensure that photometric and spectroscopic fitting results were internally consistent. We expect $E(B-V)_{\mathrm{SED}}$ and $E(B-V)_{\mathrm{cont}}$ to be strongly correlated, although the correlation might not be 1:1 due to the fact that the stellar metallicity corresponding to $E(B-V)_{\mathrm{cont}}$ is allowed to vary freely, whereas the SED fitting fixes the stellar metallicity at $Z_* = 0.002$[5]. The best-fit values of $E(B-V)_{\mathrm{cont}}$ increase monotonically with increasing $E(B-V)_{\mathrm{SED}}$ as expected and stay very close to the median values of $E(B-V)_{\mathrm{SED}}$ in the bins.

We find that all composites are best fit by either a $Z_* = 0.001$ model ($Z_*/Z_{\odot} = 0.07$) or a $Z_* = 0.002$ model ($Z_*/Z_{\odot} = 0.14$). This is as we might expect based on the analysis from Steidel et al. (2016) which used a similar $\chi^2$ minimization analysis for the "LM1" stack (which contains some of the same galaxy spectra as this sample)

[5]We expect $Z_* \sim 0.001 - 0.002$; see below.

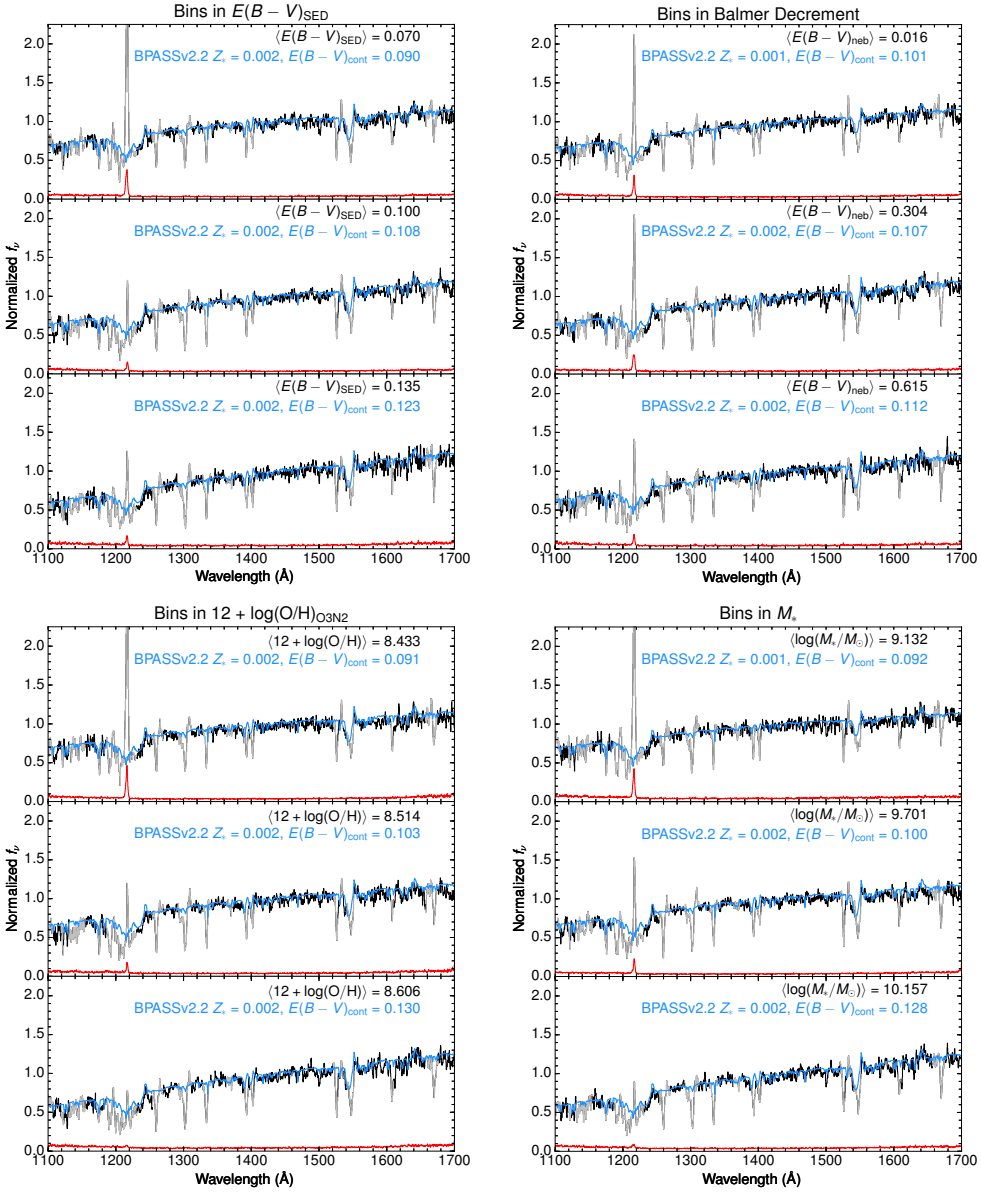


Figure 2.7: Stacked composite rest-frame UV spectra of the LRIS+MOSFIRE sample, in bins of a) $E(B-V)_{\rm SED}$, b) BD (converted to $E(B-V)_{\rm neb}$), c) 12 + $\log({\rm O/H})_{\rm O3N2}$, d) $M_*$, e) ${\rm SFR}_{{\rm H}\alpha}$, and f) ${\rm SFR}_{\rm SED}$. Bootstrapped error spectra are shown in red. Prior to stacking, the spectra were normalized by the median flux in the range 1400 – 1500 Å. Superposed are the best-fit population synthesis models from BPASSv2.2 (blue), reddened by the best-fit $E(B-V)_{\rm cont}$ (assuming an SMC attenuation curve), which was calculated by minimizing $\chi^2$ with respect to the observed spectrum, after masking regions containing nebular emission lines or interstellar absorption lines (gray).

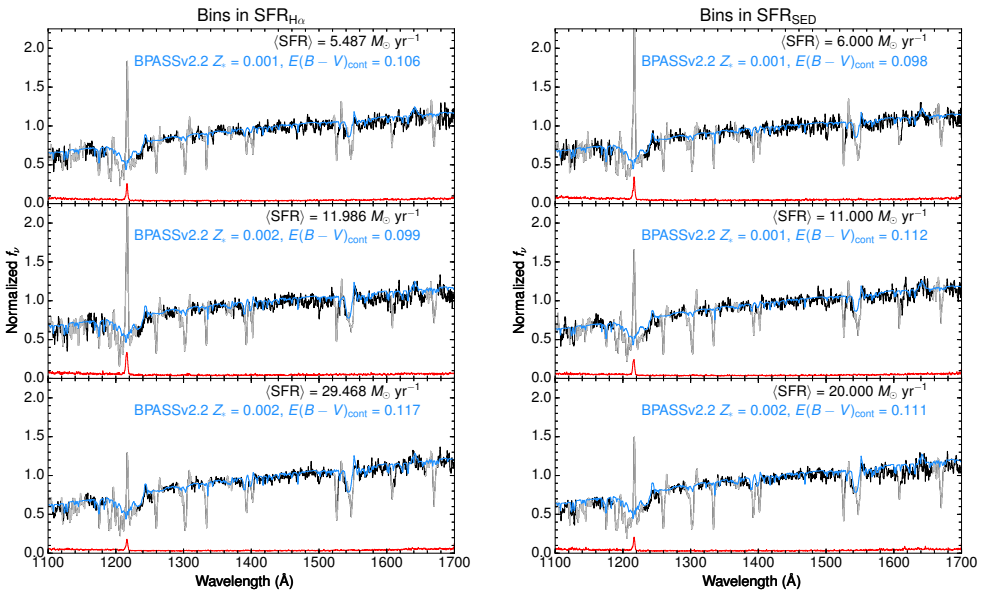


Figure 2.7: (continued)

and found that models with $Z_* \geq 0.003$ were strongly dis-favored compared to those with $Z_* \leq 0.002$. Similarly, Strom et al. (2017, 2018) showed using photoionization modeling that only binary models with low $Z_*$ were able to reproduce the nebular line ratios observed in most individual $z \sim 2.3$ galaxies.

Since the ages we infer for the galaxies in our sample are $\sim 50 - 300$ Myr, and the delay timescale for Fe enrichment of the ISM by Type Ia supernovae is $\sim 300 - 400$ Myr, the ISM metallicities in these galaxies (and thus the abundances of the massive stars) are likely dominated by core-collape supernovae. Rising star formation histories, which are expected for galaxies during the period of most rapid growth (Reddy et al., 2012a), can extend the time period over which ISM enrichment remains dominated by core-collapse SNe. Steidel et al. (2016) argued that under these conditons, galaxies can reach near-solar gas-phase O/H while Fe abundance remains low. Our result is consistent with this general picture, where stellar metallicity is uniformly low at all values of nebular reddening (Figure 2.7b) and 12 + log(O/H)$_{O3N2}$ (Figure 2.7c).

While $E(B-V)_{cont}$ is positively correlated with all six binned quantities, the strength of the correlation varies—the weakest trend is with $E(B-V)_{neb}$. In the following section, we explore these relationships for *individual galaxies* using $E(B-V)_{SED}$, which we have argued is an equally good measure of continuum reddening—we show that the same general trends still hold.

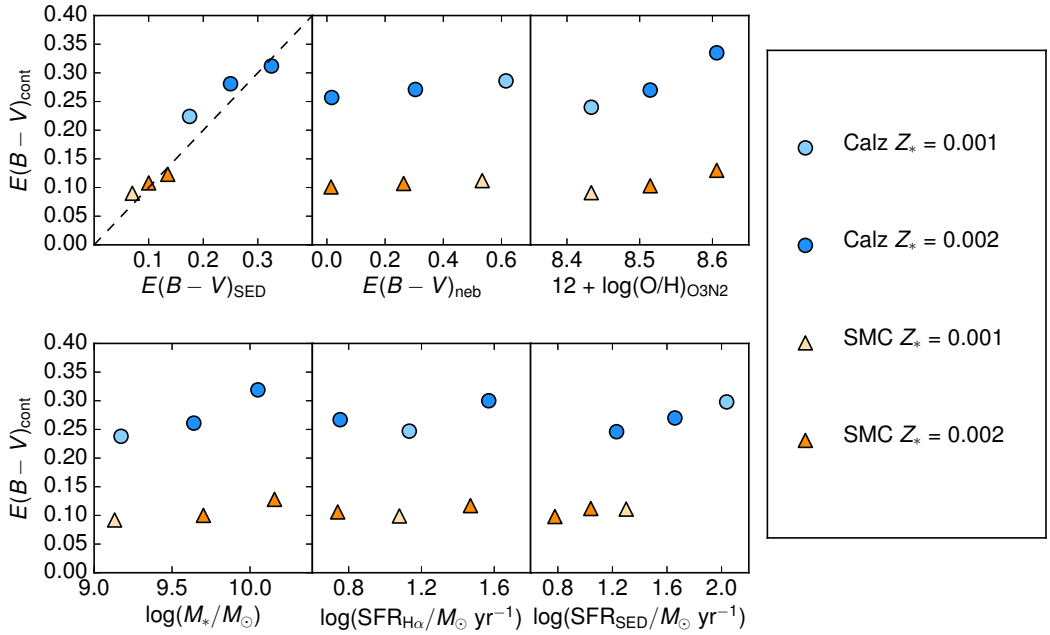


Figure 2.8: Trends between $E(B-V)_{\rm cont}$ as measured from the stacked LRIS spectra shown in Figure 2.7 and the six binned quantities: $E(B-V)_{\rm SED}$, BD (here converted to $E(B-V)_{\rm neb}$), 12 + log(O/H)$_{\rm O3N2}$, $M_*$, SFR$_{\rm H\alpha}$, and SFR$_{\rm SED}$. The blue circles correspond to model fits assuming the Calzetti et al. (2000) attenuation curve and the orange triangles assume SMC. In both cases, the light-colored points correspond to the spectra best-fit by a $Z_* = 0.001$ model, and the dark-colored points correspond to those best-fit by a $Z_* = 0.002$ model. While $E(B-V)_{\rm cont}$ shows increasing trends with every quantity, the stellar metallicity of the best-fit model is consistently low and is not correlated with any of the binned quantities.

## 2.5 Relationship between nebular and continuum attenuation

Figure 2.9 compares $E(B-V)_{\rm SED}$ to $E(B-V)_{\rm neb}$for two combinations of continuum attenuation curve and nebular extinction curve. The solid lines in Figure 2.9 represent orthogonal distance regressions fit to the data, which can be used to derive a translation between $E(B-V)_{\rm SED}$ and $E(B-V)_{\rm neb}$, similar to that proposed by Calzetti et al. (2000). With this sample we find:

$$E(B-V)_{\rm neb,MW} = (1.34 \pm 0.05) E(B-V)_{\rm SED,Calz} \tag{2.8}$$

$$E(B-V)_{\rm neb,SMC} = (3.06 \pm 0.15) E(B-V)_{\rm SED,SMC}. \tag{2.9}$$

The error bars on the coefficients are the standard deviation of the orthogonal distance regression, and the median scatter about each the best-fit lines (in the $E(B-V)_{\rm neb}$ direction) are 0.20 (Cardelli/Calzetti) and 0.19 (SMC). Spearman rank-order correlation coefficients for both combinations of curves are given in Table 2.3.

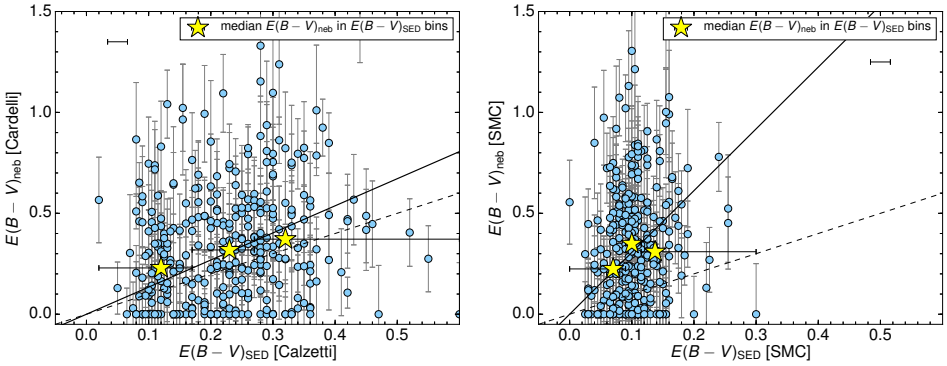


Figure 2.9: $E(B-V)_{\rm neb}$ versus $E(B-V)_{\rm SED}$. The solid lines represent orthogonal distance regressions fit to the data (Equation 2.8), similar to Calzetti et al. (2000), and the dashed lines represent equal $E(B-V)_{\rm neb}$ and $E(B-V)_{\rm SED}$. Yellow stars are median values of $E(B-V)_{\rm neb}$ in equal-number bins of $E(B-V)_{\rm SED}$, and the bin limits are represented as horizontal error bars. The error bars on $E(B-V)_{\rm neb}$ correspond to a $1\sigma$ error in H$\alpha$/H$\beta$, and the horizontal error bar is the representative error on $E(B-V)_{\rm SED}$ discussed in Appendix 4.2. *Left*: The SED fitting assumes a Calzetti et al. (2000) attenuation curve and $E(B-V)_{\rm neb}$ assumes a Cardelli et al. (1989) line-of-sight extinction curve. *Right*: Both attenuation estimates assume SMC extinction. For both assumed curves, $E(B-V)_{\rm neb}$ is generally greater than $E(B-V)_{\rm SED}$, with large scatter; however, the apparent discrepancy between the two reddening estimates is greater when the SMC curve is assumed.

Table 2.3: Spearman Rank-Order Correlations

| Correlated Quantities[a] | Spearman $\rho$[b] | Spearman $\sigma$[c] |
|---|---|---|
| $E(B-V)_{\rm neb}$ [Cardelli] vs. $E(B-V)_{\rm SED}$ [Calzetti] | 0.15 | 2.6 |
| $E(B-V)_{\rm neb}$ [SMC] vs. $E(B-V)_{\rm SED}$ [SMC] | 0.13 | 2.3 |
| 12 + log(O/H)$_{\rm O3N2}$ vs. $E(B-V)_{\rm neb}$ [Cardelli] | 0.06 | 1.1 |
| 12 + log(O/H)$_{\rm O3N2}$ vs. $E(B-V)_{\rm SED}$ [Calzetti] | 0.17 | 3.0 |
| 12 + log(O/H)$_{\rm O3N2}$ vs. $E(B-V)_{\rm SED}$ [SMC] | 0.17 | 3.0 |
| $E(B-V)_{\rm neb}$ [Cardelli] vs. $M_*$ [Calzetti] | 0.23 | 4.2 |
| $E(B-V)_{\rm neb}$ [SMC] vs. $M_*$ [SMC] | 0.21 | 3.7 |
| SFR$_{\rm H\alpha}$ [Cardelli] vs. SFR$_{\rm SED}$ [Calzetti] | 0.24 | 4.3 |
| SFR$_{\rm H\alpha}$ [SMC] vs. SFR$_{\rm SED}$ [SMC] | 0.33 | 6.0 |

[a] The assumed attenuation curves are indicated in brackets.

[b] Spearman rank correlation coefficient.

[c] Standard deviations from null hypothesis.

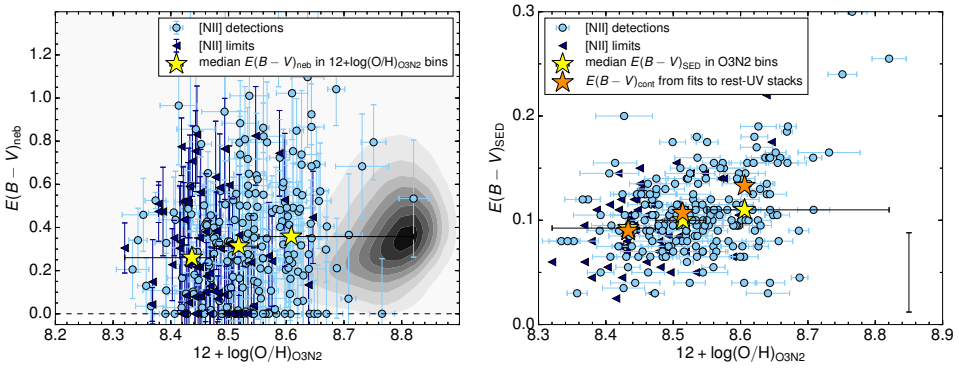


Figure 2.10: *Left:* $E(B-V)_{\rm neb}$ versus 12 + log(O/H)$_{\rm O3N2}$. Dark blue triangles represent $2\sigma$ upper limits in [N II]. Yellow stars represent the median measurements of the individual spectra in four equal-number bins of 12 + log(O/H)$_{\rm O3N2}$. The grayscale contours represent the locus of similarly selected SDSS galaxies (Strom et al., 2017). *Right:* $E(B-V)_{\rm SED}$ versus 12 + log(O/H)$_{\rm O3N2}$, assuming the SMC attenuation curve. Orange stars are measurements of $E(B-V)_{\rm cont}$ for stacks of LRIS spectra in bins of 12 + log(O/H)$_{\rm O3N2}$, and yellow stars are median values of $E(B-V)_{\rm SED}$in the same bins. Bin limits are shown as black error bars. While we find no significant correlation between 12 + log(O/H)$_{\rm O3N2}$ and $E(B-V)_{\rm neb}$, 12 + log(O/H)$_{\rm O3N2}$ and $E(B-V)_{\rm SED}$ are correlated at $3.0\sigma$ significance. Additionally, KBSS galaxies have a lower 12 + log(O/H)$_{\rm O3N2}$ than SDSS galaxies by 0.21 dex on average.

**Relationship between reddening and gas-phase metallicity**

One might expect dust reddening and gas-phase enrichment to be strongly correlated, as metals in the ISM will be depleted onto the same dust grains that attenuate the nebular emission lines—the higher the metal content of the ISM, the more dust grains will be formed (Reddy et al., 2010). Motivated by this picture, the lefthand panel of Figure 2.10 compares measurements of $E(B-V)_{\rm neb}$ to 12 + log(O/H)$_{\rm O3N2}$. The lefthand panel of Figure 2.10 shows, for comparison, low-redshift galaxies from SDSS-DR7 (Abazajian et al., 2009, grayscale contours), selected to have similar detection properties as KBSS-MOSFIRE (see Strom et al., 2017). Figure 2.10 shows that compared to SDSS, the KBSS sample has systematically lower 12 + log(O/H)$_{\rm O3N2}$ by 0.21 dex on average at a given value of $E(B-V)_{\rm neb}$. The righthand panel of Figure 2.10 compares 12 + log(O/H)$_{\rm O3N2}$ with $E(B-V)_{\rm SED}$, where the orange stars are measurements of $E(B-V)_{\rm cont}$ for the stacked rest-UV spectra in bins of 12 + log(O/H)$_{\rm O3N2}$(see Section 2.4). The measurements of $E(B-V)_{\rm cont}$ for the stacks show good agreement with the median $E(B-V)_{\rm SED}$ in the bins (yellow stars), again demonstrating that these quantities on average provide

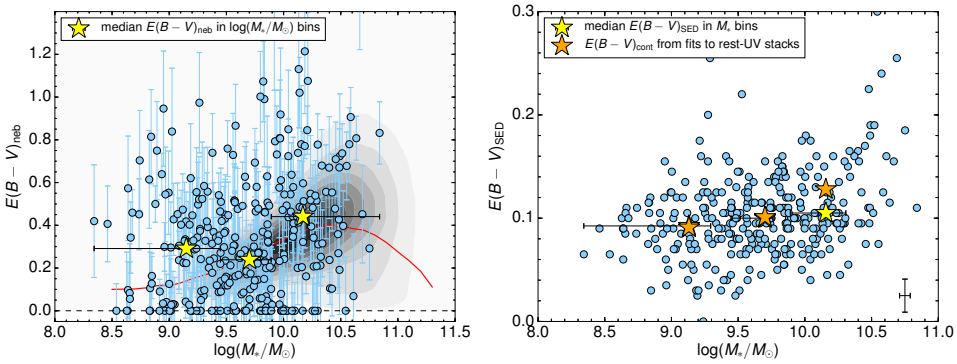


Figure 2.11: *Left:* $E(B-V)_{\rm neb}$ versus $M_*$ inferred from SED fits assuming a BPASSv2.2 $Z_* = 0.002$ continuous star formation model with SMC attenuation. The solid red line represents the locus of SDSS galaxies, determined by the median $E(B-V)_{\rm neb}$ in bins of $M_*$. The KBSS and SDSS galaxies are consistent with being drawn from the same parent distribution in $E(B-V)_{\rm neb}$, but KBSS galaxies are offset to lower stellar masses; thus, the degree of reddening at fixed stellar mass is higher on average in KBSS galaxies. *Right:* $E(B-V)_{\rm SED}$ versus $M_*$, where both quantities have been inferred from SED fits assuming a BPASSv2.2 $Z_* = 0.002$ continuous star formation model with SMC attenuation. The yellow stars represent the median values of $E(B-V)_{\rm SED}$ in equal-number bins of $M_*$, and the orange stars are measurements of $E(B-V)_{\rm cont}$ from stacks of LRIS spectra in the same bins. Bin limits are shown as black error bars. As in Figure 2.10, the trend with continuum reddening are stronger than the trend with nebular reddening.

consistent estimates of the stellar continuum reddening.

We observe no statistically significant correlation between $12 + \log(\mathrm{O/H})_{\rm O3N2}$ and $E(B-V)_{\rm neb}$ ($1.1\sigma$; Table 2.3). However, we do observe a strong correlation between $12 + \log(\mathrm{O/H})_{\rm O3N2}$ and $E(B-V)_{\rm SED}$ ($3.0\sigma$).

### Relationship between $E(B-V)$, $M_*$, and SFR

The lefthand panel of Figure 2.11 compares measurements of $E(B-V)_{\rm neb}$ to $M_*$, where local galaxies from SDSS-DR7 are shown for comparison. The median stellar mass of the KBSS sample is 0.72 dex lower than that of the SDSS sample, and a Kolmogorov-Smirnov (K-S) test revealed that the two samples are drawn from different parent distributions in $M_*$. However, they are consistent with being drawn from the same parent distribution in $E(B-V)_{\rm neb}$. Both samples show a positive correlation between $E(B-V)_{\rm neb}$ and $M_*$. Thus, at fixed $M_*$, KBSS galaxies have a greater degree of nebular reddening on average.

The righthand panel of Figure 2.11 compares $E(B-V)_{\rm SED}$ to $M_*$; while these

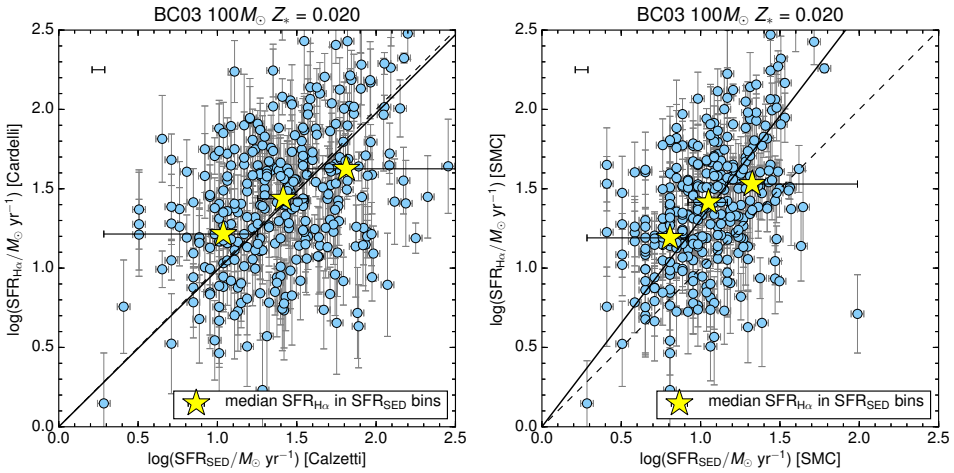


Figure 2.12: Comparison of star formation rates estimated from SED fitting ($SFR_{SED}$) with those based on the H$\alpha$ luminosity ($SFR_{H\alpha}$), for the Bruzual and Charlot (2003) model with $Z_* = 0.020$. The solid lines are orthogonal distance regression lines, and the dashed lines represent equal SFRs. Yellow stars are median vales of $SFR_{H\alpha}$ in equal-number bins of $SFR_{SED}$, and bin limits are represented as horizontal error bars. *Left*: The SED fitting assumes a Calzetti et al. (2000) attenuation curve and the H$\alpha$ measurements assume a Cardelli et al. (1989) line-of-sight extinction curve. *Right*: Both the SED fitting and the H$\alpha$ measurements assume SMC extinction. Using the SMC extinction curve results in values of $\log(SFR_{SED}$ that are offset from $\log(SFR_{H\alpha}$ by a factor of 1.3, whereas using Cardelli et al. (1989) extinction and Calzetti et al. (2000) attenuation results in consistent SFRs on average.

quantities may be degenerate due to the fact that they are both derived from the SED fits, the presence of a correlation is supported by the correlation between $E(B-V)_{\rm cont}$ and $M_*$ (orange stars), which are measured independently. This may be explained by the following argument. $M_*$ is related to the normalization of the model SED relative to the data. $E(B-V)_{\rm SED}$ essentially parametrizes the "shape" of the SED. While the whole spectrum is used for normalization, the matching of the overall shape of the SED is likely to be driven primarily by the shape in the UV, which is also sensitive to parameters such as age and star formation history. Since higher Fe/H at fixed O/H will make UV spectra intrinsically redder for older galaxies, dust reddening and maturity of star formation could be degenerate.

## 2.6 SFR comparisons

In this paper, SFRs are estimated from both SED fitting (which is primarily sensitive to the UV continuum) and H$\alpha$ luminosities. If the correct curve is assumed in both

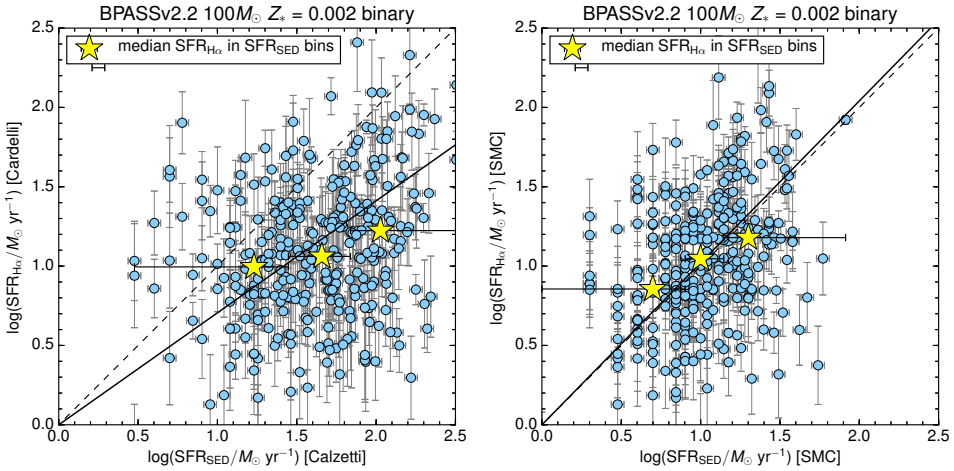


Figure 2.13: Comparison of star formation rates estimated from SED fitting ($SFR_{SED}$) with those based on the H$\alpha$ luminosity ($SFR_{H\alpha}$). The solid lines are orthogonal distance regression lines, and the dashed lines represent equal SFRs. Yellow stars are median vales of $SFR_{H\alpha}$ in equal-number bins of $SFR_{SED}$, and bin limits are represented as horizontal error bars. *Left*: The SED fitting assumes a Calzetti et al. (2000) attenuation curve and the H$\alpha$ measurements assume a Cardelli et al. (1989) line-of-sight extinction curve. *Right*: Both the SED fitting and the H$\alpha$ measurements assume SMC extinction. Using the Calzetti et al. (2000) curve results in values of $\log(SFR_{SED}$ that are offset from $\log(SFR_{H\alpha}$ by a factor of 1.3, whereas using the SMC curve results in consistent SFRs on average.

the UV and optical regime and all systematic uncertainties have been accounted for, then these two measures of SFR should agree on average in the case of continuous star formation.

Figure 2.12 compares $SFR_{H\alpha}$ to $SFR_{SED}$ for the Bruzual and Charlot (2003) $Z_* = 0.020$ models, assuming Calzetti et al. (2000) attenuation and Cardelli et al. (1989) extinction (left), and SMC for both lines and continuum (right). Also shown in Figure 2.13 are orthogonal distance regression lines fit to the data. Using the SMC extinction curve results in values of $\log(SFR_{SED}$ that are offset from $\log(SFR_{H\alpha}$ by a factor of 1.3, whereas using Cardelli et al. (1989) extinction and Calzetti et al. (2000) attenuation results in consistent SFRs on average.

Conversely, Figure 2.13 compares the same quantities, but instead for the BPASSv2.2 $Z = 0.002$ binary models. In this case, using the Calzetti et al. (2000) curve results in values of $\log(SFR_{SED}$ that are offset from $\log(SFR_{H\alpha}$ by a factor of 1.3, whereas using the SMC curve results in consistent SFRs on average.

Figure 2.14 compares the distributions of $SFR_{H\alpha}$ and $SFR_{SED}$ for BPASSv2.2 100$M_\odot$

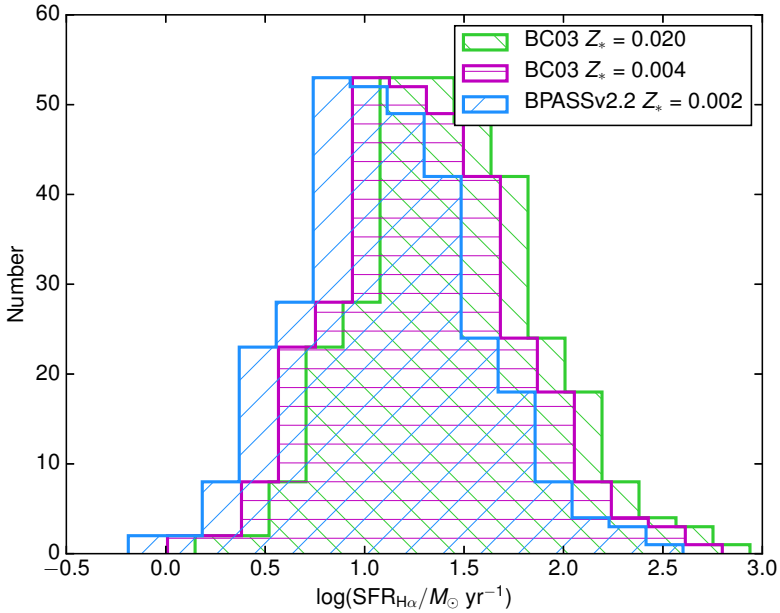


Figure 2.14: Histograms of $SFR_{H\alpha}$ for BPASSv2.2 $100M_\odot$ $Z_*$ = 0.002 binary models (blue), Bruzual and Charlot (2003) $Z_*$ = 0.004 (magenta), and Bruzual and Charlot (2003) $Z_*$ = 0.020 (green). In all cases, the default BPASS IMF is assumed, and H$\alpha$ luminosities have been converted to SFRs by integrating the ionizing portion of the best-fit SED, as described in Section 2.3. Compared to BPASSv2.2, the Bruzual and Charlot (2003) $Z_*$ = 0.004 models predict values of $SFR_{H\alpha}$ that are 0.27 dex higher on average, and the Bruzual and Charlot (2003) $Z_*$ = 0.020 models predict values of $SFR_{H\alpha}$ that are 0.5 dex higher.

$Z_*$ = 0.002 binary models, Bruzual and Charlot (2003) $Z_*$ = 0.004, and Bruzual and Charlot (2003) $Z_*$ = 0.020. In all cases, the default BPASS IMF has been assumed, and H$\alpha$ luminosities have been converted to SFRs by integrating the ionizing portion of the best-fit SED, as described in Section 2.3. Compared to BPASSv2.2, the Bruzual and Charlot (2003) $Z_*$ = 0.004 models predict values of $SFR_{H\alpha}$ that are 0.20 dex higher on average, and the Bruzual and Charlot (2003) $Z_*$ = 0.020 models predict values of $SFR_{H\alpha}$ that are 0.5 dex higher on average, once the differences in IMF have been accounted for. $SFR_{SED}$ assuming the BPASS models is higher than that predicted by Bruzual and Charlot (2003) $Z$ = 0.020 by 0.12 dex, also accounting for differences in IMF.

On the other hand, when the same SED model is assumed, changing the continuum attenuation curve from Calzetti et al. (2000) to SMC lowers $SFR_{SED}$ by 0.69 dex on average, and changing the nebular extinction curve from Cardelli et al. (1989) to SMC lowers $SFR_{H\alpha}$ by 0.06 dex on average. Thus, changing the combination of

assumptions from Bruzual and Charlot (2003) $Z_* = 0.020$ models with Calzetti et al. (2000) attenuation and Cardelli et al. (1989) extinction to BPASSv2.2 $Z_* = 0.002$ models with SMC applied to both lines and continuum lowers $SFR_{SED}$ by 0.57 dex and $SFR_{H\alpha}$ by 0.56 dex. This can be seen clearly in Figures 2.12 and 2.13; differences in attenuation curve cancel out differences in SED model. In order to break this degeneracy and determine the most applicable attenuation relation for our sample, independent constraints on the best-fit SED model are needed.

## 2.7 Discussion

### Comparison between nebular and continuum reddening

Figure 2.9 shows that although a correlation exists between the reddening toward the ionized nebulae and the stellar continuum, there is large scatter. In particular, galaxies with $E(B-V)_{neb} = 0$ (which is defined here as BD $\leq$ 2.86) span the full range of $E(B-V)_{SED}$. Similarly, the measurements of $E(B-V)_{cont}$ for stacked spectra in bins of BD show only a very weak trend, suggesting that nebular reddening is nearly independent of UV continuum reddening.

This relationship between $E(B-V)_{neb}$ and $E(B-V)_{cont}$ is intriguing because previous studies have reached different conclusions. For example, Steidel et al. (2016) found that the best-fit $E(B-V)_{cont}$ for the LM1 stack was consistent with the median $E(B-V)_{neb}$ of the individual galaxies contributing to the stack. They suggested that the similarity between these two quantities implies that the nebular emission lines are powered by the same massive stars that are responsible for the far-UV continuum, and thus there is not likely to be a significant population of dust-obscured massive stars contributing to the nebular emission line luminosities but not the far-UV continuum. We find that with the Calzetti et al. (2000) attenuation curve and Cardelli et al. (1989) extinction curve, $E(B-V)_{neb} = 1.34E(B-V)_{SED}$ on average, in contrast to the factor of 2.27 between $E(B-V)_{neb}$ and $E(B-V)_{cont}$ proposed by Calzetti et al. (2000) for local starburst galaxies. When the SMC curve is applied to both lines and continuum, we find that $E(B-V)_{neb} = 3.06E(B-V)_{SED}$, which is merely due to the steeper slope of the SMC curve in the UV relative to the Calzetti et al. (2000) curve.

At low redshift, the discrepancy between nebular and continuum color excess is usually attributed to increased dust covering fractions surrounding H II regions; i.e., the youngest stars remain in undissipated parent birth clouds (Calzetti et al., 1994; Charlot and Fall, 2000). However, this picture does not explain the significant

fraction of galaxies in the KBSS sample for which $E(B-V)_{\rm SED} > E(B-V)_{\rm neb}$.

Additionally, scatter in the relationship between $E(B-V)_{\rm neb}$ and $E(B-V)_{\rm cont}$ may be due to variations in the dust attenuation curve from galaxy to galaxy. It is unlikely that the same attenuation curve applies to every galaxy in our sample, or even every galaxy in a bin of some observed quantity. Indeed, theoretical work has suggested that observed variations in the IRX-$\beta$ relation may be attributed to variations in the dust attenuation curve due to differences in grain composition, as well as stellar population age, dust temperature, and geometry of the dust distribution (e.g. Granato et al., 2000; Popping et al., 2017; Narayanan et al., 2018). Indeed, we find that the same curve cannot be applied to every galaxy in our sample. While 38% of galaxies in our sample have SEDs that are best fit by SMC, 16% are best fit by Calzetti et al. (2000), and the remainder do not favor either curve within the uncertainty (although the majority of these are nominally better fit by SMC).

Regardless of which curve is assumed, however, the scatter in $E(B-V)_{\rm neb}$ relative to $E(B-V)_{\rm SED}$ is large. Similarly, Figures 2.10 and 2.11 show that while $E(B-V)_{\rm SED}$ is strongly correlated with both 12 + log(O/H)$_{\rm O3N2}$ and $M_*$, neither quantity is strongly correlated with $E(B-V)_{\rm neb}$.

**Correlations with gas-phase metallicity and stellar mass**

Figure 2.10 shows that local galaxies have a higher gas-phase metallicity (and/or lower excitation) at the same $E(B-V)_{\rm neb}$ than high-redshift galaxies. This is consistent with the well-studied offset in the mass-metallicity relation (MZR; Tremonti et al., 2004; Erb et al., 2006c; Mannucci et al., 2010; Zahid et al., 2011; Steidel et al., 2014) at high redshift, such that high-redshift galaxies have lower metallicity at fixed $M_*$.

A number of studies (e.g. Reddy et al., 2010; Heinis et al., 2014; Oteo et al., 2014; Álvarez-Márquez et al., 2016; Bouwens et al., 2016) have noted correlations between continuum dust obscuration and $M_*$; we find such a correlation for the KBSS sample as well (Figure 2.11). Other studies have found a redshift-independent relationship between *nebular* attenuation and stellar mass; Dominguez et al. (2013) found using stacked WFC3 grism spectra of galaxies at intermediate redshift ($0.75 \leq z \leq 1.5$) that these galaxies have a similar BD at fixed stellar mass as SDSS galaxies (within the errors). However, we find that our sample of $z \sim 2.3$ galaxies has a distribution of BD that is similar to that of SDSS galaxies (albeit with large scatter), but a median $M_*$ that is 0.6 dex lower than that of $z \sim 0$ SDSS galaxies. In both samples

there is a positive correlation between $E(B-V)_{\rm neb}$ and $M_*$. Thus, $E(B-V)_{\rm neb}$ is higher in KBSS galaxies than in SDSS galaxies at a fixed $M_*$. The presence of a decrement in the MZR but not in the dust obscuration-stellar mass relation may be explained by the expectation that if dust and metals are produced in the same way across redshift, high-redshift galaxies should have lower dust-to-gas ratios than low-redshift galaxies at the same stellar mass; however, their larger gas fractions (e.g. Daddi et al., 2008; Tacconi et al., 2010) overcompensate for this to produce a larger column of dust at fixed stellar mass. It may also be the case that dust grain composition changes systematically with redshift.

Interestingly, we found (Section 2.5) that the correlation between stellar continuum reddening $E(B-V)_{\rm cont}$ and (reddening-independent) 12 + log(O/H)$_{\rm O3N2}$ is much stronger than that between nebular reddening $E(B-V)_{\rm neb}$ and 12 + log(O/H)$_{\rm O3N2}$ (Figure 2.10; Table 2.3). This may be explained if the intrinsic scatter is much larger for $E(B-V)_{\rm neb}$, a conclusion supported by the weak correlation between $E(B-V)_{\rm neb}$ and $E(B-V)_{\rm SED}$ discussed in the previous section. Alternately, this trend could be explained if $E(B-V)_{\rm SED}$ is a better tracer of gas-phase abundances and/or excitation. Several authors (e.g. Steidel et al., 2014; Sanders et al., 2016; Strom et al., 2017) have noted that at high redshift, line ratios such as O3N2 become less sensitive to gas-phase oxygen abundance and more sensitive to the overall spectral shape of the ionizing radiation field produced by massive stars. Thus, the stronger correlation between 12 + log(O/H)$_{\rm O3N2}$ and $E(B-V)_{\rm SED}$ may be induced because both quantities are closely tied to the spectral shape of the ionizing radiation field produced by the massive stars, which depends on the stellar abundance of Fe.

**SFR comparisons**

Figures 2.12 and 2.13 show that the combination of Calzetti et al. (2000) attenuation for the stellar continuum and Cardelli et al. (1989) Galactic extinction for the nebular emission lines produces consistent H$\alpha$-based and SED-based SFRs when the Bruzual and Charlot (2003) $Z = 0.020$ single-star models are used, as in Steidel et al. (2014). When the BPASSv2.2 $Z = 0.002$ binary models (and appropriate H$\alpha$ conversions) are used, SMC produces consistent SFRs.

As mentioned in Section 2.3, the SEDs of 46% of the sample do not significantly favor either Calzetti et al. (2000) or SMC within the uncertainty. Similarly, while the BPASS models provide a better fit than Bruzual and Charlot (2003) for the majority of the sample, 33% do not significantly favor either model within the uncertainty.

Thus, the SED fitting alone is not able to constrain either the most appropriate dust attenuation curve or the most appropriate SPS model. Indeed, Figure 2.12 appears to indicate that the combination of Calzetti et al. (2000) attenuation, Cardelli et al. (1989) extinction, and the single-star, solar metallicity Bruzual and Charlot (2003) models is a reasonable combination of assumptions, and this is the combination of assumptions used by nearly all previous studies.

However, the BPASSv2.2 $Z_* = 0.002$ models are more consistent with observations than the $Z_* = 0.020$ Bruzual and Charlot (2003) models in that they are better able to simultaneously match the rest-UV continuum, stellar and nebular lines, and rest-optical nebular emission lines. Thus, we argue that the agreement between SFRs when the single-star models are used is likely to be coincidental rather than an indication that these models are an accurate represention of the conditions at high redshift. When the BPASSv2.2 $Z_* = 0.002$ model and corresponding H$\alpha$-to-SFR conversion is used, SMC produces consistent SFRs on average, and so we argue that it is the most appropriate attenuation curve for the majority of KBSS galaxies, in agreement with what has been found in several recent studies (e.g., Capak et al., 2015; Bouwens et al., 2016; Koprowski et al., 2016; Reddy et al., 2017).

The large scatter in $\mathrm{SFR}_{\mathrm{H}\alpha}$ with respect to $\mathrm{SFR}_{\mathrm{SED}}$ could be explained by several factors. First, it is likely that the same H$\alpha$/SFR conversion factor does not apply to every galaxy in our sample. The $L_{\mathrm{H}\alpha}/L_{\mathrm{UV}}$ ratio is directly proportional to the ionizing photon production efficiency $\xi_{\mathrm{ion}}$. Shivaei et al. (2017) found an intrinsic scatter of 0.28 dex in the distribution of $\xi_{\mathrm{ion}}$ for galaxies in the MOSDEF survey. They conclude that variations in $\xi_{\mathrm{ion}}$ cannot be solely explained by object-to-object variations in the dust attenuation curve; rather, the scatter is affected by stellar population properties such as variations in IMF and stellar metallicity. The conversion from H$\alpha$ luminosity to SFR predicted by the BPASSv2.2 models is directly calculated from the model predictions for $\xi_{\mathrm{ion}}$ for a given model template, but it is likely that the intrinsic $\xi_{\mathrm{ion}}$ of a given galaxy varies from the model predictions. Thus, variations in $\xi_{\mathrm{ion}}$ could explain the scatter in the $\mathrm{SFR}_{\mathrm{SED}}/\mathrm{SFR}_{\mathrm{H}\alpha}$ ratio from galaxy to galaxy.

One potential caveat is that variations between H$\alpha$ and UV-based SFRs are frequently attributed to "bursty" star formation (e.g. Weisz et al., 2012; Kauffmann, 2014; Shivaei et al., 2016; Smit et al., 2016). It is often asserted that the H$\alpha$ flux traces SFR over $\approx$ 10 Myr timescales and the UV continuum flux traces SFR over $\approx$ 200 Myr timescales (Kennicutt and Evans, 2012), in which case a galaxy with a

heightened H$\alpha$/UV flux ratio may have had a short burst of star formation within the last 10 Myr (Sparre et al., 2017). This effect could explain some of the scatter in Figure 2.13, given that $\mathrm{SFR_{SED}}$ is predominantly determined by the UV spectrum and its slope. However, binary stars can significantly extend the timescales over which ionizing photons are produced (Eldridge et al., 2017), and for the galaxies in our sample, we do not expect significant fluctuations in SFR on timescales shorter than $\sim$ 30 Myr, the typical central dynamical timescale; note also that the SEDs and FUV spectra are well-fit by models with constant star formation histories with a typical timescale of $10^8$ yr. Even in a scenario where bursts were important, we might expect to see a $\mathrm{SFR_{H\alpha}/SFR_{SED}}$ ratio that was systematically elevated, which is not the case, at least for the fiducial BPASS model employed in this paper.

Additionally, while the SMC curve comes the closest to producing consistent SFRs, and it provides the best fit to the SEDs of many of the galaxies in the sample, it may not be the most appropriate attenuation curve for every galaxy. As discussed in Section 2.3, 16% of galaxies in the sample are better fit by Calzetti et al. (2000) within the uncertainties.

Interestingly, this subset of galaxies better fit by the Calzetti et al. (2000) curve displays unique properties. A Kolmogorov-Smirnov (KS) test indicates that these galaxies and the remainder of the sample are drawn from different parent distributions in $12 + \log(\mathrm{O/H})_{\mathrm{O3N2}}$ ($3.2\sigma$), $\mathrm{SFR_{H\alpha}}$ ($2.8\sigma$), and $M_*$ ($7.0\sigma$). Histograms of these three properties for the subsample best fit by Calzetti et al. (2000) and the remainder of the sample are shown in Figure 2.15. Thus, it may be the case that this subsample is a population of galaxies distinct from the majority.

## 2.8 Summary and conclusions

We have presented an analysis of a sample of high-quality near-IR spectra of 317 galaxies at $2.0 \leq z \leq 2.7$ obtained as a part of KBSS-MOSFIRE (Steidel et al., 2014; Strom et al., 2017) in combination with complementary deep optical spectra obtained with Keck/LRIS for 270 of these galaxies. We have estimated $E(B-V)_{\mathrm{neb}}$ from the Balmer decrement and continuum attenuation from SED fits to broadband photometry [$E(B-V)_{\mathrm{SED}}$] as well as from stellar spectral synthesis model fits to composite rest-UV spectra [$E(B-V)_{\mathrm{cont}}$] in bins of $E(B-V)_{\mathrm{neb}}$, $12 + \log(\mathrm{O/H})_{\mathrm{O3N2}}$, $M_*$, $\mathrm{SFR_{H\alpha}}$, and $\mathrm{SFR_{SED}}$. We compared nebular and continuum estimates of dust reddening to each other and to gas-phase metallicity, $M_*$, and SFR. Finally, we compared H$\alpha$ and SED-based estimates of SFR. Our conclusions are as

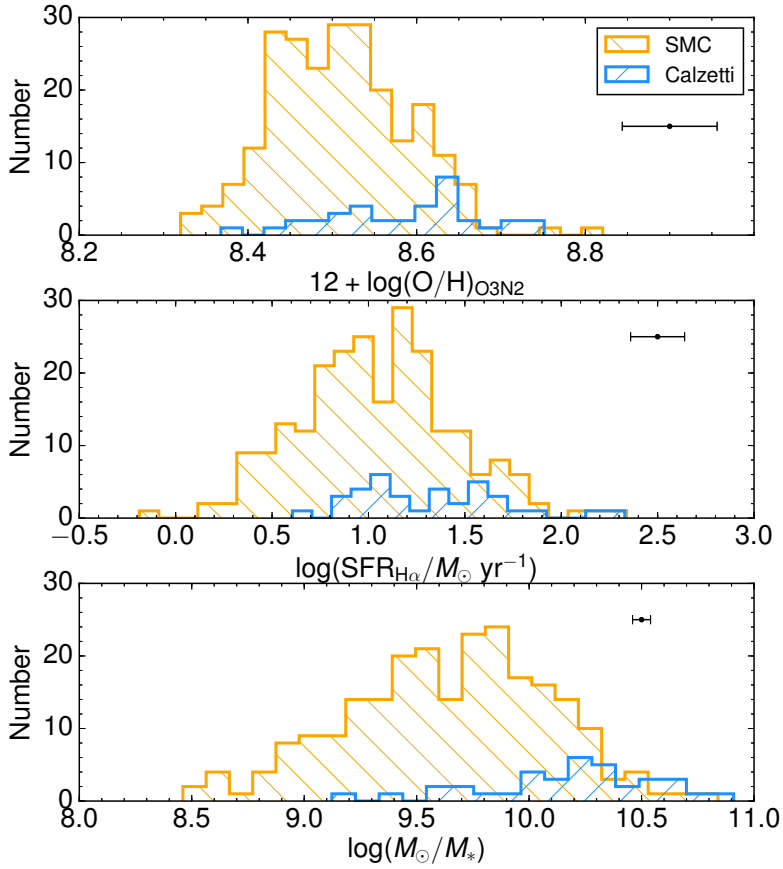


Figure 2.15: Histograms of 12 + log(O/H)$_{\rm O3N2}$, SFR$_{\rm H\alpha}$, and $M_*$ for the 16% of galaxies with SEDs best fit by the Calzetti et al. (2000) curve (blue) and the remainder of the sample (orange). Note that the former two quantities are independent of the assumed continuum attenuation curve, and we have shown that while the latter quantity requires an assumption of attenuation curve, it is nearly independent of this choice (see Figure 2.5).

follows:

- $E(B-V)_{\rm neb}$ is correlated with $E(B-V)_{\rm SED}$ for individual galaxies, albeit with large scatter, and there is generally larger reddening towards line-emitting regions. Fits of BPASSv2.2 stellar spectral synthesis models to composite rest-UV spectra in bins of $E(B-V)_{\rm neb}$ confirm that $E(B-V)_{\rm cont}$ is also correlated with $E(B-V)_{\rm neb}$. We find that when the SMC curve is applied to both lines and continuum, the discrepancy between $E(B-V)_{\rm neb}$ and $E(B-V)_{\rm SED}$ is larger on average than when the Calzetti et al. (2000) curve is applied to the continuum and the Cardelli et al. (1989) curve is applied to the nebular lines, due to the fact that the SMC curve is much steeper than the Calzetti et al.

(2000) curve in the UV but is similar to the Cardelli et al. (1989) Milky Way extinction curve in the optical. We argue that translations between nebular and continuum reddening such as that proposed by Calzetti et al. (2000) should be used with caution given the large scatter.

- $E(B-V)_{\rm neb}$ is correlated with gas-phase O/H measured from the O3N2 index, which is also sensitive to the massive stars ionizing the nebulae (e.g. Steidel et al., 2014; Steidel et al., 2016; Strom et al., 2017). The sense of the observed correlation is that the nebular reddening increases with increasing gas-phase O/H and/or decreasing excitation in the H II regions; the trend is similar to that observed at low redshift, but is offset by $\Delta \log(O/H) = 0.21$ dex toward lower inferred gas-phase oxygen abundance. Similarly, the relationship between $E(B-V)_{\rm neb}$ and $M_*$ is offset such that $z \sim 2.3$ galaxies have greater nebular reddening at a fixed stellar mass than $z \sim 0$ galaxies. We interpret the behavior as a natural consequence of lower dust/gas ratios but much higher gas fractions at high redshift.

- We find that the *continuum* reddening measured from the far-UV spectra is more strongly correlated with the inferred ionized gas-phase O/H (measured using the dust-insensitive O3N2 index) than the nebular reddening measured from the Balmer decrement toward the same H II regions. The strength of this correlation may be due to the fact that both the O3N2 index, used to measure $12 + \log(\mathrm{O/H})_{\rm O3N2}$, and the UV spectral slope, used to measure $E(B-V)_{\rm cont}$, are sensitive to the shape of the ionizing radiation field produced by the massive stars.

- The use of the Calzetti et al. (2000) attenuation curve in SED fitting in combination with the BPASSv2.2 $Z_* = 0.002$ SED models and corresponding conversion from H$\alpha$ luminosity to SFR produces inconsistent values of $\mathrm{SFR_{SED}}$ and $\mathrm{SFR_{H\alpha}}$ for all but the highest-$\mathrm{SFR_{H\alpha}}$ galaxies when the BPASSv2.2 $Z = 0.002$ binary star models are assumed, which several authors have found is best able to reproduce the observed constraints at high redshift. In contrast, the SMC curve produces consistent SFRs on average, and nominally the best fit to the full SEDs of the majority of the sample, and we argue that SMC is the most appropriate attenuation for the majority of the sample (except for the highest-mass galaxies). The large observed scatter between $\mathrm{SFR_{H\alpha}}$ and $\mathrm{SFR_{SED}}$ may be plausibly explained by variations in the intrinsic EUV-FUV spectra that are not fully accounted for with standard assumptions.

We emphasize that many of the relations between quantities involving continuum and nebular dust corrections depend sensitively on the details of the assumed continuum attenuation curve. In particular, the SMC curve predicts significantly smaller values of reddening and SFR than the "grayer" Calzetti et al. (2000) curve, and it provides a better fit for many of the galaxies in our sample at $z \sim 2.3$. However, a non-negligible fraction is better fit by the Calzetti et al. (2000) attenuation curve, and for these galaxies, the application of the SMC curve would lead to severe underestimates of reddening and SFR. Thus, care must be taken when selecting the most appropriate attenuation curve for a given galaxy at high redshift, and in general it is not a good assumption that the same attenuation curve applies to every galaxy at high redshift.

Perhaps just as importantly, due to large intrinsic variations in $L_{\mathrm{H}\alpha}/L_{\mathrm{UV}}$ modulated by stellar metallicity, IMF, and the importance of binaries, it is unlikely that the same conversion factor between H$\alpha$ luminosity and SFR applies to every galaxy at high redshift, and we argue that H$\alpha$-based SFRs are highly stochastic, and therefore remain a significant source of systematic errors in estimating SFRs of high-redshift galaxies.

*Chapter 3*

# GALACTIC OUTFLOWS IN $z \sim 2-3$ GALAXIES FROM KBSS-MOSFIRE

Theios, R. L. et al. (2020). "Galactic Outflows in z ∼ 2-3 Galaxies from KBSS-MOSFIRE". (in preparation).

Rachel L. Theios[1], Charles C. Steidel[1], Allison L. Strom[2], Yuguang Chen[1], Ryan F. Trainor[3], Gwen C. Rudie[2]

[1]Cahill Center for Astronomy and Astrophysics, California Institute of Technology, Pasadena, CA 91125, USA
[2]Carnegie Observatories, 813 Santa Barbara Street, Pasadena, CA 91101, USA
[3]Physics and Astronomy Department, Franklin & Marshall College, 415 Harrisburg Pike, Lancaster, PA 17603

**Abstract**

We present a detailed analysis of outflow signatures in the rest-UV and rest-optical spectra of $\sim 200$ $z \sim 2-3$ star-forming galaxies from KBSS-MOSFIRE. We measure outflow velocities from Si II and C II absorption profiles in composite rest-UV spectra grouped by five galaxy properties: stellar mass ($M_*$), dynamical mass ($M_{\rm dyn}$), star formation rate surface density ($\Sigma_{\rm SFR}$), BPT offset, and the O32 line ratio. We find that of these five parameters, only $\Sigma_{\rm SFR}$ shows a monotonic relationship with outflow properties. We compare several different velocity metrics, including the flux-weighted centroid velocity $v_{\rm cen}$ and the maximum blueshifted velocity extent $v_{\rm max}$, and conclude that the former is strongly affected by the presence of interstellar absorption with $\langle v \rangle = 0$. This symmetric absorption component spans nearly the same velocity extent as H$\alpha$ in both individual and composite spectra, suggesting that both are tracing the same gas. Finally, we search for broad emission components in the [O III]$\lambda$5008 line and find that the detectability of broad emission is strongly dependent on line signal-to-noise ratio. We conclude that UV absorption lines are a more reliable indicator of outflowing gas in high-redshift galaxies.

## 3.1 Introduction

Galactic winds driven by stellar feedback are crucial to our understanding of the evolution of galaxies and the surrounding intergalactic medium (IGM). In the local universe, winds with mass outflow rates ($\dot{M}$) roughly comparable to or exceeding the

star formation rate (SFR) have been observed in local starburst galaxies with intense star formation activity (see, e.g. Veilleux et al., 2005; Heckman and Thompson, 2017, for reviews). At higher redshifts up to $z \sim 2-3$, outflows are a near-ubiquitous feature of star-forming galaxies (e.g. Shapley et al., 2003; Steidel et al., 2010), which is not surprising given that this epoch represents the peak of cosmic star formation (Madau and Dickinson, 2014). By carrying metal-rich gas out of galaxies, galaxy-scale outflows are often invoked to explain the inefficiency of star formation at the low-mass end of the galaxy stellar mass function (e.g. Dekel and Silk, 1986; Somerville and Primack, 1999; Benson et al., 2003), as well as the tightness of the observed mass-metallicity relation (Tremonti et al., 2004; Chisholm et al., 2018) and metal abundances in the IGM (e.g. Pettini et al., 2003).

In the local Universe, multiwavelength observations have revealed that galactic winds are multiphase and kinematically complex. The prototypical example is the starburst galaxy M82, with a large-scale outflow that has been observed in multiple wavelength regimes: hard X-rays, likely tracing a hot fluid of stellar ejecta (Strickland and Heckman, 2007); soft X-rays and optical emission lines, whose kinematics suggest a bi-conical structure surrounding the hot outflowing fluid (Heckman et al., 1990; Shopbell and Bland-Hawthorn, 1998; Lehnert et al., 1999); and atomic and molecular phases, likely tracing the interaction of the wind and dense ambinet clouds (Contursi et al., 2013; Leroy et al., 2015). Observations of outflows in other local starburst galaxies are consistent with this picture (e.g. Armus et al., 1995; Strickland et al., 2004).

Galactic winds are also commonly traced by the blueshifts of interstellar (IS) absorption lines in the UV, originating in ionized and neutral outflowing gas seen against the stellar continuum. At low- and intermediate-redshift, numerous studies have found that outflow velocity scales with $M_*$ and SFR (e.g. Heckman et al., 2000; Martin, 2005; Rupke et al., 2005; Weiner et al., 2009; Erb et al., 2012; Martin et al., 2012; Chisholm et al., 2015; Trainor et al., 2015). Outflow velocity traced via absorption has also been found to be correlated with the star formation rate surface density $\Sigma_{\rm SFR}$ (Kornei et al., 2012; Heckman et al., 2015; Williams et al., 2015). This result is qualitatively consistent with the expectation for a momentum-driven wind, in that the momentum flux injected by stellar winds and core-collapse supernova ejecta is concentrated over a smaller area and is thus able to efficiently drive winds that escape the galaxy.

Fewer quantitative constraints exist at $z \sim 2-3$. Detailed studies of outflows in

individual lensed $z \sim 2$ galaxies (Pettini et al., 2002; Quider et al., 2009, 2010; Berg et al., 2018; Marques-Chaves et al., 2020) reveal a complex velocity structure—in all cases, IS absorption is distributed over a wide range of velocities, but differences in Ly$\alpha$ profiles and the inferred covering fraction of outflowing gas suggest that the structure of the outflow varies across the galaxy population. In a study of larger samples of outflows at $z \sim 2-3$, Steidel et al. (2010) found no significant trends between outflow velocity and $M_*$ or parameters related to star formation, in contrast to the situation in the local Universe.

The determination of outflow properties from IS absorption is subject to uncertainties due to the composition, geometry, and filling or covering fraction of the outflowing gas. In recent years, a growing body of work has instead focused on searching for galactic outflows via rest-frame optical emission lines such as H$\alpha$, H$\beta$, [N II], and [O III]. In M82 and other local starbursts, H$\alpha$ can be seen extending several kpc from the galaxy, in the direction perpendicular to the disk, and shows a double-peaked profile suggesting that the warm ionized gas lies on the surface of a biconical structure filled with the hot wind fluid seen in hard X-rays (Shopbell and Bland-Hawthorn, 1998). At high redshift, several authors have speculated that even in galaxies without an AGN, the faint, broad emission sometimes seen superimposed on a narrow Gaussian core may originate in the ionized phase of galactic winds. High-resolution spatially resolved observations of small samples of galaxies at $z \sim 2$ have noted broad emission arising from massive, highly star-forming clumps and galactic disks with high $\Sigma_{\rm SFR}$ (Genzel et al., 2011; Newman et al., 2012). Studies of broad emission in stacked spectra have found that the ratio of broad to narrow flux increases with stellar mass (Shapiro et al., 2009; Freeman et al., 2019) and SF properties (Newman et al., 2012; Förster Schreiber et al., 2019).

In studies of individual galaxies, however, broad emission is only detected in $\sim 10-20\%$ of the $z \sim 2$ galaxy population (Förster Schreiber et al., 2019; Freeman et al., 2019). Generally, very few trends are observed between the FWHM of the broad emission component and galaxy properties such as $M_*$ or SFR, and alternative scenarios cannot be conclusively ruled out (Freeman et al., 2019). The multiphase nature of galactic winds introduces significant uncertainties—even if broad emission does trace the ionized phase of the outflow, the fraction of mass carried in different outflow phases is largely unconstrained, and thus the connection between this broad, faint emission and the blueshifted IS absorption remains uncertain.

In this paper, we aim to bridge this gap by studying outflow signatures in the rest-

UV and rest-optical for the same galaxies. In particular, we examine a subsample of galaxies from the KBSS-MOSFIRE survey (Steidel et al., 2014; Strom et al., 2017) with both rest-optical spectra from Keck/MOSFIRE and high-quality rest-UV spectra from Keck/LRIS. The goal of this paper is twofold: to examine the physical properties of outflows at $z \sim 2-3$ and search for trends with outflow properties across parameter space; and to compare nebular emission lines in the rest-optical to rest-UV absorption lines in the same galaxies.

This paper is structured as follows: Section 3.2 describes the MOSFIRE and LRIS observations, the properties of the KBSS-LM dataset, and our methodology for stacking spectra and estimating the continuum level (discussed in more detail in Appendix 4.3). In Section 3.3 we investigate outflow properties inferred from rest-UV absorption. Section 3.4 discusses the kinematics of H$\alpha$ and [O III] line emission in KBSS galaxies. In Section 3.5 we discuss the implications of these results.

We adopt a $\Lambda$CDM cosmology with $H_0 = 70$ km s$^{-1}$ Mpc$^{-1}$, $\Omega_\Lambda = 0.7$, and $\Omega_\mathrm{m} = 0.3$. Conversion relative to solar metallicity assumes $Z_\odot = 0.0142$ (where $Z$ is the fraction of metals by mass), as in Asplund et al. (2009). Specific spectral features are referred to using their vacuum wavelengths.

### 3.2 Observations and galaxy sample

The galaxy sample discussed in this paper is taken from the KBSS-LRIS/MOSFIRE (KBSS-LM) project. This program was designed to follow up the deepest subsample of the KBSS-MOSFIRE survey (Steidel et al., 2014; Strom et al., 2017) with Keck/LRIS to obtain complementary high-quality rest-UV spectra and facilitate analysis of the joint rest-UV and rest-optical properties of these galaxies. The pilot survey conducted by Steidel et al. (2016), referred to as KBSS-LM1, includes the first two slitmasks observed as part of the KBSS-LM program, and details of the observing strategy and data reduction for KBSS-LM are described in that paper.

In brief, the highest-priority targets selected for LRIS observations were those which had already been observed with MOSFIRE in the J, H, and K bands. Here we focus on those galaxies with emission line measurements of the following lines: [O II]$\lambda\lambda$3727, 2729 in J band; H$\beta$ and [O III]$\lambda$5008 in H band; H$\alpha$ and [N II]$\lambda$6585 in K band. These criteria require the galaxies' redshfits to lie in the range $2.1 \lesssim z \lesssim 2.7$ so that the full complement of these strong rest-frame optical nebular emission lines is accessible in the near-IR atmospheric windows.

We also attempted to select galaxies such that the observed subsample spans the full

range of SFR, $M_*$, and metallicity observed in the KBSS-MOSFIRE dataset. As in Theios et al. (2019), we imposed a significance cut on the Balmer lines: $S/N > 3$ for the line ratio $I(\mathrm{H}\alpha)/I(\mathrm{H}\beta)$, to ensure that dust-corrected quantities such as the SFR are relatively well-constrained.

Finally, we included several galaxies that lack high-quality LRIS spectra but have been observed with KCWI (described in detail by Chen et al., in preparation). These criteria result in a sample of 121 galaxies (see Table 3.1). We note that all of the LRIS spectra used here have $R \sim 1350$, and the KCWI spectra have $R \sim 1800$.

**Derived galaxy properties**

Stellar masses were estimated for KBSS-MOSFIRE galaxies based on SED fits to broadband photometry, using reddened BPASSv2.2 (Stanway and Eldridge, 2018) binary models. The fitting process is described in detail in Theios et al. (2019); in brief, we assumed a constant star formation history, a stellar metallicity of $Z_* = 0.002$ ($Z_*/Z_\odot \approx 0.14$), the default BPASS IMF with an upper mass cutoff of $100 M_\odot$, a minimum age of 50 Myr, and an SMC attenuation curve. These models have been found by numerous studies (Steidel et al. 2016; Strom et al. 2017; Theios et al. 2019; see also Chisholm et al. 2019; Nanayakkara et al. 2019) to simultaneously match the rest-UV continuum and nebular lines better than single-star models. However, most studies thus far have determined stellar masses using the Bruzual and Charlot (2003) solar metallicity, single-star models assuming a Chabrier (2003) IMF, and Calzetti et al. (2000) attenuation curve. In general, changing the SED model and attenuation curve used in fitting results in a systematic offset in galaxy parameters, rather than a change in the rank-ordering. A detailed discussion of this topic is presented in Theios et al. (2019); in brief, the values of $M_*$ quoted in this work are lower by $\sim 0.45$ dex than those assuming the canonical combination of assumptions listed above. Wherever possible, we have included both estimates of stellar mass for reference.

SFRs were estimated from H$\alpha$ and dust-corrected as described by Theios et al. (2019). As in that paper, we used the $L_{\mathrm{H}\alpha}$-to-SFR conversion appropriate to the BPASS models (Stanway and Eldridge, 2018) combined with the SMC attenuation curve, which results in an $\sim 0.5$ dex offset to lower SFRs, relative to the conversion from Kennicutt and Evans (2012) that is commonly used in the literature (not accounting for differences in IMF; see Table 2 of Theios et al. 2019). Figure 3.1 shows the $M_*$-SFR relation for two subsamples of the full KBSS dataset: all galaxies

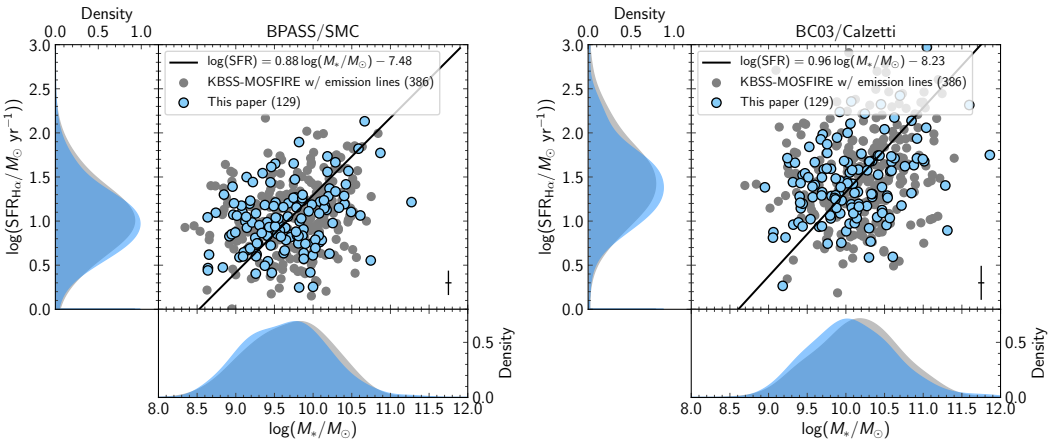


Figure 3.1: $M*$ vs. SFR for the full KBSS-MOSFIRE sample with S/N(BD) > 3 (the sample discussed by Theios et al. 2019), with the KBSS-LM sample overlaid in blue. A linear regression fit to the data is shown in black. Also shown are Gaussian kernel density estimations of each parameter. The left panel shows $M_*$ inferred from BPASSv2.2 SED fits and $\mathrm{SFR}_{\mathrm{H}\alpha}$ calculated using the conversion appropriate to the BPASSv2.2 models, assuming SMC attenuation and the default BPASS IMF. The right panel shows $M_*$ from Bruzual and Charlot (2003) SED fits and $\mathrm{SFR}_{\mathrm{H}\alpha}$ calculated using the Kennicutt and Evans (2012) conversion, assuming Calzetti et al. (2000) attenuation and a Chabrier (2003) IMF.

with robust H$\alpha$ and H$\beta$ measurements in gray, and the subset of 121 KBSS-LM galaxies in blue.

From $\mathrm{SFR}_{\mathrm{H}\alpha}$, we measured the star formation surface density $\Sigma_{\mathrm{SFR}}$ for the KBSS-LM dataset. Galaxy sizes for 74 of the 129 galaxies in the sample were measured from diffraction-limited imaging of the rest-frame optical with the *Hubble Space Telescope* (HST), as described in Law et al. (2012). For the subset without HST observations, we estimate the spatial extent of KBSS galaxies with the H$\alpha$ emission line. We estimated the spatial extent of lines by fitting the 2D profile of a line with a Gaussian, taking the projected profile along the slit, and correcting for the measured seeing on the same mask (see Strom et al., 2017, for details). The effective radius of the galaxy $r_{\mathrm{H}\alpha}$ was then computed from the spatial extent of the H$\alpha$ line and the measured nebular redshift, and used to estimate $\Sigma_{\mathrm{SFR}}$.

We measured dynamical masses using a method similar to Erb et al. (2006b). We assumed a disk geometry for gas-rich objects (which is likely appropriate for the majority of the sample), such that

$$M_{\mathrm{dyn}} = \frac{v_{\mathrm{true}}^2 r}{G}. \tag{3.1}$$

Erb et al. (2006b) estimated $v_{\rm true}$ by incorporating an average inclination correction $\langle v_{\rm true}\rangle = \frac{\pi}{2}\langle v_{\rm obs}\rangle$ and estimating $v_{\rm obs}$ from the velocity dispersion of the H$\alpha$ line, such that $v_{\rm obs} = \sqrt{2\ln 2}\sigma_{\rm H\alpha}$. The KBSS-MOSFIRE line fitting procedure discussed by Strom et al. (2017) fits the full complement of emission lines in a single band with Gaussian profiles constrained to have the same line width. The instrumental resolution can then be subtracted in quadrature.

In this paper, we analyze primarily composite spectra of subsets of the KBSS-LM sample, grouped by a variety of galaxy properties. As discussed in Section 3.1, literature studies of outflow velocities at both low and high redshifts have found conflicting trends with galaxy mass and SF properties. To investigate this, we divided the KBSS-LM sample into three groups each in $M_*$, $M_{\rm dyn}$, and $\Sigma_{\rm SFR}$ before generating the composite spectra.

We also considered trends between outflow velocity and the nebular emission line properties of the KBSS-LM sample. High-redshift galaxies have long been known to exhibit an offset in the N2-BPT plane relative to SDSS galaxies, towards higher [O III]/H$\beta$ and/or [N II]/H$\alpha$ ratios (e.g. Masters et al., 2014; Steidel et al., 2014; Shapley et al., 2015). Many studies have debated the origin of this offset; in particular, Steidel et al. (2014), Steidel et al. (2016), and Strom et al. (2017) came to the conclusion that the primary cause of the "BPT offset" is increased hardness of the ionizing radiation field at fixed N/O and O/H. We define "BPT offset" as the absolute distance in the BPT plane between each galaxy and the SDSS N2-BPT ridgeline, and assign a negative value if [O III]/H$\beta$ at fixed [N II]/H$\alpha$ is lower than the KBSS-MOSFIRE ridgeline. The BPT diagram for the KBSS-LM sample is shown in Figure 3.2.

Finally, we consider the O32 line ratio, defined as:

$$\mathrm{O32} \equiv \log([\mathrm{O\ III}](\lambda\lambda 4960, 5008)/[\mathrm{O\ II}](\lambda\lambda 3727, 3729)).$$

O32 is often used to calculate the ionization parameter $U \equiv n_\gamma/n_{\rm H}$, and unlike the BPT line ratios, is insensitive to differences in abundance patterns relative to $z \sim 0$.

In all cases, we divided the sample into three bins of each quantity, constrained to have a fixed width in parameter space, so the number of spectra contributing to each composite varies. A small number of galaxies did not have complete J, H, or K-band observations, and were excluded from the relevant composites. A summary of the KBSS samples, as well as the subsets of galaxies used for stacks, is given in Table 3.1.

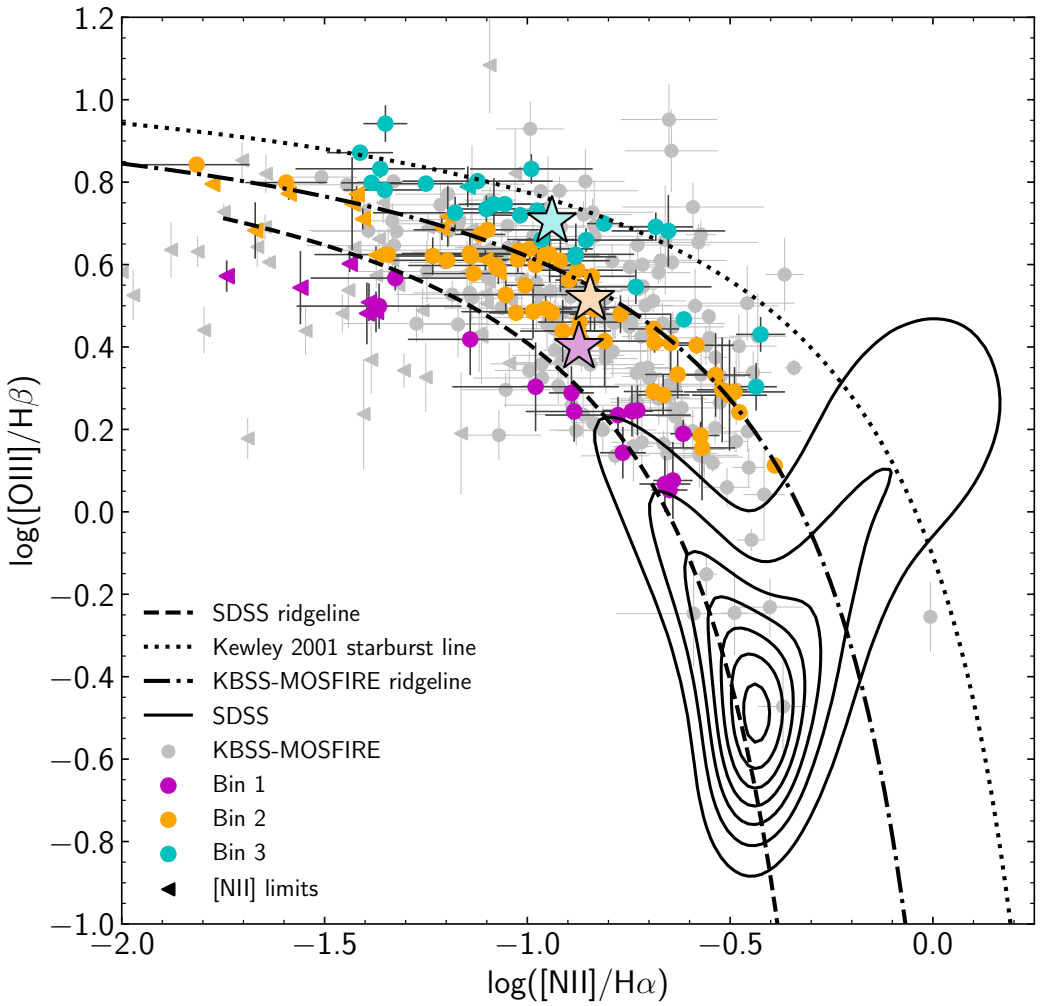


Figure 3.2: N2-BPT diagram for SDSS (black contours), the full KBSS-MOSFIRE sample (gray points), and the KBSS-LM sample (colored points). The KBSS-LM subsample discussed in this paper is sorted into three groups for generating composite spectra, here color-coded by the offset from the polynomial fit to the locus of SDSS galaxies on the N2-BPT, discussed by Steidel et al. (2014), Steidel et al. (2016), and Strom et al. (2017). The lowest-offset group (i.e. closest to SDSS) is shown in magenta, the median-offset group is shown in orange, and the highest-offset group is shown in cyan. Also shown are the Kewley et al. (2001) maximum starburst line and the polynomial fit to the locus of KBSS galaxies discussed by Strom et al. (2017). Upper limits in [N II]$\lambda$6585 ($2\sigma$) are shown as triangles, and line ratios measured from composite spectra are shown as stars.

Table 3.1: Sample Statistics.

| Galaxy Sample | $N_{\rm gal}$ | $\langle z_{\rm neb}\rangle$ | $\langle \log(M_*)\rangle^{\rm a}$ ($M_\odot$) | $\langle {\rm SFR}_{\rm H\alpha}\rangle$ ($M_\odot$ yr$^{-1}$) |
|---|---|---|---|---|
| KBSS-MOSFIRE ($2.1 \leq z \leq 2.7$) | 656 | 2.29 | 9.71 | 5.97 |
| $S/N({\rm H}\alpha/{\rm H}\beta) > 3$ | 386 | 2.30 | 9.74 | 10.42 |
| KBSS-LM | 121 | 2.36 | 9.67 | 9.65 |
| BPT | 111 | 2.36 | 9.68 | 9.93 |
| O32 | 103 | 2.38 | 9.68 | 9.93 |

[a]Assuming the fidicual BPASSv2.2 model used in this work, with SMC attenuation.

**Generating the composite spectra**

When searching for trends in high-redshift galaxy spectra, composites offer several advantages over individual spectra: first, averaging spectra together increases the continuum $S/N$ of the resulting spectrum, which allows for more accurate continuum normalization and measurement of weak spectral features, as well as mitigating uncertainties due to sky subtraction and other calibration errors. Second, combining spectra of galaxies along different lines of sight removes statistical uncertainty due to the Ly$\alpha$ forest, blueward of the Ly$\alpha$ line.

Composite rest-UV spectra were generated from the sample of 121 LRIS-B+R and KCWI spectra discussed above, using a method similar to that of Steidel et al. (2016). For each subsample, the spectra were shifted to the rest frame using $z_{\rm neb}$ measured from the corresponding rest-optical MOSFIRE spectra. The flux scale was adjusted correspondingly, and the spectra were averaged without additional weighting. As in Steidel et al. (2016), outlier pixels resulting from sky subtraction residuals near bright sky lines were excluded, but no other outlier rejection was performed. The $1\sigma$ error spectrum was propagated from the error spectra of the individual galaxies.

For comparison, we generated composite rest-optical MOSFIRE spectra for the same galaxies. The J, H, and K-band spectra were shifted into the rest frame using $z_{\rm neb}$ and the flux scale of each spectrum was adjusted to account for small differences in redshift across the sample. Bright sky lines were masked and the final stacked spectra were generated by averaging all unmasked pixels without weighting. The $1\sigma$ error spectra for each object were then propagated to produce a $1\sigma$ error spectrum for each composite.

**Continuum estimation**

The continuum levels of both the rest-UV and rest-optical spectra were estimated by fitting BPASSv2.2 model spectra to the data. The fitting procedure for the LRIS composite spectra is discussed in detail in Section 4.3; in brief, we used a $\chi^2$ minimization technique similar to that of Steidel et al. (2016) and Theios et al. (2019), allowing the stellar metallicity to vary. In this case, rather than reddening the models before fitting to the data, we normalized each model spectrum by a cubic spline fit to the data, smoothed with an iterative sigma clipping procedure. In effect, the normalized model spectra have the same overall shape as the data so that the $\chi^2$ minimization only fits the detailed spectral features such as stellar wind lines and photospheric absorption.

While this method marginalizes over the reddening $E(B-V)$, it may mitigate the effects of template mismatches if the flux calibration of the spectra is uncertain, particularly when combining spectra from LRIS-B and LRIS-R. We elect to use only models assuming a constant star formation history, with a stellar population age fixed to the median SED-inferred age of the galaxies contributing to each composite. However, the effects of allowing the stellar population age to vary in fitting are discussed in Section 4.3.

In the MOSFIRE spectra, the rest-optical continuum is generally faint and can be easily fitted by a low-order polynomial; however, we elected to use a model continuum in order to include the stellar Balmer absorption features, which vary with stellar mass and other properties. The BPASSv2.2 models were reddened and scaled to match the median of the observed data, excluding regions within 5 Å of strong emission lines. As with the LRIS spectra, we fixed the stellar population age of the model to the median SED-inferred age of the galaxies in the stack.

The final stacked rest-UV and rest-optical composite spectra and fitted continua are shown in Figure 3.3. Table 3.2 gives the parameters of the best-fit models for each composite. Although the primary spectral fitting method used in this paper does not allow for determination of $E(B-V)$, we also fit reddened BPASSv2.2 models to the data and measured $E(B-V)$ for comparison. Also shown in Table 3.2 are measurements of several of the strongest nebular emission lines in the far-UV spectra.

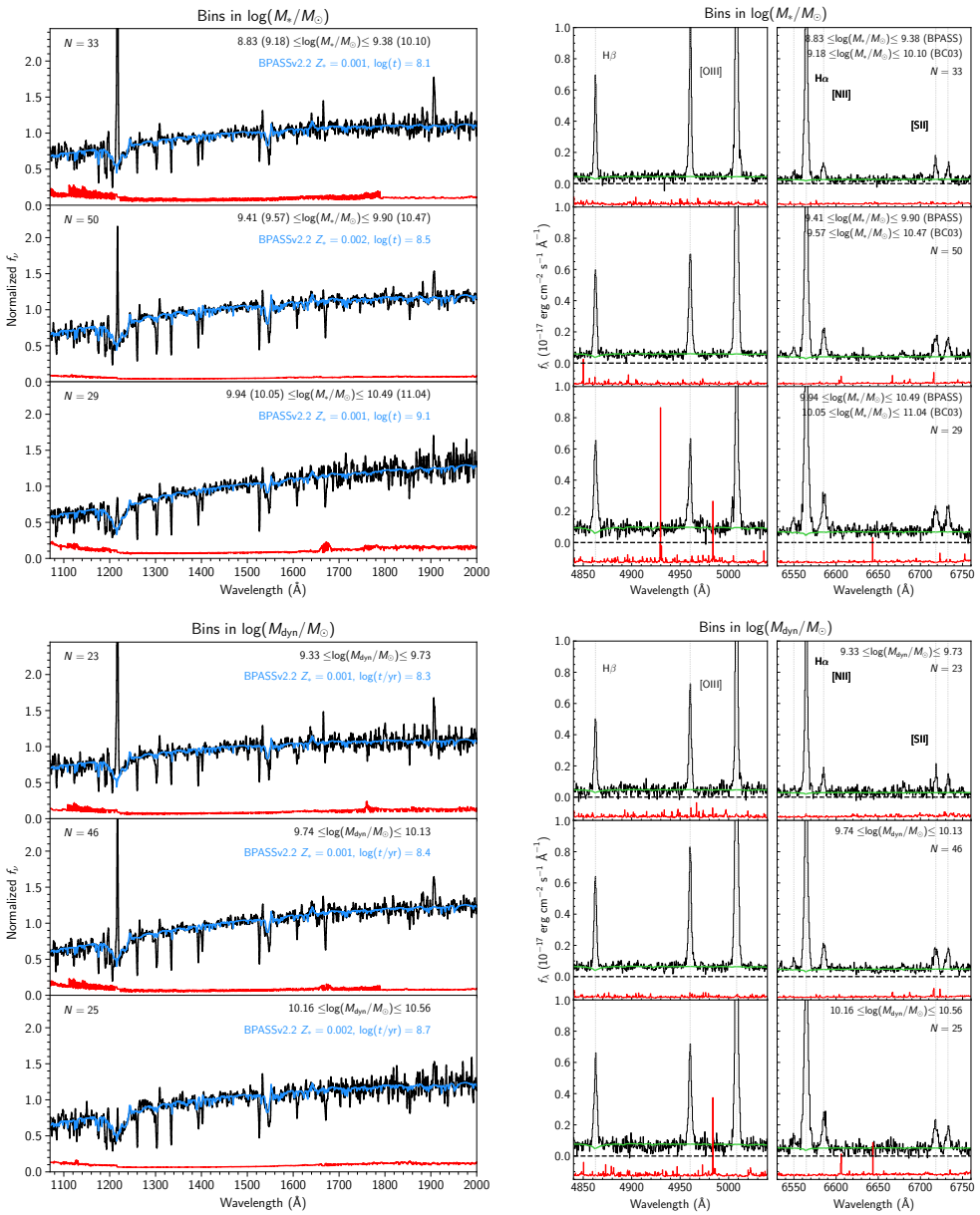


Figure 3.3: Composite rest-UV and rest-optical spectra in bins of $M_*$ and $M_{\rm dyn}$. Error spectra, propagated from the error spectra of the individual objects, are shown in red. Superposed are the best-fit population synthesis models from BPASSv2.2, as discussed in Section 3.2. The number of spectra contributing to each stack is shown on the top left.

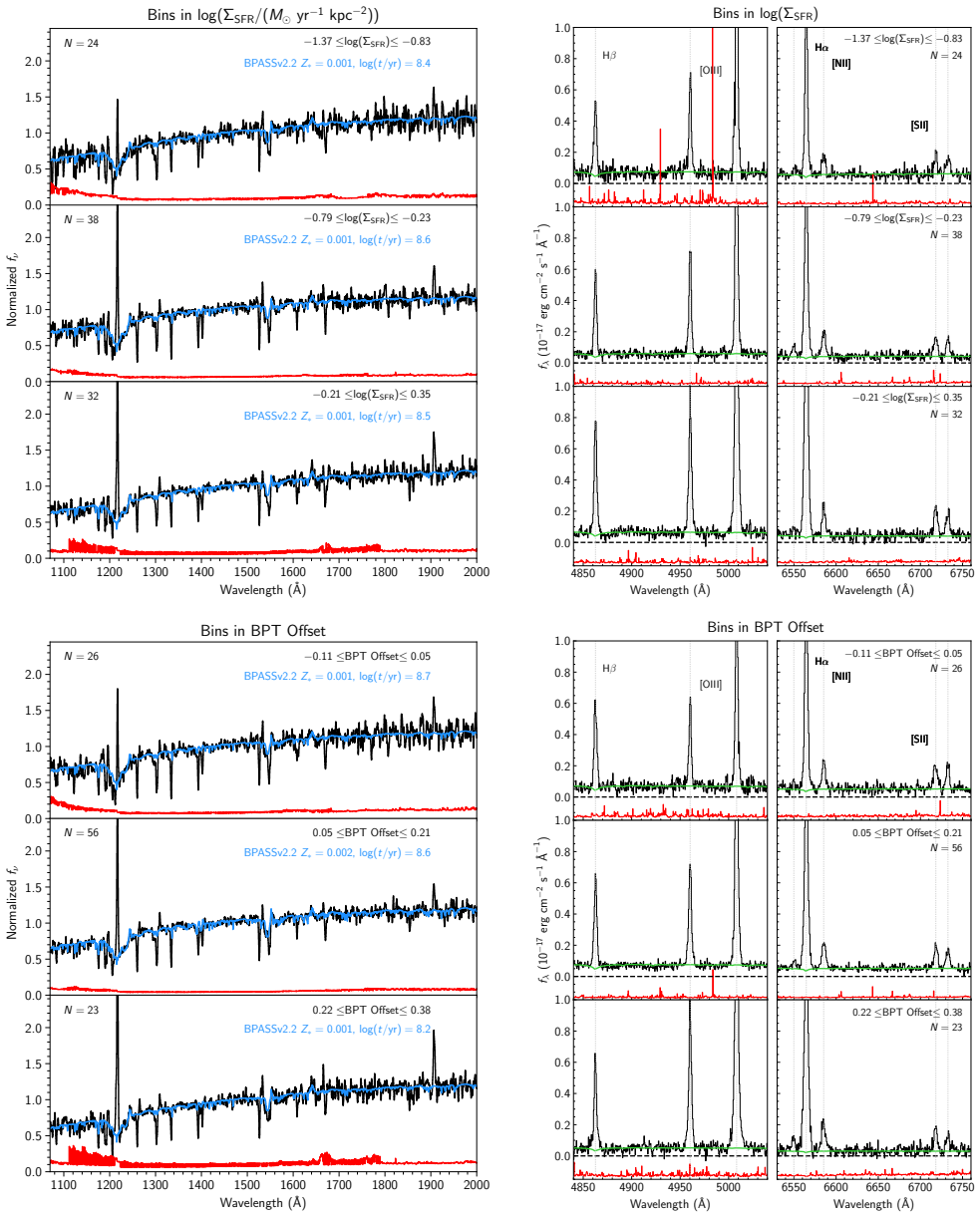


Figure 3.3: Composite rest-UV and rest-optical spectra in bins of $\Sigma_{\rm SFR}$ and BPT offset. (continued)

Table 3.2: Parameters of Stellar Model Fitting to Composite Spectra and Nebular Emission Line Fluxes.

| Median | Range | $Z_*$ | $E(B-V)$[a] | $\log(t/\mathrm{yr})$ | $W_{\mathrm{Ly}\alpha}$[b] | $F_{\mathrm{O\ III}]1661}$ | $F_{[\mathrm{O\ III}]1666}$ | $F_{[\mathrm{Si\ III}]1882}$ | $F_{[\mathrm{Si\ III}]\lambda1892}$ | $F_{\mathrm{C\ III}]\lambda1906}$ | $F_{[\mathrm{C\ III}]\lambda1908}$ |
|---|---|---|---|---|---|---|---|---|---|---|---|
| $\log(M_*/M_\odot)$[c] | | | | | | | | | | | |
| 9.14 (9.54) | (8.83, 9.38) | 0.001 | 0.08 | 8.10 | −14.85 | < 0.07 | 0.19 ± 0.02 | 0.04 ± 0.01 | 0.05 ± 0.01 | 0.17 ± 0.01 | < 0.02 |
| 9.69 (10.07) | (9.41, 9.90) | 0.002 | 0.08 | 8.50 | −0.52 | 0.04 ± 0.01 | 0.14 ± 0.01 | 0.08 ± 0.01 | 0.03 ± 0.01 | 0.15 ± 0.01 | < 0.02 |
| 10.15 (10.57) | (9.94, 10.49) | 0.001 | 0.10 | 9.10 | 4.68 | < 0.04 | < 0.06 | < 0.04 | < 0.04 | 0.1 ± 0.02 | < 0.04 |
| $\log(M_{\mathrm{dyn}}/M_\odot)$ | | | | | | | | | | | |
| 9.59 | (9.33, 9.73) | 0.001 | 0.07 | 8.30 | −13.49 | < 0.05 | 0.24 ± 0.02 | 0.14 ± 0.02 | 0.03 ± 0.01 | 0.18 ± 0.02 | 0.08 ± 0.02 |
| 9.94 | (9.74, 10.13) | 0.001 | 0.10 | 8.40 | −3.80 | 0.04 ± 0.02 | 0.06 ± 0.02 | < 0.03 | 0.06 ± 0.01 | 0.12 ± 0.01 | < 0.02 |
| 10.27 | (10.16, 10.56) | 0.002 | 0.08 | 8.70 | 4.52 | 0.03 ± 0.01 | 0.12 ± 0.01 | 0.09 ± 0.01 | < 0.03 | 0.1 ± 0.01 | < 0.03 |
| $\log(\Sigma_{\mathrm{SFR}})$ ($M_\odot$ yr$^{-1}$ kpc$^{-2}$) | | | | | | | | | | | |
| −1.08 | (−1.37, −0.83) | 0.001 | 0.10 | 8.40 | 3.11 | < 0.06 | 0.09 ± 0.02 | < 0.04 | < 0.06 | 0.16 ± 0.02 | < 0.03 |
| −0.48 | (−0.79, −0.23) | 0.001 | 0.07 | 8.60 | −3.58 | 0.04 ± 0.01 | 0.05 ± 0.01 | < 0.03 | 0.02 ± 0.01 | 0.07 ± 0.01 | < 0.02 |
| −0.04 | (−0.21, 0.35) | 0.001 | 0.09 | 8.50 | −8.12 | < 0.05 | 0.14 ± 0.01 | 0.09 ± 0.01 | < 0.05 | 0.18 ± 0.01 | < 0.04 |
| BPT Offset | | | | | | | | | | | |
| −0.06 | (−0.11, 0.05) | 0.001 | 0.08 | 8.70 | 2.67 | 0.04 ± 0.02 | 0.06 ± 0.02 | 0.08 ± 0.02 | < 0.04 | 0.2 ± 0.01 | < 0.03 |
| 0.15 | (0.05, 0.21) | 0.002 | 0.08 | 8.60 | −5.21 | 0.03 ± 0.01 | 0.06 ± 0.01 | 0.03 ± 0.01 | < 0.04 | 0.13 ± 0.01 | < 0.02 |
| 0.27 | (0.22, 0.38) | 0.001 | 0.10 | 8.20 | −11.97 | < 0.1 | 0.11 ± 0.03 | 0.06 ± 0.01 | < 0.03 | 0.23 ± 0.01 | 0.05 ± 0.01 |
| O32 | | | | | | | | | | | |
| 0.07 | (−0.13, 0.20) | 0.003 | 0.09 | 9.00 | 3.42 | 0.06 ± 0.02 | < 0.07 | < 0.04 | < 0.04 | 0.12 ± 0.02 | < 0.03 |
| 0.36 | (0.21, 0.50) | 0.001 | 0.09 | 8.40 | 0.74 | < 0.03 | 0.12 ± 0.01 | 0.04 ± 0.01 | < 0.02 | 0.11 ± 0.01 | 0.03 ± 0.01 |
| 0.72 | (0.54, 0.87) | 0.001 | 0.08 | 8.10 | −21.79 | 0.05 ± 0.02 | 0.12 ± 0.02 | 0.1 ± 0.01 | 0.04 ± 0.01 | 0.25 ± 0.01 | < 0.03 |

All fluxes are given in units of $10^{-17}$ erg cm$^{-2}$ s$^{-1}$; upper limits correspond to $2\sigma$.

[a] Assuming an SMC attenuation curve.

[b] Negative values indicate net emission.

[c] Assuming BPASSv2.2 SED models and SMC attenuation; the corresponding median $M_*$ assuming Bruzual and Charlot (2003) models and Calzetti et al. (2000) attenuation is given in parentheses.

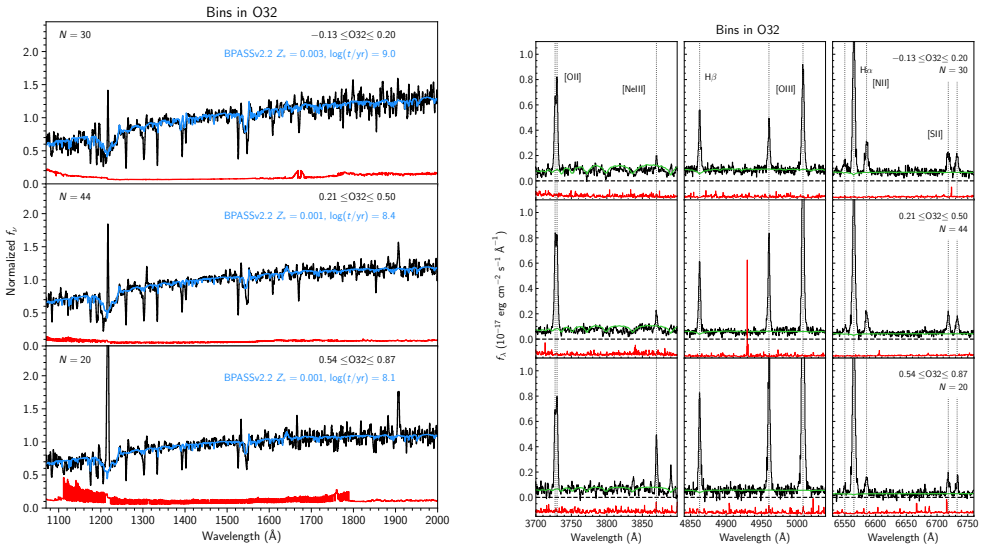


Figure 3.3: Composite rest-UV and rest-optical spectra in bins of O32. Here we have included the MOSFIRE J band spectra, which contain the [O II]$\lambda\lambda$3727, 3729 doublet used in calculating O32. (continued)

### 3.3 Outflow features in the rest-UV spectra

Interstellar absorption lines in rest-UV spectra of star-forming galaxies at $z \sim 2-3$ display a nearly ubiquitous blueshift relative to nebular emission lines, and are thus thought to trace outflowing gas. The H I Lyman series lines and singly ionized metal absorption lines probe cool outflowing gas, and the more highly ionized metal lines probe the ionized phase of the outflow. We focus on the low-ionization interstellar (LIS) absorption lines, as the strongest highly-ionized lines visible in these spectra (Si IV$\lambda$1393 and C IV$\lambda\lambda$1548, 1550) have a stellar contribution as well, which is difficult to disentangle from the interstellar absorption component. Since several of the LIS lines visible in the rest-UV spectra are blended, we selected three strong LIS transitions that are less likely to be contaminated by nearby features: Si II$\lambda$1260, C II$\lambda$1334, and Si II$\lambda$1526.

As discussed above, we use composite spectra to search for trends with the LIS lines as a function of five galaxy properties: $M_*$, $M_{\rm dyn}$, $\Sigma_{\rm SFR}$, BPT offset, and the O32 line ratio. For the purposes of analyzing the detailed interstellar absorption line profiles, we found that the BPASS model fits to the composite spectra did not always accurately fit the continuum shape in the immediate vicinity of the rest-UV interstellar absorption lines, perhaps due to mismatches in the detailed shape of nearby stellar features. We thus adjusted the continuum level by hand in the regions

surrounding the lines of interest.

Figure 3.4 shows the line profiles of Si II$\lambda$1260, C II$\lambda$1334, and Si II$\lambda$1526 for each composite. For comparison, the H$\alpha$ profiles from the corresponding MOSFIRE composite spectra are superposed.

For the purpose of measuring outflow velocities, we averaged these three line profiles together (hereafter referred to as the "average LIS profile") in order to increase the $S/N$ and mitigate uncertainties due to continuum placement. We spline-interpolated each portion of the spectrum onto the same velocity scale and averaged them together, inverse-variance weighting by the $1\sigma$ error level around each line.

**Velocity estimates**

While the asymmetry observed in rest-UV absorption line profiles is generally attributed to outflows, the specific metrics used to quantify outflow velocities vary in the literature. The absorption lines available for this purpose depend on the wavelength coverage of the spectrum, and each line poses its own unique set of challenges. Given that the radial distribution of the outflowing gas is unknown, any specific choice of "characteristic" outflow velocity is somewhat arbitrary, and care must be taken to account for systematic uncertainties when comparing velocity metrics quoted in the literature.

The simplest velocity measure is the flux-weighted centroid of the line profile. However, there are inherent complications with this approach, because the blueshifted component of the line profile, originating in an outflow, is likely superposed upon an ISM component at the systemic redshift (or zero velocity offset). Apparent trends between the line centroid and properties such as $M_*$ may be biased if the relative flux contained in the $\langle v \rangle = 0$ component varies with the galaxy properties being studied.

Some studies (e.g. Weiner et al., 2009) have attempted to separate the systemic and blueshifted components by fitting the red side of the line profile with a Gaussian and subtracting it from the full absorption profile. A simpler way around this problem is to measure the point at which the blue side of the absorption line profile meets the continuum, which should probe the extreme "tail" of the velocity distribution (e.g. Rivera-Thorsen et al., 2015). However, this method is subject to systematic uncertainties related to the placement of the continuum level.

In this paper, we compare these different approaches, and define the following velocity measures:

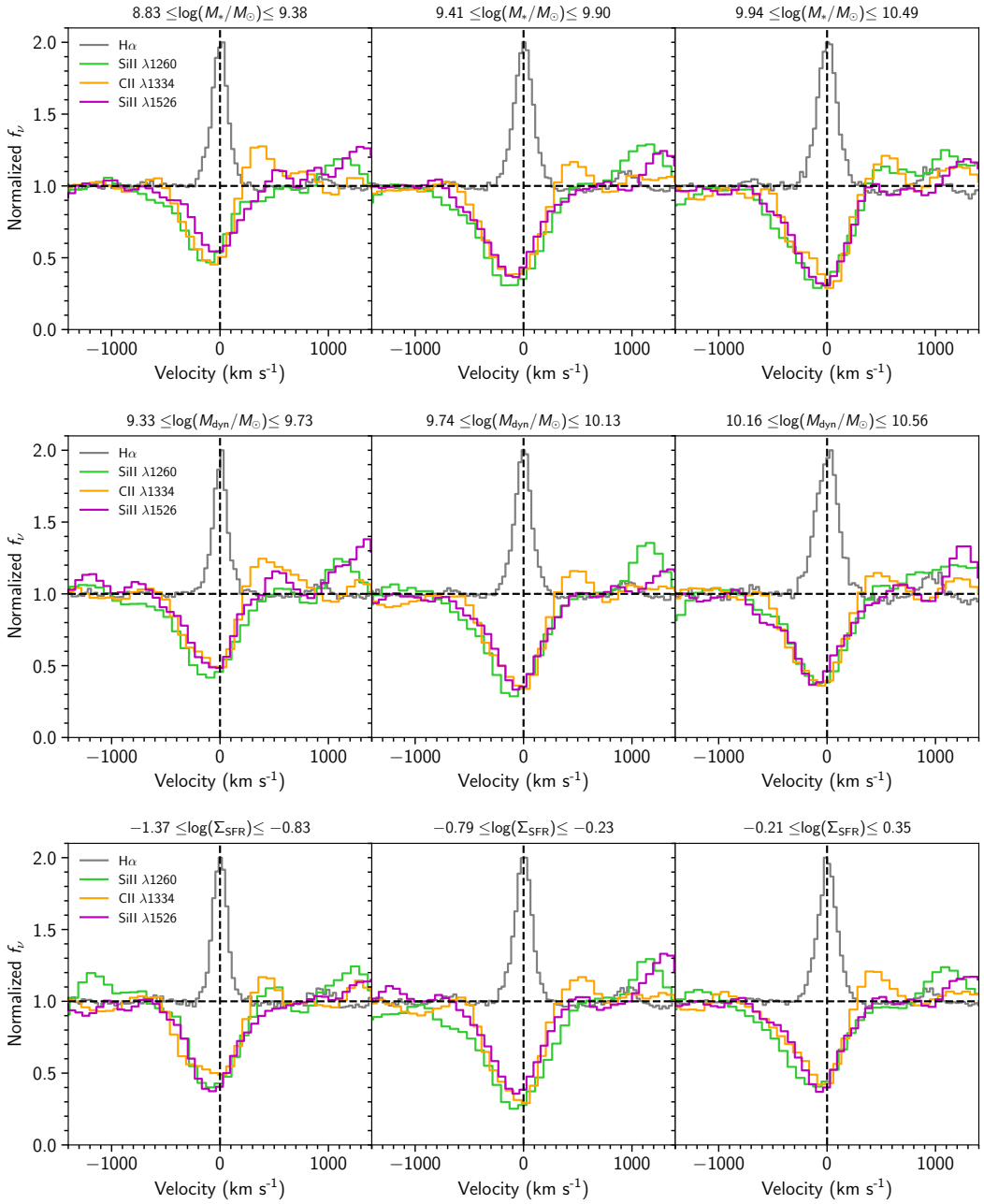


Figure 3.4: Velocity profiles of three rest-UV low-ionization interstellar absorption lines, for composite spectra in bins of (from top to bottom) $M_*$, $M_{\rm dyn}$, and $\Sigma_{\rm SFR}$. The spectra have been normalized by the best-fit BPASSv2.2 model as discussed in Section 3.2, and the excited fine structure emission lines corresponding to each resonance line (Si II*$\lambda$1265, C II*$\lambda$1335, and Si II*$\lambda$1533) are visible on the red side of each profile. The composite H$\alpha$ emission line for the same set of galaxies is shown for comparison, normalized by an arbitrary scaling factor.

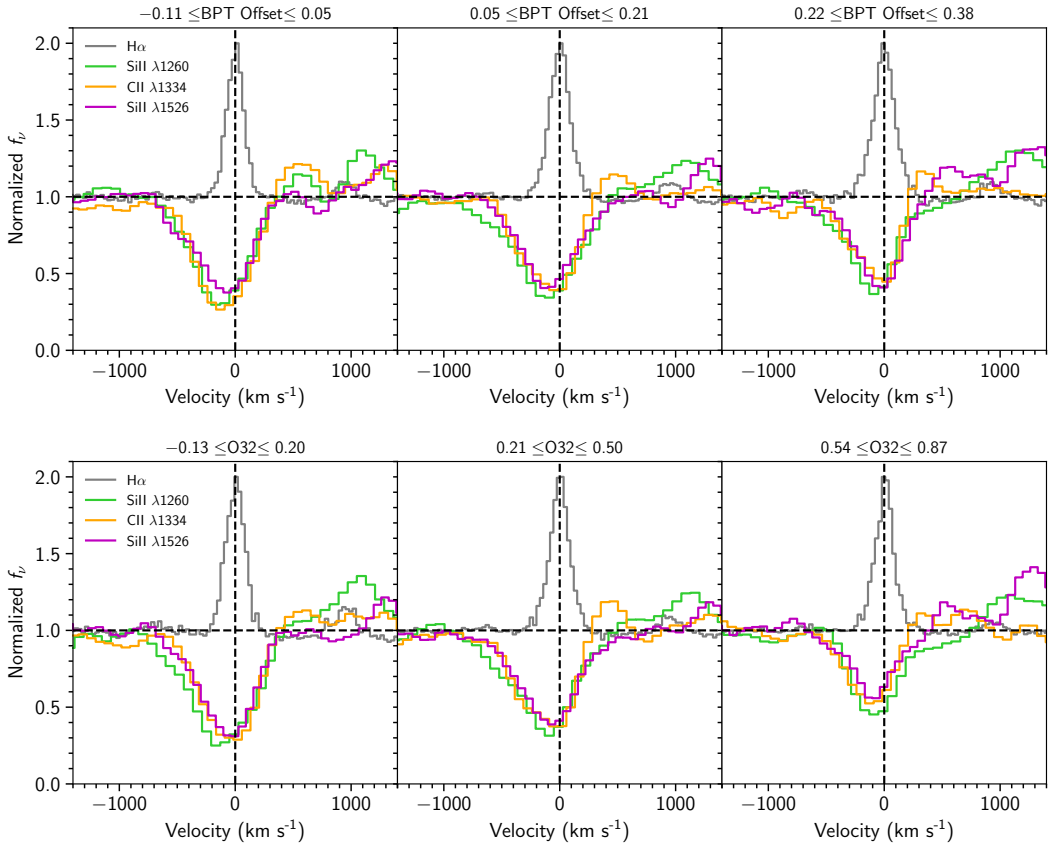


Figure 3.4: Velocity profiles of three rest-UV low-ionization interstellar absorption lines, for composite spectra in bins of BPT offset and O32. (continued)

1. *Centroid velocity* $v_{\rm cen}$. While the centroid of the absorption line profile may not reflect the true bulk velocity of the outflow, we have included it here as it is the most frequently used velocity metric.

2. *Maximum blue side velocity* $v_{\rm max}$. The point at which the absorption line profile meets the continuum on the blue side. We estimate $v_{\rm max}$ as the dispersion point (at $v < 0$) where the normalized flux is closest to $f_\nu = 1$.

3. *Residual centroid* $\langle v_{\rm out} \rangle$. Assuming that the $\langle v \rangle = 0$ component exhibits an approximately Gaussian absorption line profile, we fit a single Gaussian to the $v \geq 0$ portion of the absorption line profile. We then subtract the symmetric Gaussian with $\langle v \rangle = 0$ from the line profile, where the residual absorption represents the net outflow and $\langle v_{\rm out} \rangle$ is the flux-weighted centroid of the residual absorption profile.

Figure 3.5 shows the average LIS profile, zero-velocity ISM component fit, and residual for each composite spectrum, with the H$\alpha$ profile shown for comparison. We measured velocities for each composite, and the results are presented in Table 3.3, along with the equivalent width of the blueshifted residual component, and the Gaussian velocity widths of H$\alpha$ and the $\langle v \rangle = 0$ absorption component.

**Results**

Figure 3.5 shows that in every composite, the residual from the zero-offset Gaussian fit is consistent with zero on the red side of the spectrum, indicating that a Gaussian velocity distribution accurately describes the $\langle v \rangle = 0$ absorption component. Every stack shows a blueshifted residual from this fit, suggesting that outflows are present in the vast majority of galaxies at $z \sim 2 - 3$ regardless of other galaxy properties.

Among the five quantities used to generate stacks, $\Sigma_{\rm SFR}$ shows the strongest correlation with $\langle v_{\rm out} \rangle$, $v_{\rm max}$, and the equivalent width of the blueshifted residual, $W_{\rm out}$. This result is consistent with the correlation between outflow velocity and $\Sigma_{\rm SFR}$ found by multiple authors across a range of redshifts (Kornei et al., 2012; Heckman et al., 2015; Williams et al., 2015). Once differences in SFR calibrations have been accounted for, the large majority of our sample lies above the $\Sigma_{\rm SFR} \gtrsim 0.1\, M_\odot\, {\rm yr}^{-1}\, {\rm kpc}^{-2}$ threshold for driving winds, proposed by Heckman (2002).

The trends observed with $M_*$ and $M_{\rm dyn}$ are less clear-cut. While $\langle v_{\rm out} \rangle$ increases monotonically with $M_*$, no clear trends are observed between $M_*$ and $v_{\rm max}$, or between $M_{\rm dyn}$ and any velocity metric. No trends are apparent between outflow properties and BPT offset or O32, although in several cases (most notably the middle bin in O32) there is evidence for a high-velocity wing much fainter than that of the high-$\Sigma_{\rm SFR}$ composite.

Interestingly, Figure 3.5 and Table 3.3 show that the velocity width of the $\langle v \rangle = 0$ absorption component is consistently larger than that of H$\alpha$ for the same galaxies by a factor of $\sim 1.5$, even when the differences in instrumental resolution between MOSFIRE and LRIS are accounted for ($R = 3690$ for MOSFIRE K-band and $R \sim 1350$ for LRIS-B, with the configurations used in this work). However, it can be seen from Figure 3.5 that while the core of H$\alpha$ is generally much narrower than that of the LIS profile, both lines meet the continuum (on the red side) at approximately the same place in every composite.

To quantify this effect, we estimated the continuum-crossing point on the red side of both lines in the same manner as $v_{\rm max}$, by measuring the velocity at which the flux

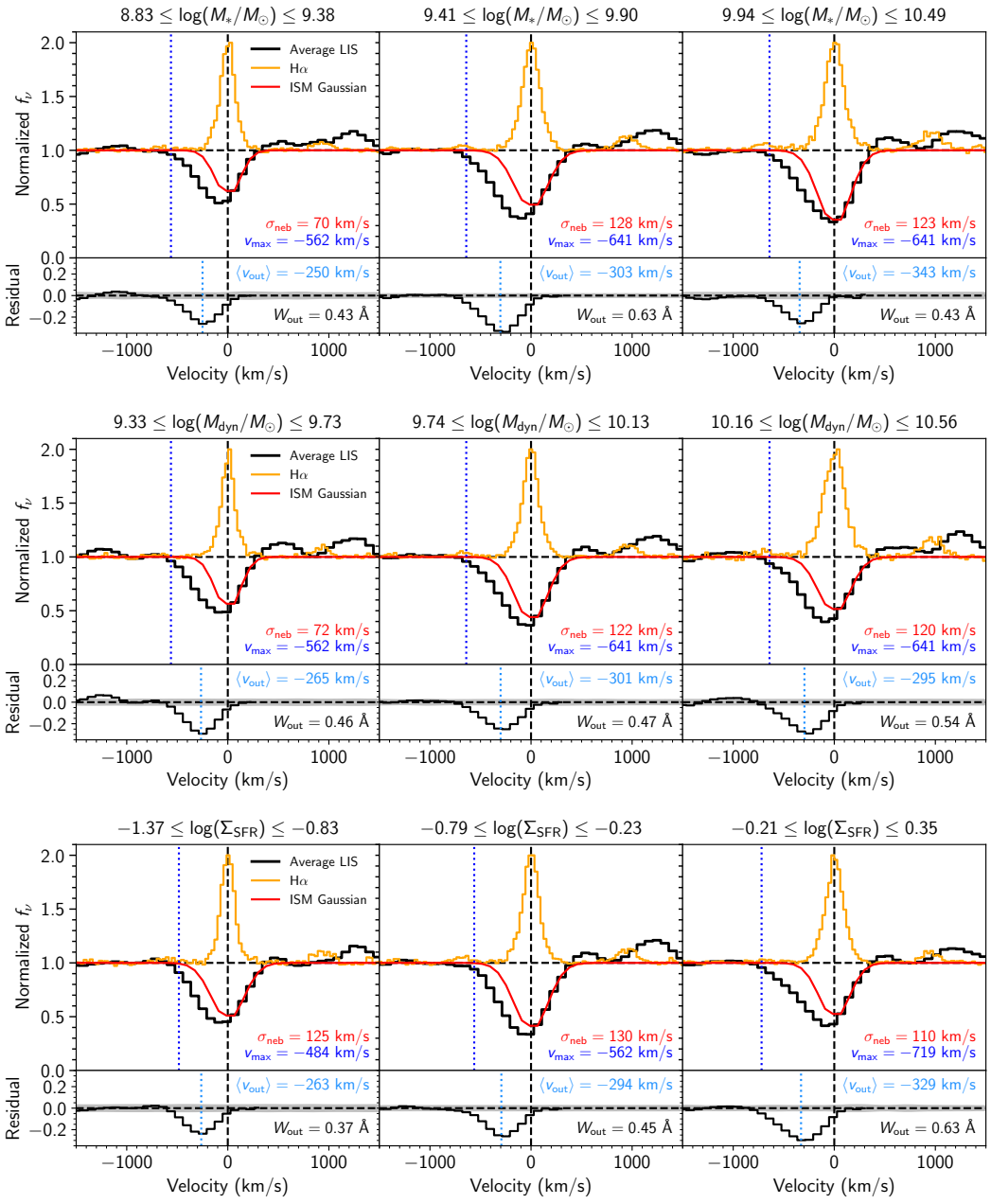


Figure 3.5: Averaged LIS profile for composite spectra in bins of (from top to bottom) $M_*$, $M_{\rm dyn}$, and $\Sigma_{\rm SFR}$, with the composite H$\alpha$ emission line for the same set of galaxies shown in orange. Shown in red is a Gaussian fit to the red side of the line, assumed to originate from a systemic ISM component. The bottom panel is the residual of this fit, with the $1\sigma$ error level of the averaged line profile shown in gray. The blue dashed lines indicate the maximum outflow velocity $v_{\rm max}$, and the centroid of the residual $\langle v_{\rm out} \rangle$, assumed to trace the bulk outflow velocity of the low-ionized gas. Note that the portion of the averaged LIS profile on the red side with $f_\nu > 1$ represents the averaged contribution of three excited fine structure lines: Si II*$\lambda$1265, C II*$\lambda$1335, and Si II*$\lambda$1533.

Table 3.3: Velocity Estimates From Composite Spectra.

| Median | Range | $v_{\rm max}$ (km/s) | $v_{\rm cen}$ (km/s) | $\langle v_{\rm out}\rangle$ (km/s)[a] | $W_{\rm resid}$ (Å) | $W_{\rm sys,abs}$ (Å) | $\sigma_{\rm sys,abs}$ (km/s)[b] | $\sigma_{\rm H\alpha}$ (km/s)[b] |
|---|---|---|---|---|---|---|---|---|
| $\log(M_*/M_\odot)$[c] | | | | | | | | |
| 9.14 (9.54) | (8.83, 9.38) | −562 | −190 | −250 | 0.43 | 0.53 | 70 | 67 |
| 9.69 (10.07) | (9.41, 9.90) | −641 | −193 | −303 | 0.63 | 0.91 | 128 | 84 |
| 10.15 (10.57) | (9.94, 10.49) | −641 | −213 | −343 | 0.43 | 1.15 | 123 | 92 |
| $\log(M_{\rm dyn}/M_\odot)$ | | | | | | | | |
| 9.59 | (9.33, 9.73) | −562 | −193 | −265 | 0.46 | 0.61 | 72 | 60 |
| 9.94 | (9.74, 10.13) | −641 | −205 | −301 | 0.47 | 0.98 | 122 | 74 |
| 10.27 | (10.16, 10.56) | −641 | −195 | −295 | 0.54 | 0.84 | 120 | 103 |
| $\log(\Sigma_{\rm SFR})$ ($M_\odot$ yr$^{-1}$ kpc$^{-2}$) | | | | | | | | |
| −1.08 | (−1.37, −0.83) | −484 | −96 | −263 | 0.37 | 0.87 | 125 | 60 |
| −0.48 | (−0.79, −0.23) | −562 | −158 | −294 | 0.45 | 1.07 | 130 | 75 |
| −0.04 | (−0.21, 0.35) | −719 | −237 | −329 | 0.63 | 0.79 | 110 | 84 |
| BPT Offset | | | | | | | | |
| −0.06 | (−0.11, 0.05) | −641 | −193 | −306 | 0.64 | 0.91 | 109 | 68 |
| 0.15 | (0.05, 0.21) | −641 | −197 | −297 | 0.53 | 0.90 | 131 | 85 |
| 0.27 | (0.22, 0.38) | −562 | −195 | −279 | 0.44 | 0.65 | 68 | 90 |
| O32 | | | | | | | | |
| 0.07 | (−0.13, 0.20) | −641 | −215 | −317 | 0.48 | 1.17 | 130 | 80 |
| 0.36 | (0.21, 0.50) | −719 | −240 | −319 | 0.65 | 0.82 | 105 | 82 |
| 0.72 | (0.54, 0.87) | −484 | −87 | −221 | 0.42 | 0.48 | 91 | 73 |

[a] Measurements of $\langle v_{\rm out}\rangle$ are quantized to the nearest pixel.

[b] Both $\sigma_{\rm sys,abs}$ and $\sigma_{\rm H\alpha}$ are corrected for the instrumental profiles of LRIS and MOSFIRE, respectively.

[c] Assuming BPASSv2.2 SED models and SMC attenuation; the corresponding median $M_*$ assuming Bruzual and Charlot (2003) models and Calzetti et al. (2000) attenuation is given in parentheses.

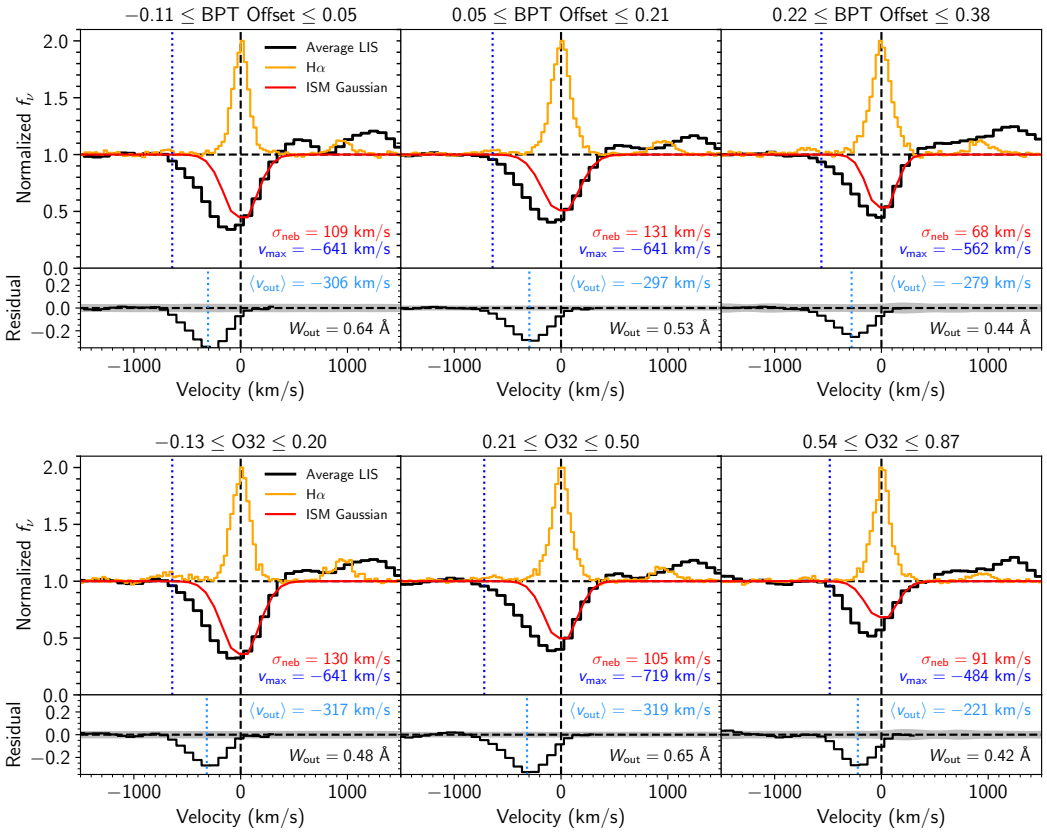


Figure 3.5: Averaged LIS profile for composite spectra in bins of BPT offset and O32. (continued)

reaches $f_\nu = 1$. In the case of H$\alpha$, we first convolved the spectrum with a Gaussian kernel to match the instrumental resolution of LRIS, and measured the point at which $f_\nu = 0$, since the continuum was subtracted from the emission-line spectra. In every composite, the differences in continuum-crossing velocities between the LIS lines and H$\alpha$ are smaller than the velocity sampling of the LRIS spectra, suggesting that the nebular emission and $\langle v \rangle = 0$ LIS absorption are tracing the same ISM gas, and the velocity extent reflects the range of velocities in the galaxy ISM.

It is worth noting that while $\langle v_{\rm out} \rangle$ and $v_{\rm max}$ generally scale proportionally to one another, $v_{\rm cen}$ does not, nor does the equivalent width of the blueshifted residual component, $W_{\rm resid}$. Given that the strength of the $\langle v \rangle = 0$ absorption component varies with mass, the overall centroid of the absorption profile is likely modulated by a combination of factors, including the strength of absorption in the ambient and outflowing components, which may not be correlated at all. We return to this issue in Section 3.5.

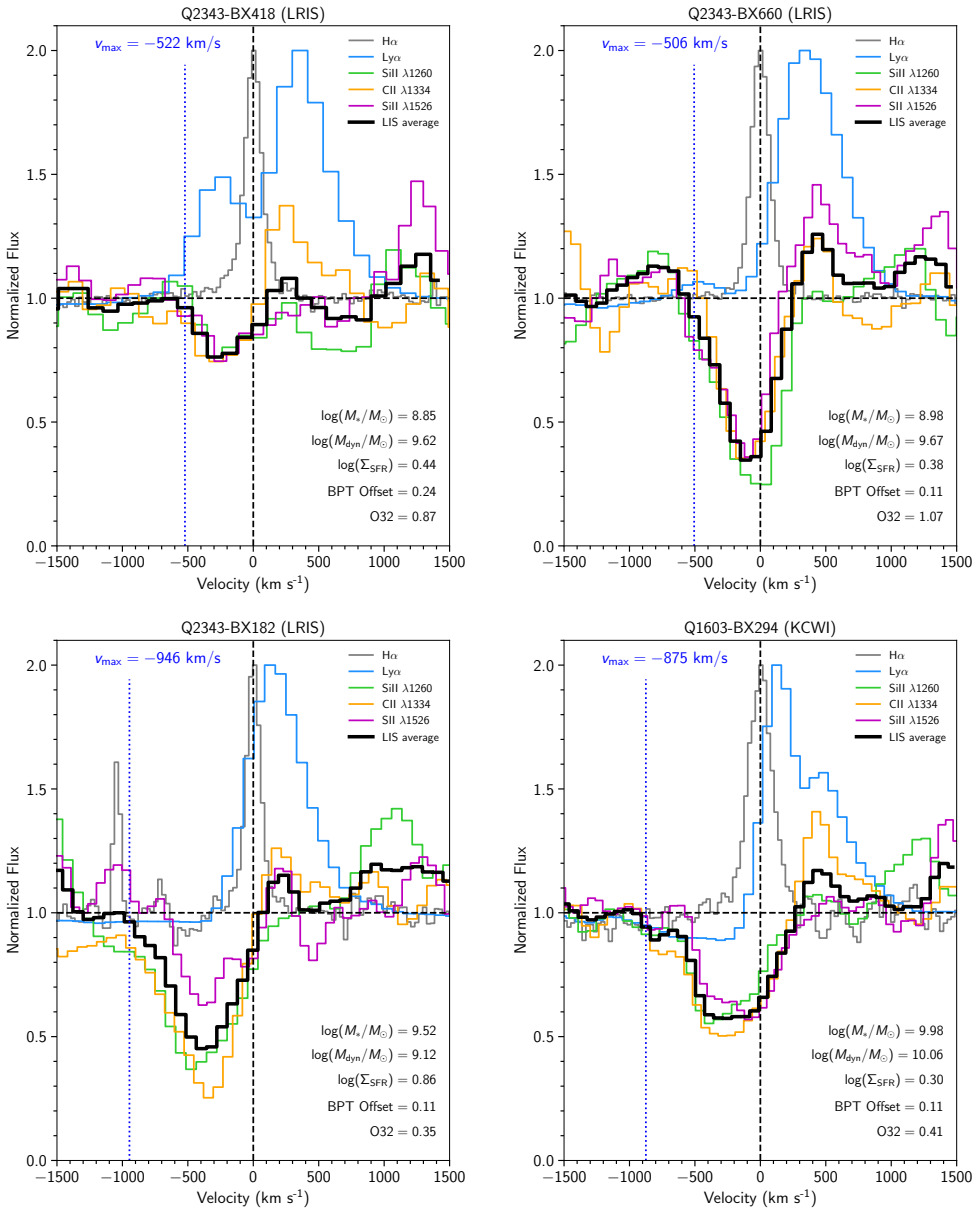


Figure 3.6: Velocity profiles of three rest-UV low-ionization interstellar absorption lines, Ly$\alpha$, and H$\alpha$ for individual galaxy spectra. The H$\alpha$ and Ly$\alpha$ fluxes have been normalized by an arbitrary scaling factor. The averaged LIS profile is shown in black, as in 3.5, and $v_{\rm max}$ is shown as a blue dotted line.

### Individual spectra

A small subset of the KBSS-LM rest-UV spectra have sufficiently high continuum $S/N$ that they can be analyzed individually, which we discuss in this section. These galaxies are naturally biased towards high values of $\Sigma_{\rm SFR}$, and thus are not as useful in characterizing trends among typical $z \sim 2-3$ galaxies. However, they

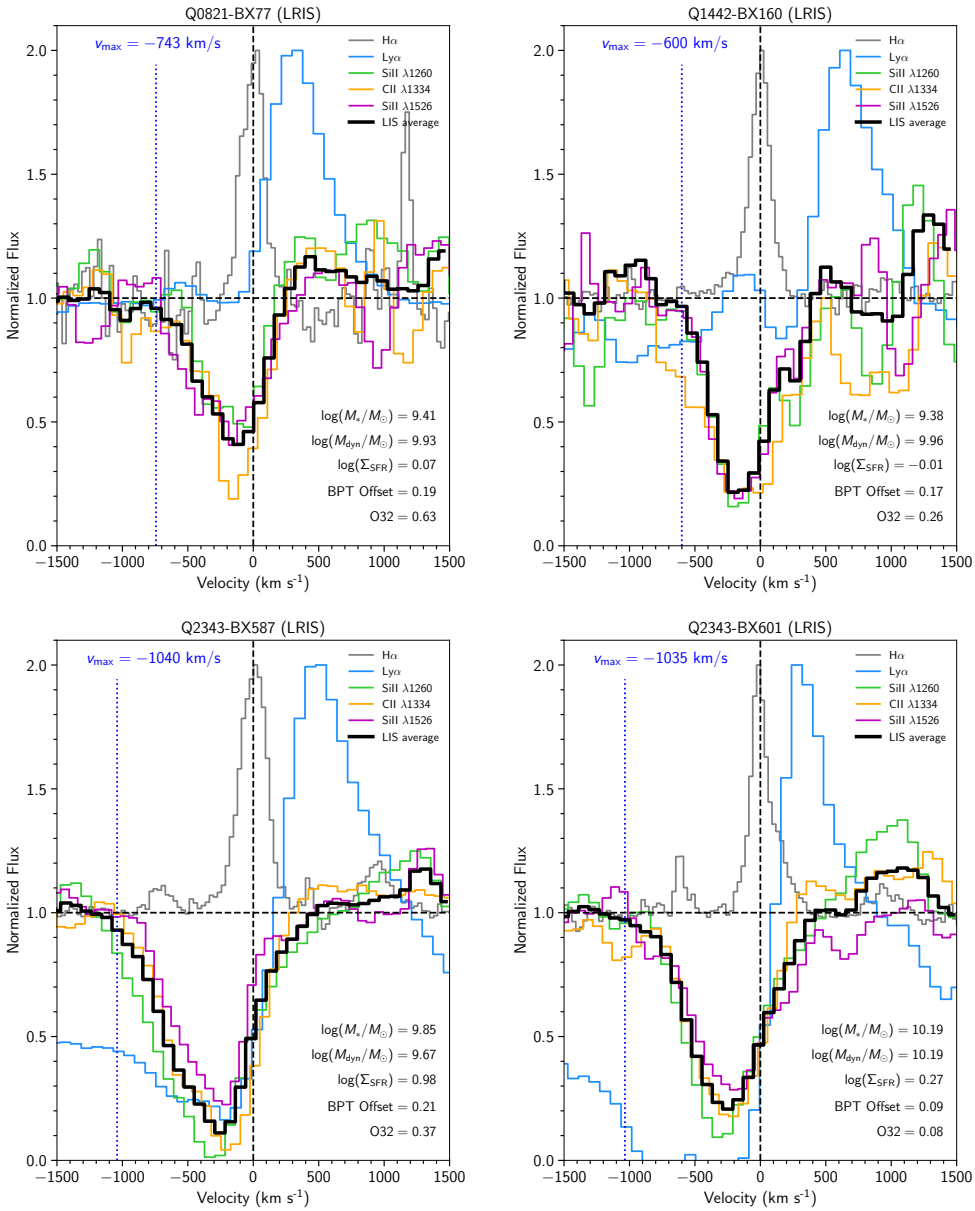


Figure 3.6: Continued.

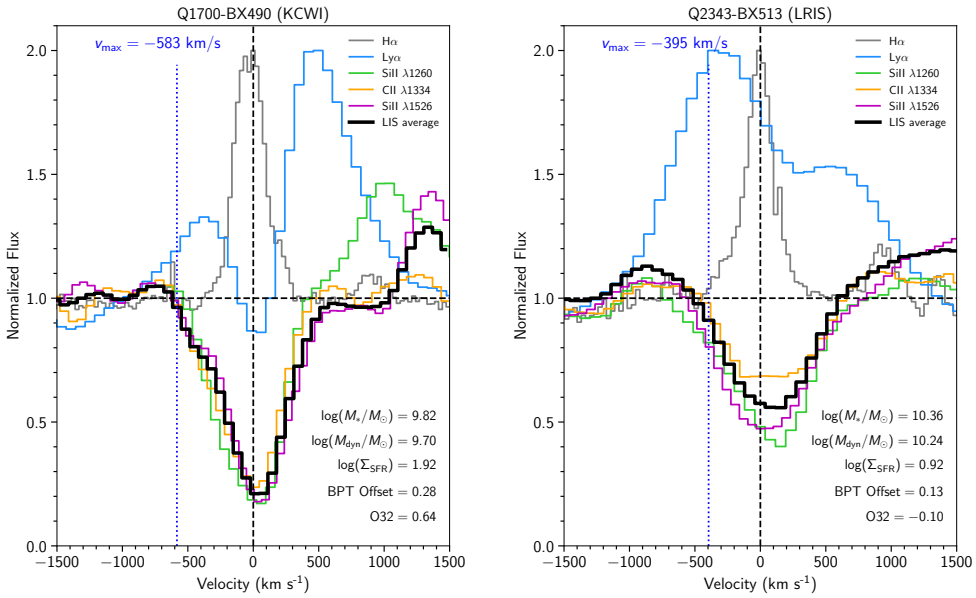


Figure 3.7: Same as Figure 3.6, for two galaxies with broadened absorption line profiles on the red side, suggesting the presence of inflows. Q1700-BX490 also shows absorption from an intervening low-redshift source.

do showcase the diversity of outflow properties seen even among galaxies which otherwise occupy similar regions of parameter space. Figure 3.6 shows the LIS absorption line profiles of eight KBSS-LM galaxies (observed with either LRIS or KCWI), along with H$\alpha$ and Ly$\alpha$, the latter of which can be seen in emission, absorption, or a combination of both. Also indicated is $v_{\rm max}$, measured in the same manner as the composites.

The first of these galaxies is Q2343-BX418, which has been extensively studied in the literature (e.g. Erb et al., 2010; Steidel et al., 2014; Erb et al., 2018), and shows an extended Ly$\alpha$ halo, with double-peaked emission lines that vary as a function of radius from the central galaxy. In the "down-the-barrel" spectrum shown here, Ly$\alpha$ is double-peaked with non-zero emission at the systemic redshift, suggesting that the gas is optically thin. Additionally, the strengths of the Si II* $\lambda$1265 and Si II* $\lambda$1533 excited fine-structure lines are comparable to their corresponding resonance absorption transitions. This is as we might expect for a scenario in which the fine-structure emission originates in photon scattering in an isotropic outflow; this result may indicate that the entire line-emitting region is captured by the slit (see, e.g. Steidel et al., 2010; Prochaska et al., 2011; Erb et al., 2012; Scarlata and Panagia, 2015). The $v_{\rm max}$ measured here is lower than the majority of the sample, although

this may simply be due to the weak absorption profile; the high-O32 composite in Figure 3.5 shows similarly weak LIS absorption with a broad high-velocity wing on the blue side, which may be too faint to observe in an individual galaxy. Q2343-BX660 is similar to BX418 in $M_*$, $\Sigma_{\rm SFR}$, and BPT offset, with $v_{\rm max}$ very close to that of BX418. However, it shows stronger LIS absorption line profiles, and evidence of optically thick gas. Both Q2343-BX418 and Q2343-BX660 have measurements of oxygen abundance using the "direct method;" see Steidel et al. (2014).

In the composite spectra shown in Figure 3.4, the low-$M_*$ stack shows the most obvious evidence for optically thin outflowing gas; i.e. the Si II$\lambda$1260 profile is deeper than Si II$\lambda$1526. However, among the galaxies shown in Figure 3.6, several galaxies have optically thin Si II profiles at $v < 0$, over a wide range of galaxy properties. Furthermore, in these cases (e.g. Q2343-BX182, Q2343-BX587), it is clear that since Si II is optically thin out to high velocities, measures of $v_{\rm max}$ would then depend on $Nf\lambda$ of the transition chosen.

Several of the galaxies shown in Figure 3.6 are characteristic of the sample as a whole, yet they still exhibit a variety of absorption line strengths and velocities. As in the composites shown in Figure 3.5, however, the averaged LIS profile and H$\alpha$ reach the continuum level at roughly the same velocity on the red side (i.e. $v < 0$). In fact, this appears to be the *only* feature that all of these galaxies have in common.

However, there are several exceptions to this rule. Figure 3.7 shows two of the most unusual spectra in the KBSS-LM sample, whose kinematics appear to be inverted relative to the rest of the KBSS sample. Q1700-BX490 shows strong, nearly symmetric LIS absorption and double-peaked Ly$\alpha$ emission. Q2343-BX513 is the only galaxy in the KBSS-LM sample with net blueshifted Ly$\alpha$ emission; it also shows LIS absorption that is broader on the red side. In both cases, the Si II transitions are saturated at all velocities. These kinematic signatures suggest the presence of inflowing gas, and possibly a merging companion.

### 3.4 Broad emission components in the rest-optical spectra

As discussed in Section 3.1, many recent studies have interpreted the faint, broad wings sometimes visible in nebular emission lines as evidence of outflows. However, inferences about outflow properties from broad emission are often discrepant with those from absorption line studies, in several ways:

1. Studies of broad emission in large samples of individual $z \sim 2-3$ galax-

ies (Förster Schreiber et al., 2019; Freeman et al., 2019) only detect broad emission in a small fraction of the population.

2. In high-resolution spectra and stacks, the flux ratio of broad to narrow emission varies with galaxy properties, but the FWHM of broad emission components show no trends with $M_*$, SFR, or $\Sigma_{\rm SFR}$.

3. Models of this broad emission cannot reliably distinguish between ionized gas outflows and other scenarios, such as shocks, turbulent line broadening, or AGN, and if an outflow is assumed, the inferred mass loading factor is much smaller than both theoretical expectations and inferences from absorption line studies (see, e.g. Freeman et al., 2019).

In this section we address these open questions by searching for broad emission in individual KBSS galaxies and comparing to results from the previous section, where we examined outflow signatures in the LIS absorption lines.

**Spectral Fitting to Individual Galaxies**

We searched for broad emission components in KBSS-MOSFIRE galaxies by fitting superposed broad and narrow Gaussians to the [O III]$\lambda$5008 line. Compared to H$\alpha$, [O III]$\lambda$5008 has the advantage of being unaffected by Balmer absorption or contamination from nearby spectral lines, and it is often the strongest line in the rest-optical spectra. Nevertheless, we fit only galaxies with $S/N \geq 3$ in the [O III]$\lambda$5008 line and no sky lines within 5 Å of the line center, to ensure that noise spikes were not fitted as Gaussian components. To increase the sample size, we included KBSS-MOSFIRE galaxies which met these criteria but did not have corresponding high-quality LRIS spectra, resulting in a total of 195 galaxies.

The continuum level of each individual MOSFIRE spectrum was estimated using a reddened stellar population synthesis model fit, as described by Strom et al. (2017). After subtracting the continuum level, we interpolated the flux over spectral regions that deviated strongly from the the sum of a continuum fit and a single Gaussian fit to the [O III]$\lambda$5008 line.

The free parameters in the fitting were the the Gaussian amplitudes and velocity widths of each component; we fixed the central velocity of both the narrow and broad component at zero, since in practice the emission line profiles show very little evidence of asymmetry. We applied priors intended to capture only physically plausible combinations of parameters. Apart from forcing the broad component to

have a greater velocity width and smaller amplitude than the narrow component, we required the narrow component to have a velocity width greater than the instrumental resolution of MOSFIRE, and we enforced a maximum broad velocity width of $\sigma_{\rm br}$ = 400 km/s. Other studies searching for broad emission in star-forming galaxies have found FWHM$\sim$ 125 – 250 km/s (Genzel et al., 2011; Newman et al., 2012; Wood et al., 2015), so we expect this cut to capture the majority of cases.

Fitting was performed with the Python Markov Chain Monte Carlo sampler *emcee* (Foreman-Mackey et al., 2013), with 250 walkers. The number of burn-in and run steps was determined by the autocorrelation time for each galaxy, with an average of 200 burn-in steps and 5000 run steps. Initial guesses for each parameter were determined by the best-fit single Gaussian flux and velocity width (as discussed by Strom et al. 2017).

We classified galaxies as having a detected broad component if they met several criteria. We defined the error level of each parameter estimate as the 68% highest posterior density interval (HDI), and we required all four parameters to have single-peaked posteriors within the HDI. Since the posterior distributions generally resemble Gaussian distributions, we required that the best-fit value of each parameter be greater than twice the error level defined from the HDI. Finally, we required that the peak of the broad Gaussian component must be at least twice the median noise level of the spectrum over the wavelength range of the fit.

Two examples of the MCMC fitting to individual galaxies are shown in Figure 3.8. While the two galaxies shown have very similar stellar masses, close to the median of the sample, one meets our detection criteria and the other is consistent with a single Gaussian.

In total, broad components were detected in 23 out of 195 galaxies, or 12%. Figure 3.9 shows the distribution of galaxies with detected broad components as a function of $M_*$ and $S/N([\mathrm{O\ III}])$. Galaxies are significantly more likely to have a detected broad component if $S/N([\mathrm{O\ III}])$ is high. However, the distributions of galaxies with detected broad components and those without are largely consistent with one another across the full range of $M_*$ probed by our sample. To test this, we performed Kolmogorov-Smirnov (KS) tests on the distributions of each parameter with and without detected broad components. The $M_*$ of the subsets of galaxies with and without detected broad components are consistent with the null hypothesis, i.e. that they are drawn from the same parent distribution. The distributions of $S/N([\mathrm{O\ III}])$, however, are inconsistent with the null hypothesis at the $4\sigma$ level.

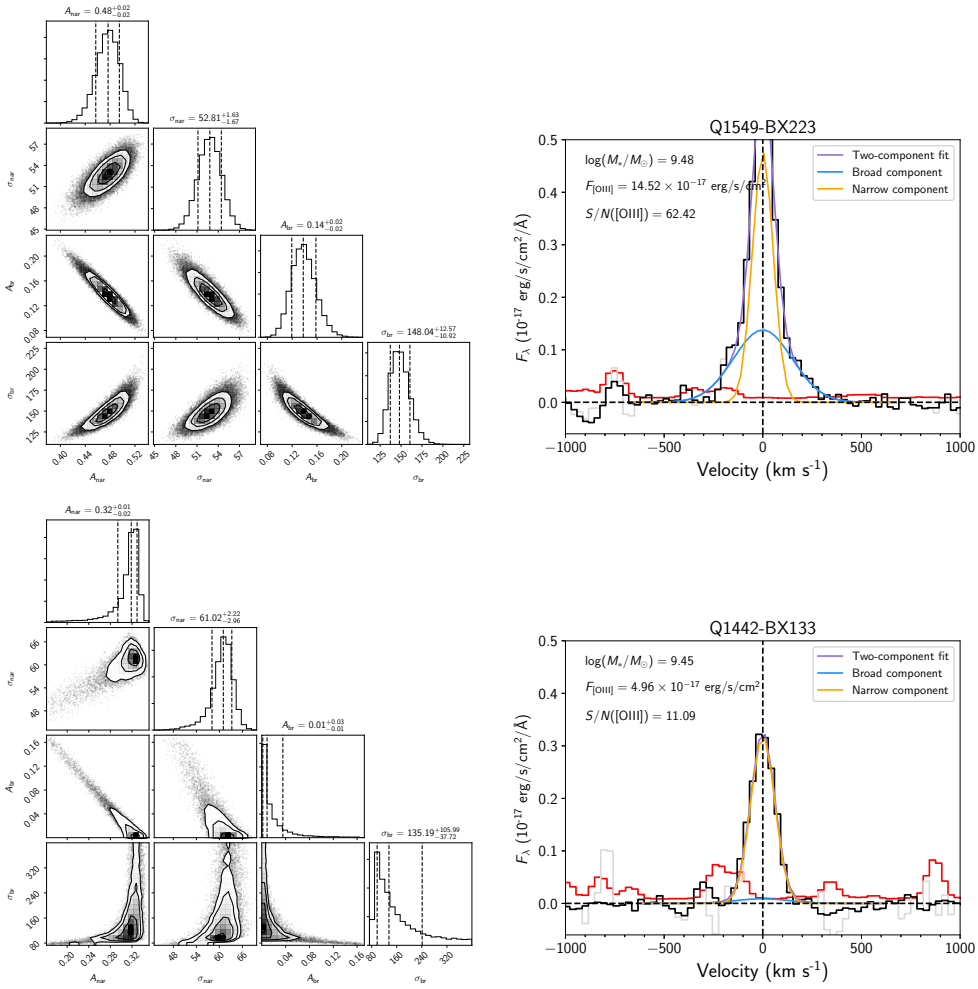


Figure 3.8: Examples of the MCMC fitting technique for broad emission components. The two galaxies shown are here have comparable stellar masses, close to the median of the sample. *Left:* corner plots for the four fit parameters, the amplitude and width of the broad and narrow components. *Right:* best-fit two-component Gaussian superposed on the observed emission line (black, where the spectrum has been interpolated over low S/N regions, shown in light gray). The 1$\sigma$ error spectrum is shown in red. The best-fit narrow component is shown in orange, the broad component in blue, and the superposition of the two in purple. The galaxy Q1549-BX223 meets the criteria we have defined for calling a broad component "detected:" $> 2\sigma$ determinations of all four parameters, where $\sigma$ is defined from the posterior distribution. Q1442-BX133, on the other hand, does not have a detected broad component.

Table 3.4: Correlations of Galaxy Properties and Detected Broad Emission Parameters.*

| Quantity | $F_{\rm br}/F_{\rm nar}$ | $\rm FWHM_{br}$ |
|---|---|---|
| $M_*$ | 2.30 | 1.10 |
| $S/N([\rm O\ III])$ | −2.73 | −1.45 |

* Quoted values are the number of sigma from the null hypothesis that the quantities are uncorrelated, from a Spearman rank order correlation test. Negative values indicate an anticorrelation.

These results are roughly consistent with those found in the literature. Förster Schreiber et al. (2019) performed a similar analysis for both AGN and star-forming galaxies at $0.6 < z < 2.7$, over a similar range of stellar masses as the KBSS sample. They found no trend between $M_*$ and broad emission incidence for the star-forming galaxies, and a positive correlation between broad emission incidence and $\Sigma_{\rm SFR}$, ranging from $\sim$ 10% to $\sim$ 30% of their sample. We detect broad components in a similar fraction of our sample (12%), and although only 52 of the 195 galaxies studied in this section have robust measurements of galaxy sizes, those with detected broad components span the entire range of $\Sigma_{\rm SFR}$ in the full sample. Similarly, Freeman et al. (2019) detected broad [O III] emission in 10% of their sample overall, and found that this fraction varied significantly with line $S/N$. They quote the 10% incidence as a lower limit on the true incidence of broad emission at $z \sim 2$; we return to this issue in the next section.

Table 3.4 presents the results of Spearman rank-order correlation tests between the properties of the detected broad emission components and $M_*$ and $S/N([\rm O\ III])$. As in the literature (Shapiro et al., 2009; Freeman et al., 2019), we find that the ratio of broad to narrow flux ($F_{\rm br}/F_{\rm nar}$) is correlated with $M_*$ at the $2\sigma$ level. However, we also find no correlation between $F_{\rm br}/F_{\rm nar}$ and SFR, and a moderate anticorrelation with $S/N([\rm O\ III])$. Since $S/N([\rm O\ III])$ decreases with stellar mass, this may be the cause of the positive correlation between $F_{\rm br}/F_{\rm nar}$ and $M_*$. The FWHM of the broad emission components, however, do not show a significant correlation with *any* quantity.

**MCMC Fitting to Synthetic Spectra**

To further investigate the dependence of broad emission properties on line $S/N$, we performed the same MCMC fitting on a set of synthetic emission-line spectra. All

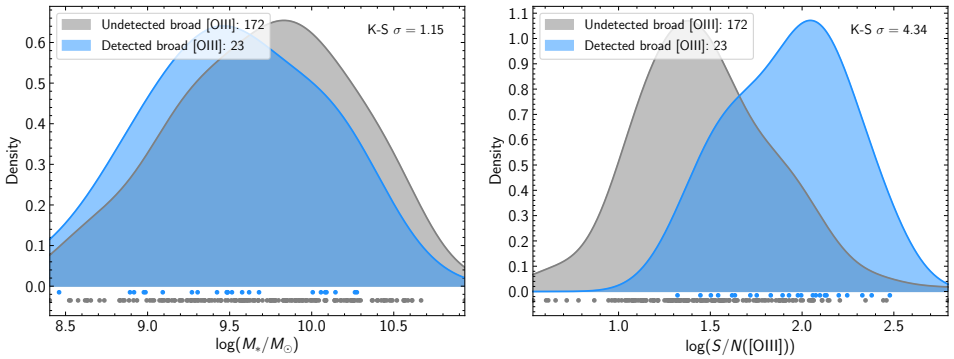


Figure 3.9: Distribution of galaxies with detected broad emission components (12% overall) as a fuction of $M_*/M_\odot$ and $S/N([\mathrm{OIII}])$. Probability distributions of galaxies with detected broad components (in blue) and those without (in gray) are represented by a Gaussian kernel density estimation. The data are displayed as points on the bottom of the plot. The probability distributions of galaxies with detected broad components and those without are largely consistent with one another across the full dynamic range of parameter space in $M_*/M_\odot$, but galaxies are much more likely to have a detected broad component if the SNR is high.

synthetic emission lines were generated from a two-component Gaussian, where the broad component is twice as wide as the narrow component in velocity space, with an amplitude 0.3 times that of the narrow component (the average of the best-fit parameters in the real spectra). Random noise was then added to each two-component Gaussian such that the $S/N$ of each line varied across approximately the same range as our galaxy sample. We generated 50 synthetic spectra at each step in $S/N$, in order to capture variations in the pixel-to-pixel noise of different spectra with the same integrated flux. The MCMC fitting was then performed in the same manner as for the real spectra.

When fitting the real spectra, we initialized the walkers in a small Gaussian "ball" around a set of initial guesses based on the best-fit single Gaussian parameters. Here, we initialized the walkers around the true amplitude and width of each synthetic Gaussian component. We also assumed a uniform error level across the line profile, with no attempt to simulate noise spikes or poor continuum subtraction. Thus, the results of this analysis can be seen as the best-case scenario, accounting only for statistical uncertainties with no systematic errors.

Figure 3.10 shows the fraction of iterations for which a broad component was detected, for each step in $S/N$. As with the real spectra, broad components are only reliably detected when the $S/N$ is high; thus, even if broad emission were

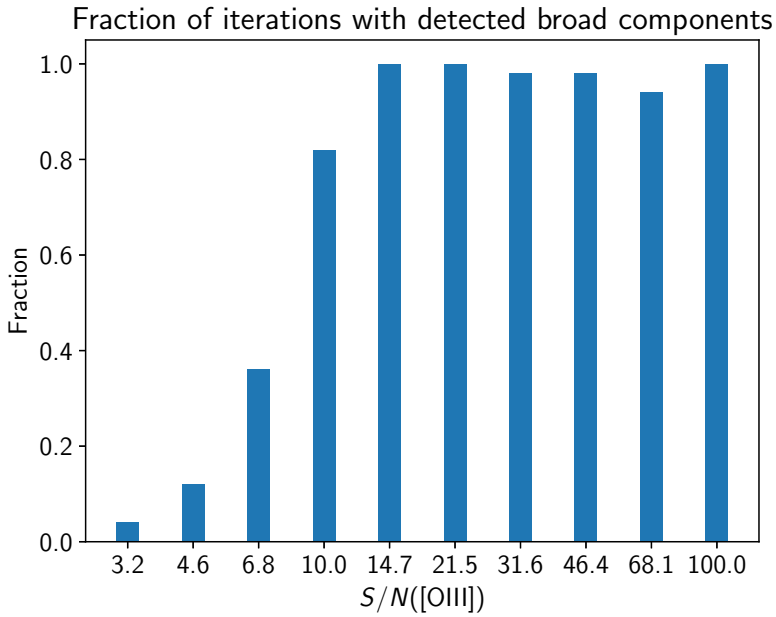


Figure 3.10: Fraction of simulated two-component Gaussians with detected broad components, as a function of $S/N$([O III]). The $S/N$ threshold above which a significant fraction of broad components are detected is $S/N \sim 10$, much higher than our galaxy sample; however, here we have not accounted for any of the systematic errors that may be present in the data.

intrinsically present in every galaxy and all sources of systematic uncertainty were accounted for, in lower-quality spectra broad components may be washed out by noise and not detected at all.

## 3.5 Discussion

### Systematics of outflow properties in absorption

As in Kornei et al. (2012), Heckman et al. (2015), and Williams et al. (2015), we find that outflow velocity correlates most strongly with $\Sigma_{\rm SFR}$. This is qualitatively consistent with the expectation for a wind driven by momentum injected from stellar feedback. In galaxies with high $\Sigma_{\rm SFR}$, the higher momentum flux is distributed over a smaller area and can heat and accelerate ambient gas more efficiently. The dependence of outflow properties on $\Sigma_{\rm SFR}$ has often been used to explain the abundance of outflows at $z \sim 2$ relative to $z \sim 0$; since galaxies at $z \sim 2$ generally have higher SFRs and more compact sizes, most galaxies have values of $\Sigma_{\rm SFR}$ exceeding the threshold proposed by Heckman (2002) for local starbursts to launch a wind: $\Sigma_{\rm SFR} \gtrsim 0.1\ M_\odot\ {\rm yr}^{-1}\ {\rm kpc}^{-2}$.

Indeed, the presence of a non-zero blueshifted component in every stacked LIS profile reinforces this picture, as the large majority galaxies in the KBSS-LM sample have values of $\Sigma_{\rm SFR}$ comparable to local starbursts. It might be expected that KBSS galaxies lying close to the SDSS locus on the N2-BPT diagram would drive weaker outflows; however, even the composites with low O32 and low BPT offset still show evidence for a significant outflowing component. Both BPT offset and O32 are sensitive to the hardness of the ionizing radiation field produced by Fe-poor massive stars (Strom et al., 2017), and thus are related to the star formation history. The specific star formation rate (sSFR $\equiv$ SFR/$M_*$) reflects the relative importance of recent star formation, and shows a relatively flat behavior at $z > 2$, but declines rapidly at $z < 2$ (Reddy et al., 2012b, and references therein).

It can be seen from Figure 3.2 that even the KBSS galaxies lying along the SDSS star-forming locus of the N2-BPT diagram still have higher [O III]/H$\beta$ and lower [N II]/H$\alpha$ ratios than the bulk of SDSS galaxies. The lack of strong correlation between outflow velocity and BPT offset may simply be due to the dynamic range probed by the KBSS dataset, which does not include many of the most massive and evolved galaxies at $z \sim 2$. Additionally, the effect of BPT offset on outflow velocity may be diluted due to the competing dependence on mass and $\Sigma_{\rm SFR}$, since those galaxies with high BPT offsets tend to be lower in mass.

Despite the range of galaxy properties probed, the LIS absorption line profiles in the stacked spectra (Figure 3.4) are remarkably similar in the depths of the absorption. In nearly every case, the two Si II lines have similar profiles at $v > 0$ but do not reach zero, suggesting optically thick gas with partial covering. However, the profiles at $v < 0$ exhibit varying degrees of optical thinness. The individual spectra in Figure 3.6 show a variety of absorption line profiles, outflow velocities, and Ly$\alpha$ profiles even for galaxies similar in $M_*$ and other properties. Detailed studies of lensed star-forming galaxies at $z \sim 2-3$ (e.g. Pettini et al., 2002; Quider et al., 2009, 2010; Berg et al., 2018; Marques-Chaves et al., 2020) have also shown that while outflows are a typical feature of galaxies in this epoch, IS absorption line profiles can vary wildly from case to case. In particular, Quider et al. (2010) found that the *stellar* features of three lensed galaxies were all indicative of young stellar populations with similar properties, despite large differences in the appearance of the interstellar features. Taken together, these results suggest that while the bulk velocity of the outflow clearly scales with $\Sigma_{\rm SFR}$, the distribution of the outflowing gas (at least in the low-ionized phase) can be quite complicated.

Furthermore, it is apparent from Table 3.3 that the relationships between the different velocity estimates are not straightforward. The centroid $v_{\rm cen}$ is determined by the combination of $W_{\rm out}$ and $W_{\rm sys,abs}$, which may or may not correlate with one another at all.

This may explain the inconsistencies among low- and intermediate-redshift studies (e.g. Heckman et al., 2000; Martin, 2005; Rupke et al., 2005; Weiner et al., 2009; Erb et al., 2012; Martin et al., 2012; Chisholm et al., 2015), that have found correlations between outflow velocity and $M_*$ and/or SFR, but are not always in agreement with one another. All in all, these results suggest that given the complexity of the outflow signatures, care must be taken in characterizing outflow velocities.

**The origin of broad optical emission**

In Section 3.4 we investigate the detectability of broad emission components using synthetic spectra, and find that the fraction of iterations with detected broad components rises sharply with $S/N$, and beyond $S/N \sim 10$, broad components are detected in nearly every case, and the true parameters of the synthetic two-component Gaussian are recovered to within a few percent. However, the right panel of Figure 3.9 shows that in the KBSS dataset, galaxies with detected broad components are only present above $S/N \sim 20$, and even then represent a small fraction of the sample. Thus, even having a high $S/N$ does not guarantee that a galaxy will have a detected broad emission component.

Several authors have compared outflow signatures in rest-UV absorption to broadened optical emission lines in local galaxies, but with mixed results. Wood et al. (2015) examined a local spiral galaxy and found that the velocity extent of the absorption lines greatly exceeds the velocity extent of the broad component of H$\alpha$, and the mass outflow rate inferred from the UV exceeds that from H$\alpha$ by nearly an order of magnitude. They conclude that the H$\alpha$ profile is likely broadened by shocks or turbulent mixing. Conversely, Hogarth et al. (2020) performed a similar analysis on a Green Pea galaxy, taken as a high-redshift analog. They fit a three-component Gaussian to the H$\alpha$ profile, and found that the broad component of H$\alpha$ spans a similar velocity extent as the UV absorption lines (including Si II$\lambda\lambda$1190, 1193, Si II$\lambda$1260, C II$\lambda$1334, and Si III$\lambda$1206). Freeman et al. (2019) find elevated [N II]/H$\alpha$ in the broad emission components of stacked $z \sim 2-3$ spectra, that are broadly consistent with shock models, although they note that other scenarios (such as the presence of undetected AGN) cannot be ruled out.

In general, measured outflow velocities are highly dependent on the gas phase being studied. Quantifying mass outflow rates is even more challenging, and studies that have estimated mass outflow rates for $z \sim 2$ galaxies using broad emission lines have reached varying conclusions (Genzel et al., 2011; Newman et al., 2012; Freeman et al., 2019). In the case of M82, the mass outflow rate inferred for the warm ionized phase is significantly smaller than both the hot wind fluid and the atomic and cold molecular phases (Heckman et al., 1990; Shopbell and Bland-Hawthorn, 1998; Contursi et al., 2013; Leroy et al., 2015). However, inferring a mass outflow rate requires knowledge of the gas mass and radial structure of the outflow, which is difficult to quantify when only a line-of-sight measurement is available.

We find that the kinematics of H$\alpha$ emission in KBSS-LM galaxies do not generally indicate the presence of outflows. If broad emission components were probing a higher ionization state of the same gas seen in absorption, we would expect the broad emission to have a greater velocity extent than the red side of the rest-UV absorption lines, since the receding side of the outflow is not seen in absorption. However, as discussed in Section 3.3, the red side of every composite LIS absorption profile meets the continuum at the same velocity as the corresponding nebular emission lines. While broad emission components are only seen in a small fraction of individual galaxies, stacking should increase the $S/N$ such that broad emission components due to outflows should be visible if present. The similarity between the velocity extent of the emission and absorption lines suggests that both sets of lines are tracing the same ISM gas, at $\langle v \rangle = 0 \pm \sigma_{\rm abs}$. The narrower core and broader tail of the H$\alpha$ line profile relative to the LIS absorption is consistent with the expectation that the nebular emission lines probe the denser regions of the same gas.

Complications may be introduced when stacking galaxy spectra, since averaging multiple Gaussians inherently results in a line profile that is more "tailed" than a Gaussian. It may be the case that broad wings may be artificially introduced into both the emission and absorption lines by the use of composite spectra; however, the individual galaxies in the KBSS-LM sample with the highest continuum $S/N$ display the same trend (Figure 3.6). Given these uncertainties and the many other possible explanations for broadened H$\alpha$ emission, caution must be exercised when interpreting broadened nebular line emission as evidence of galactic outflows.

## 3.6 Summary and conclusions

We have presented a detailed analysis of outflow signatures in the rest-UV and rest-optical spectra of $z \sim 2-3$ star-forming galaxies from KBSS-MOSFIRE. We generated composite rest-UV spectra grouped by five galaxy properties ($M_*$, $M_{\rm dyn}$, $\Sigma_{\rm SFR}$, BPT offset, and O32), and measured outflow velocities from low-ionization UV absorption lines using several different metrics. We also searched for broad [O III] emission components in the rest-optical spectra of individual galaxies, and examined the systematic uncertainties involved in this analysis using synthetic spectra. We have shown the following:

1. The centroid velocity of the LIS absorption line profiles ($v_{\rm cen}$) is strongly affected by the presence of interstellar gas at $\langle v \rangle = 0$, superposed on the blueshifted component originating in outflowing gas. Since these two absorption components have different dependences on galaxy properties such as $M_*$, the maximum velocity on the blueshifted side of the absorption profile ($v_{\rm max}$) remains a more reliable velocity measure. However, $v_{\rm max}$ is affected by the placement of the continuum level as well as the specific transition chosen (in the case where the gas is optically thin at high velocities). Thus, comparing different velocity measures (as well as those from different transitions) provides a useful "sanity check."

2. The only parameter that shows a clear monotonic relationship with outflow kinematics is $\Sigma_{\rm SFR}$, in line with results from low- and intermediate-redshift starbursts. This result is consistent with the expectation for momentum-driven winds, and supports a common explanation for the ubiquity of large-scale outflows at $z \sim 2-3$—since galaxies at these redshifts are generally more compact with higher SFRs, nearly *every* galaxy has a high enough $\Sigma_{\rm SFR}$ to launch a wind.

3. In both individual and composite spectra, the velocity extents of H$\alpha$ and the LIS absorption lines are nearly identical at $v > 0$. This shows that the kinematics of emission are indistinguishable from that of the ambient ISM of the galaxy, since we do not expect to see absorption from the receding side of the outflow.

Given these results, and the strong $S/N$ dependence of broad nebular emission, we conclude that rest-UV absorption lines are more likely to indicate the presence of outflows than emission.

*Chapter 4*

# STELLAR POPULATION SYNTHESIS MODELS

Portions of this chapter appear in Theios et al. (2019) and Theios et al. (2020).

## 4.1 Introduction

Bulk galaxy properties such as stellar mass, star formation rate (SFR), star formation history (SFH), and stellar population age are often inferred from spectral energy distribution (SED) fits to broadband photometry using stellar population synthesis models such as those of Bruzual and Charlot (2003) and "Binary Populations and Spectral Synthesis" (BPASS; Eldridge et al., 2017; Stanway and Eldridge, 2018). These same models can be fitted to rest-UV galaxy spectra, or input as the ionizing radiation source in photoionization models (e.g. Cloudy; Ferland et al., 2013), which predict the observed nebular line ratios as a function of the ionization parameter $U$ and the gas-phase metallicity $Z_{\rm neb}$.

Together, these analyses can be used to glean valuable information about the underlying stellar populations, and much recent work has thus focused on comparing results assuming different stellar models. In particular, Steidel et al. (2016) tested these models by leveraging information from rest-UV and rest-optical spectra of a pilot sample of 30 galaxies known as KBSS-LM1. They found that the only models that can simultaneously reproduce the observed level of nebular excitation and the strength of the stellar features in the FUV are those including binary evolution, with low stellar metallicities ($Z_*$) and moderate gas-phase oxygen abundances ($Z_{\rm neb}$). This requires an O/Fe enhancement consistent with the expectation that chemical enrichment in these galaxies is dominated by core-collapse supernova (CCSN) ejecta, as a result of these galaxies' short and rising star formation histories (e.g. Reddy et al., 2012b).

Thus, binary SED models with low stellar metallicities are most likely to reproduce the observed physical conditions in high-redshift galaxies. However, there remain significant uncertainties in their treatment of stellar atmospheres and binary evolution. SED fitting to galaxy photometry also requires assumptions about the galaxy's star formation history, dust attenuation curve, and IMF, all of which are poorly constrained at high redshift. Fitting these same models to the rest-UV spectra

presents additional challenges—in particular, continuum placement and matching the spectral resolution of the models to the data. In this chapter we explore the systematics of these two techniques using the KBSS sample.

## 4.2 SED fitting

Stellar masses, SFRs (hereafter $\mathrm{SFR_{SED}}$), and continuum color excesses (hereafter $E(B-V)_{\mathrm{SED}}$) were estimated for KBSS-MOSFIRE galaxies based on SED fits to broadband photometry in the optical ($U_nG\mathcal{R}$), near-IR ($J, H, K_s$, and WFC3-IR F140W and F160W), and mid-IR (*Spitzer*-Infrared Array Camera 3.6$\mu$mand 4.5$\mu$m). Prior to the SED fitting, the near-IR photometry was corrected for the emission line contribution from H$\alpha$ and [O III]. Details of the photometric data and sample selection are described elsewhere (e.g. Steidel et al., 2004; Reddy et al., 2012b; Steidel et al., 2014).

### Fitting procedure

The fiducial model used in our SED fitting is a reddened BPASSv2.2 (Stanway and Eldridge, 2018) model with a stellar metallicity of $Z_* = 0.002$ ($Z_*/Z_\odot \approx 0.14$) and binary evolution included. The model we used has a Kroupa-type IMF, with a slope of $-2.35$ for masses $> 1M_\odot$ and an upper mass cutoff of $100M_\odot$.[1]

The default models provided by BPASS reflect a single burst of star formation over a range of ages. We summed these models to generate templates assuming a constant star formation history, with stellar population ages in the range $10^{7.0} - 10^{9.7}$ yr, in steps of $\log(t/\mathrm{yr}) = 0.1$. In practice, however, we enforced a minimum allowed age of 50 Myr; as discussed by Reddy et al. (2012b), this is approximately the central dynamical timescale and is imposed to prevent best-fit solutions with unrealistically young ages.

The model SED at each age was redshifted using its measured nebular redshift $z_{\mathrm{neb}}$, reddened from $E(B-V) = 0 - 0.6$ with either the Calzetti et al. (2000) or SMC attenuation curve, and attenuated blueward of rest-frame 1216 Å by intergalactic medium (IGM) opacity using Monte Carlo modeling. The best-fit normalization of the model at a given age and reddening step was determined by minimizing $\chi^2$ with respect to the observed photometry, and this normalization determined the SFR and stellar mass. The best-fit combination of age and reddening was then taken to be that which minimizes the overall $\chi^2$.

[1] While galaxies at these redshifts would likely have a rising SFH in reality, we expect the results assuming constant SFHs to be similar (Reddy et al., 2012b).

Table 4.1: Parameters Relative to BPASSv2.2 $Z_* = 0.002$

| Quantity | BPASSv2.1 $Z_* = 0.002$ | BC03 $Z_* = 0.004$ | BC03 $Z_\odot$ |
|---|---|---|---|
| $E(B-V)_{\rm SED}$ | −0.02 | 0.00 | −0.07 |
| Age | 0.00 | +0.23 | +0.65 |
| $M_*$ | −0.04 | +0.17 | +0.33 |
| $\rm SFR_{SED}$ | −0.04 | +0.10 | −0.12 |

All quoted values are the mean difference in dex between the parameters output by the given model and those output by the fiducial model used in this paper, BPASSv2.2 $Z_* = 0.002$ $M_{\rm up} = 100 M_\odot$. Stellar masses and SFRs have been adjusted to account for the differences in IMF between the BPASS and Bruzual and Charlot (2003) models.

The default BPASSv2.2 models do not include the contribution from the nebular continuum emission. As in Steidel et al. (2016, their Figure 3), we calculated this contribution relative to the stellar continuum by using the photoionization models that produced the best matches to the observed nebular spectra. This contribution was then added to the BPASSv2.2 models before fitting them to the data. The effect of including the nebular continuum is to make the total continuum slightly redder than the stellar continuum only, thus requiring slightly lower values of $E(B-V)_{\rm SED}$ to match the data, by 5% on average.

**Fit parameters and characteristic uncertainties**

We estimated a characteristic uncertainty on the SED fit parameters by perturbing each photometric point for each galaxy in the sample 100 times within $1\sigma$, and fitting SEDs to each perturbation using each attenuation curve. We found that the average 68% confidence intervals for each parameter were: $\pm 0.016$ dex for $E(B-V)_{\rm SED}$, $[-0.07, +0.09]$ dex for $\log(t/{\rm yr})$, $[-0.07, +0.06]$ dex for $\log(\rm SFR_{SED}$, and $\pm 0.04$ dex for $\log(M_*)$. We found that 46% of the galaxies in the sample were equally well fit by both Calzetti et al. (2000) and SMC within the uncertainty, which we define as the average 68% confidence interval on $\chi^2$ for the 100 iterations of the bootstrap.

The top panel of Figure 4.1 shows example SED fits for one such galaxy, Q2343-BX215 (left; $z_{\rm neb} = 2.17$). Both curves gave similar values of $\chi^2$ in this case, and while the inferred stellar masses are similar for both curves, SMC predicts an older age and lower SFR. The bottom panel of Figure 4.1 shows example SED fits for the galaxy Q0105-BX48. For this galaxy, SMC gave a significantly lower $\chi^2$.

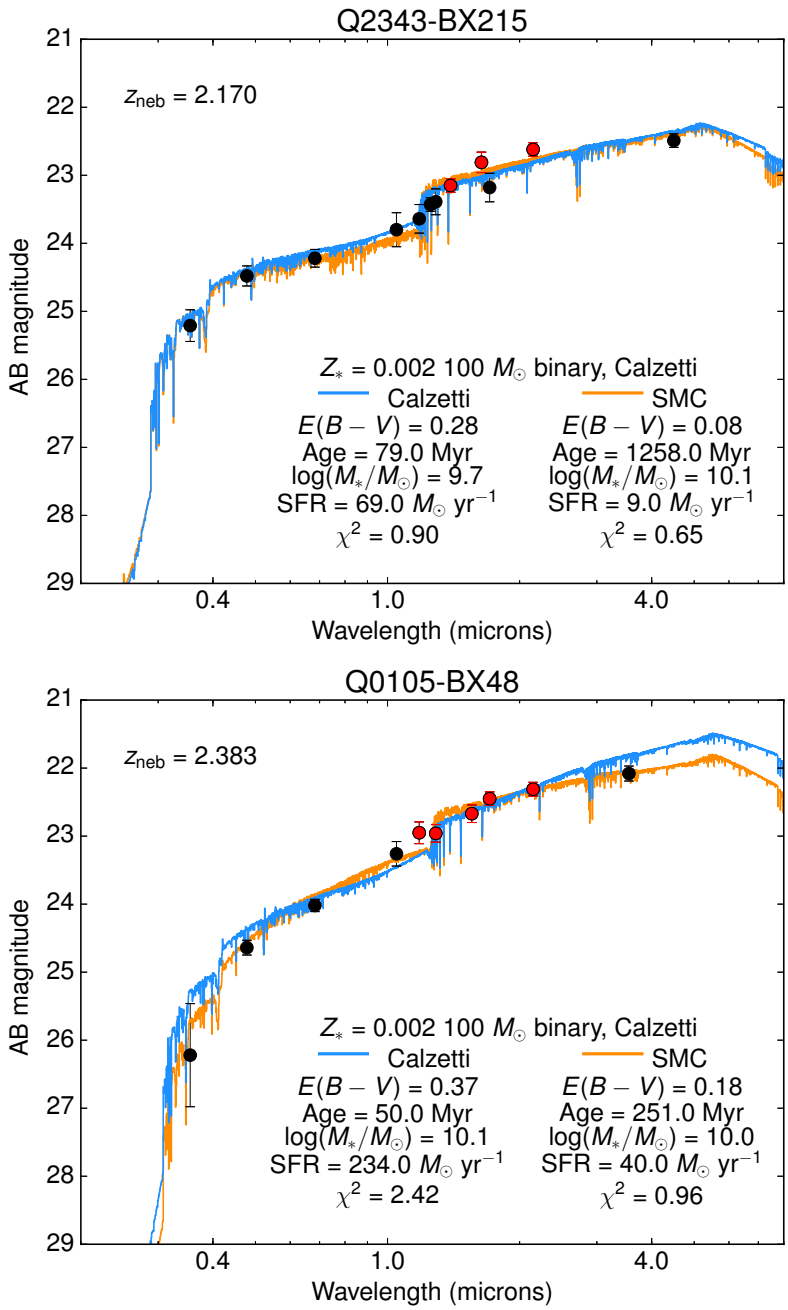


Figure 4.1: Example SEDs for the galaxies Q2343-BX215 (top; $z_{\rm neb}$ = 2.170) and Q0105-BX48 (bottom; $z_{\rm neb}$ = 2.383). Photometric points are shown in black, and red points are those that have been corrected for the emission line contribution. BPASSv2.2 SEDs are shown for the Calzetti et al. (2000) (blue) and SMC (orange) attenuation curves. In the case of Q2343-BX215, both curves give an equally good fit, and while the inferred stellar masses are similar, SMC predicts an older age, lower $E(B-V)_{\rm SED}$, and lower SFR. For Q0105-BX48, however, SMC provides a much better fit.

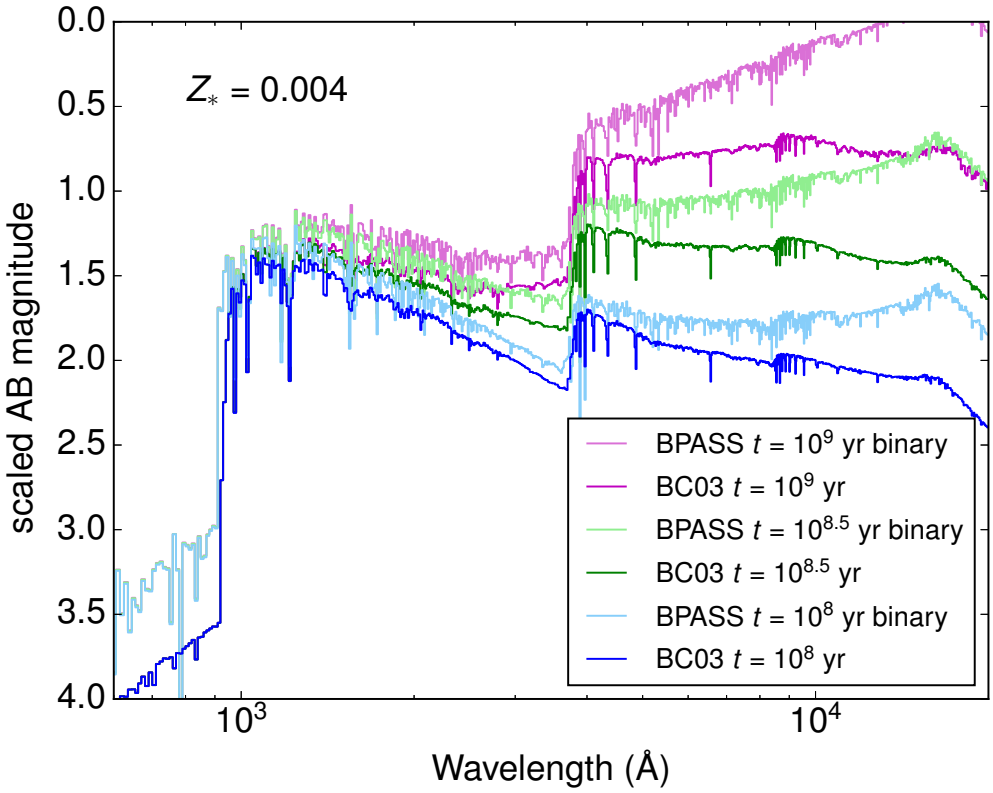


Figure 4.2: Comparison of BPASSv2.2 and Bruzual and Charlot (2003) model SEDs, where both models assume a metallicity of $Z_* = 0.004$. The SEDs are unreddened and unredshifted, and the BPASSv2.2 models shown here assume an upper mass cutoff of $100 M_\odot$ with nebular continuum not included. The SEDs are compared at three different ages: $t = 10^8$ yr, $t = 10^{8.5}$ yr, and $t = 10^9$ yr. The BPASSv2.2 models are somewhat brighter than Bruzual and Charlot (2003) in the far-UV, the region most important for determining $\mathrm{SFR_{SED}}$. This generally results in lower SFRs given by the BPASSv2.2 models.

**Comparison to other SPS models**

For comparison with our fiducial model, we fit SEDs using the older BPASSv2.1 $Z_* = 0.002$ binary models with an upper mass cutoff of $100 M_\odot$, including nebular continuum. We also fit SEDs using the Bruzual and Charlot (2003) $Z_* = 0.004$ and $Z_* = 0.020$ models (the latter of which is arguably the most commonly used SED model in the literature). We find that the $\chi^2$ of the fits using both of these models were similar to those produced by our fiducial model. A detailed comparison between the four models used for SED fitting is beyond the scope of this work; however, the fractional changes in each fit parameter relative to their BPASSv2.2 $100 M_\odot$ binary model values are given in Table 4.1 (all assuming Calzetti et al. 2000 attenuation).

Note that the Bruzual and Charlot (2003) models do not include the contribution from the nebular continuum.

We also fit SEDs using the BPASS models with an upper mass cutoff of $300M_{\odot}$, and found that changing the upper mass cutoff has almost no effect on any of the inferred parameters due to the relative insensitivity of the integrated SED in the range $0.35 - 4.5\mu$m (or $\sim$1200Å$-1.5\mu$m in the rest frame) to the most massive stars; the primary difference between the two models is in the (unobservable) EUV spectrum, and thus, the predicted strengths of nebular emission lines and line ratios. We selected the $100M_{\odot}$ model as our fiducual model because the derivation of the Calzetti et al. (2000) curve assumes an upper mass IMF cutoff of $100M_{\odot}$. Table 4.1 compares the inferred SED fit parameters for the three models discussed in this paper.

Figure 4.2 compares the model SEDs for BPASSv2.2 and Bruzual and Charlot (2003) for three choices of stellar population age, where both models assume a metallicity of $Z_{*} = 0.004$, and nebular continuum is not included for the BPASSv2.2 models. The BPASSv2.2 models are somewhat brighter than Bruzual and Charlot (2003) blueward of the Balmer break at $t = 10^{8}$ yr, which is close to the median age predicted by the Bruzual and Charlot (2003) $Z_{*} = 0.020$ models.

### 4.3 Fitting to rest-UV spectra

Pettini et al. (2002) performed the first detailed analysis of the chemical abundance patterns in a Lyman Break Galaxy (LBG), from observations of the gravitationally lensed galaxy MS 1512-cB58. However, such detailed information is not available for the majority of LBGs. To address this problem, Rix et al. (2004) developed a technique for abundance determinations based on rest-frame UV stellar spectra. They used the WM-basic and Starburst99 codes to generate model spectra, and investigated the sensitivity of the spectrum to stellar metallicities ranging from $Z_{*} = 0.05Z_{\odot}$ to $2Z_{\odot}$. They found three blends of photospheric lines from OB stars that were particularly sensitive to metallicity, and concluded that the blend centered on 1978 Å was most suitable for stellar abundance determinations. Since then, many studies have made use of this so-called "1978 index."

There is substantial room for improvement in this field with the development of novel stellar population synthesis codes, in particular those such as BPASS that incorporate the effects of binary evolution. Steidel et al. (2016) examined the details of the rest-UV spectrum of the LM1 stack, and found other regions also sensitive to

stellar metallicity, such as 1560 – 1590 Å and 1770 – 1850 Å. They concluded that a $\chi^2$ minimization of the BPASS models relative to the stack made optimal use of all available spectral information, and they determined that the stack was best-fit by models in the metallicity range $Z_* = 0.001 - 0.002$.

Steidel et al. (2016) fixed the stellar population age of the assumed models at a realistic value of $t = 10^8$ years; more recently, studies such as Topping et al. (2019) have attempted to fit for $Z_*$ and stellar population age simultaneously. This presents several challenges—broad and shallow features such as the 1978 index are sensitive to continuum placement, which may be subject to variations due to flux calibration errors. Additional uncertainties may be introduced if the spectral resolution of the model does not match that of the data.

In this section, we compare results from two spectral synthesis fitting techniques, similar to those used by Steidel et al. (2016) and Topping et al. (2019), in order to understand the effect of systematic uncertainties on inferred galaxy properties.

**Model details**

We used the far-UV spectra generated by the BPASSv2.2 model suite (Stanway and Eldridge, 2018). We considered only models with an upper mass cut-off of $100 M_\odot$ which include binary evolution, with stellar metallicities $Z_* = (0.0001, 0.001, 0.002, 0.003, 0.004, 0.006, 0.008, 0.010, 0.014)$. As in the SED fitting, we self-consistently included the nebular continuum contribution.

We allow the stellar metallicity of the models to vary independently of any knowledge of the gas-phase O/H in the galaxy sample; because $Z_*$ in the model spectra maps to Fe/H in the stars, decoupling $Z_*$ from O/H in the gas allows us to accout for non-solar abundance ratios of O relative to Fe (see also Strom et al., 2018).

**Spectral fitting procedure**

First, the model spectra can be fit directly to the data varying only the degree of stellar continuum reddening. In Theios et al. (2019), we fit the same BPASS models to several composite rest-UV spectra assuming two different dust attenuation curves: the Calzetti et al. (2000) starburst curve and a modified version of the SMC curve from Gordon et al. (2003). We found that although the inferred $E(B-V)$ was strongly affected by the choice of attenuation curve, the best-fit stellar metallicity was consistently $Z_* = 0.001 - 0.002$ regardless of any other assumptions. However, in that paper we only fit BPASS models assuming a continuous star formation history

with an age of $10^8$ years; here we repeat this analysis over a range of ages.

However, as discussed in Theios et al. (2019), the true attenuation curve for $z \sim 2-3$ galaxies remains uncertain, and likely varies from galaxy to galaxy. Furthermore, variations in the spectral shape due to flux calibration errors may degrade the fit to the most metallicity-sensitive spectral features. Thus, the second approach is to marginalize over these factors by modulating the shape of the model spectrum to match the broader continuum level of the observed spectrum (e.g. Topping et al., 2019). While this method does not allow for determination of the continuum $E(B-V)$, it may provide more accurate constraints on $Z_*$ and the stellar population age.

To this effect, we fit a cubic spline to the ratio of the observed spectrum to model spectrum, with nodes set in the spectral regions determined by Steidel et al. (2016) to correspond to continuum points with little contamination from spectral features. Within these regions, nodes were set $\sim$ 100 Å apart so that the resulting spline function interpolates over both the metallicity-sensitive features being fitted and noise in the observed spectrum. Outlier pixels were rejected from this cubic spline function using an iterative sigma clipping algorithm, until convergence was reached. The result is a smooth function capturing only the broad shape of the continuum.

To perform the fitting, we iterated over a grid of $Z_*$ and age, normalizing each model using the iterative spline fitting technique discussed above. The best-fit model was then determined by calculating the total $\chi^2$ for each fit, summed over all unmasked pixels. In all cases, the observed spectrum was corrected for the average transmission of the IGM blueward of the Ly$\alpha$ line, as discussed in Steidel et al. (2018).

**Results**

The upper panel of Figure 4.3 compares these two fitting methods for a stack of all 121 KBSS-LM spectra discussed in Section 3.2. The lower panel of Figure 4.3 shows $\Delta\sigma$ from the minimum $\chi^2/\nu$ for each combination of $Z_*$ and $\log(t/\mathrm{yr})$ in the grid. Median SED-fit ages for different combinations of SED model and attenuation curve are shown as colored lines.

As in Steidel et al. (2016), models with $Z_* \geq 0.003$ are strongly dis-favored relative to the lower-metallicity models. The nominal best-fit age for this stack is $\log(t/\mathrm{yr}) = 9.2$, significantly older than the majority of ages inferred from SED fitting for the individual galaxies in this sample, likely due to the fact that we have not included Ly$\alpha$ absorption from the ISM in the models (see Steidel et al., 2018, for details).

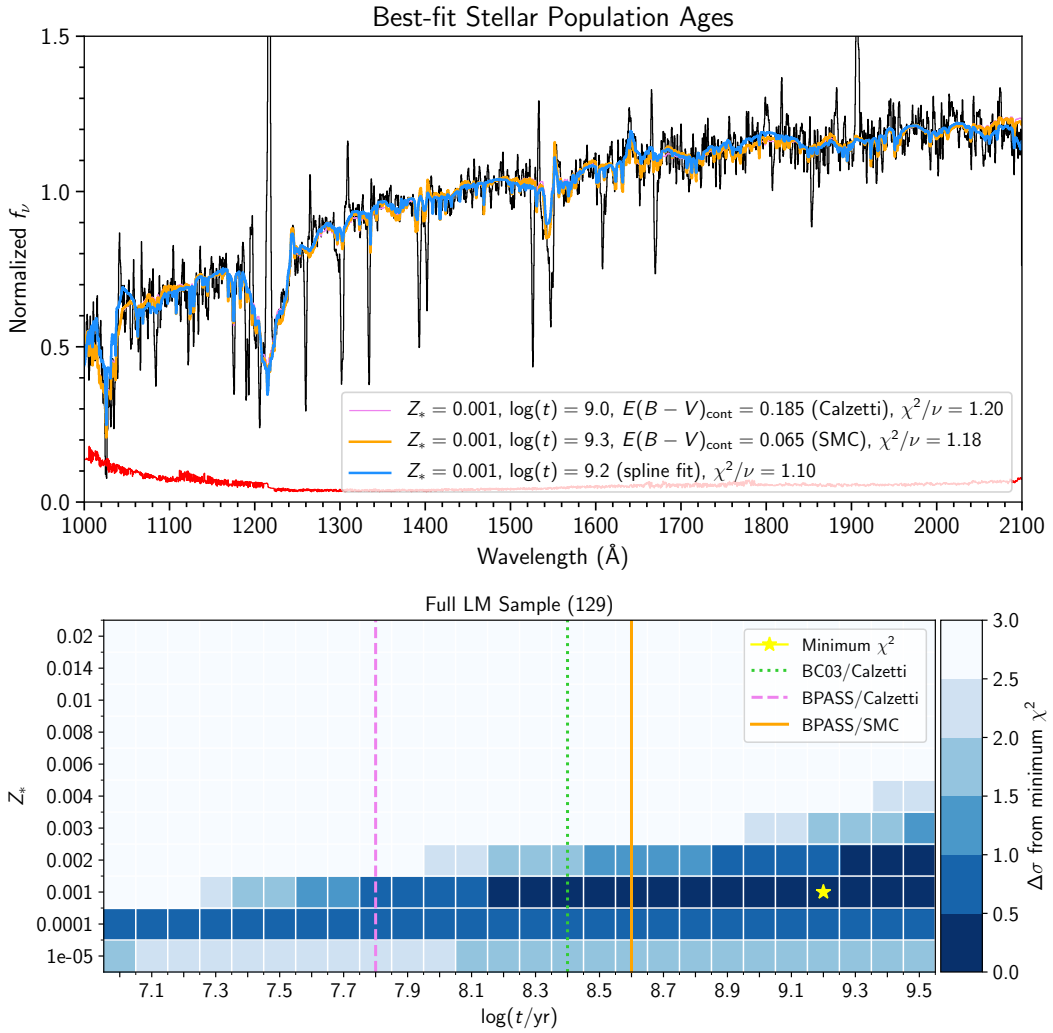


Figure 4.3: *Top:* Composite rest-frame UV spectrum of the full KBSS-LM sample (see Section 3.2). Superposed are BPASSv2.2 model spectra fit to the data using the two methods discussed above. In violet and orange are the best-fit reddened model templates assuming the Calzetti et al. (2000) and SMC attenuation curves. Shown in green is the best-fit model spectrum where the model shape has been modulated by a cubic spline fit to the data. In all cases, the models shown correspond to the best-fit combination of stellar popluation age and metallicity. *Bottom:* For each combination of $Z_*$ and log($t$/yr) in the grid of models, the color represents $\Delta\sigma$ from the minimum $\chi^2/\nu$, where the nominal best fit is indicated by a yellow star. The vertical lines mark the median SED-fit ages assuming various combinations of SED model and attenuation curve.

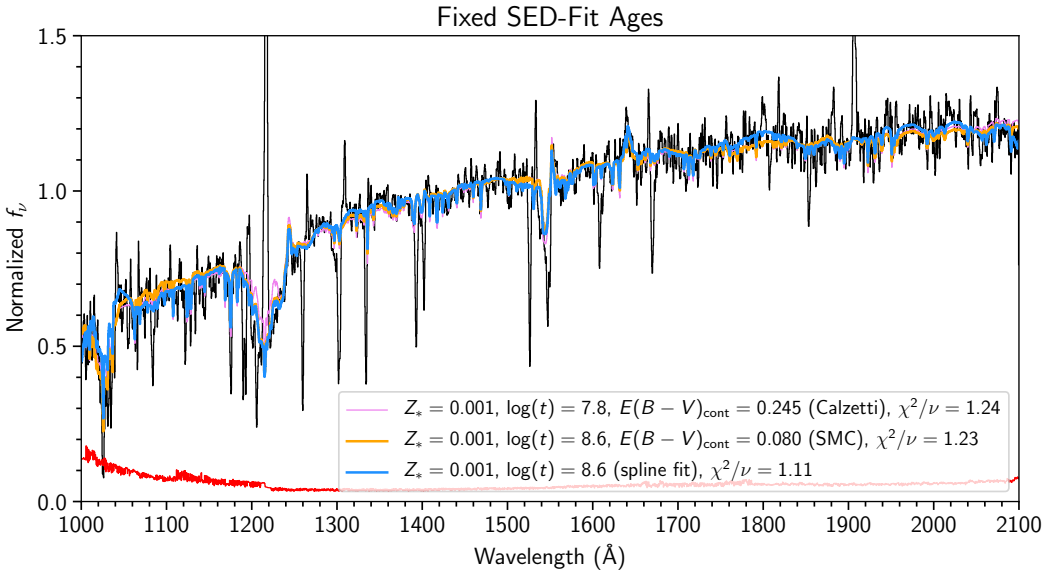


Figure 4.4: Same as the top panel of Figure 4.3, but with the age fixed to the median SED fit age of each galaxy contributing to the stack (which depends on the assumed attenuation curve).

However, the age is largely unconstrained by the rest-UV spectra. In the lower panel of Figure 4.3, every model with $Z_* = 0.0001$ gives the same $\chi^2/\nu$ to within $1\sigma$, and at the best-fit metallicity of $Z_* = 0.001$, only the youngest ages in the grid can be confidently ruled out.

When the spectral shape is fixed and only the reddening is allowed to vary, the results are similar—the best-fit metallicity is $Z_* = 0.001$ assuming both Calzetti et al. (2000) and SMC attenuation, and the inferred ages are much larger than would be expected from the results of the SED fitting. Overall, these two assumed attenuation curves provide very similar fits ($\Delta\chi^2/\nu < 1\sigma$); $E(B-V)$ is larger when the Calzetti et al. (2000) curve is assumed, due to the shallower slope of the attenuation curve in the rest-UV (see Section 2.3).

Figure 4.4 shows the same set of spectra where, instead of allowing the stellar population age to vary, it is fixed to the median SED fit age of each galaxy contributing to the stack (which depends on the assumed attenuation curve). The results are remarkably similar—in fact, the only significant difference between the fits shown in Figure 4.3 and Figure 4.4 is that $E(B-V)$ is larger in the latter case.

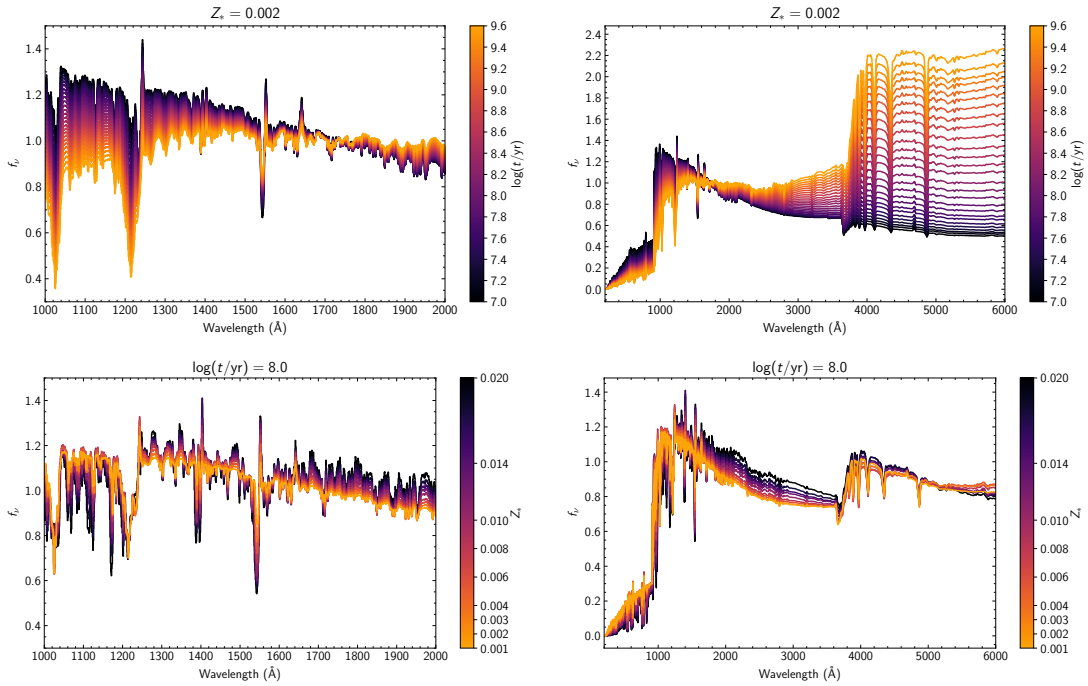


Figure 4.5: Comparison of BPASS models as a function of age and $Z_*$. The top two panels show BPASS models for different ages at fixed $Z_*$, and the bottom two are different metallicities at fixed age. The left two panels zoom in on the FUV portion of the spectra and the right two panels show a larger range of the full SED. In all cases, the spectra are unreddened and unredshifted. The stellar population age primarily determines the overall slope of the spectrum with relatively little effect on spectral features (with the exception of the stellar wind lines).

## 4.4 Discussion and conclusions

As discussed in Theios et al. (2019), reddening and age are naturally degenerate with one another, at least in the rest-UV portion of the spectrum. This effect is further demonstrated in Figure 4.5. Each of the available BPASS models are plotted against each other, where the top two panels show a range of ages at fixed $Z_*$ and the bottom two show a range of $Z_*$ at fixed age. The left two panels zoom in on the FUV portion of the spectrum, and the right two panels show a wider swath of the SED. As the stellar population age increases, the spectra become redder, but most of the detailed spectral features remain relatively constant. The strength of the stellar wind features (including the P-Cygni C IV profile) do decrease with increasing age; however, these features appear to be equally sensitive to the metallicity. The bottom two panels demonstrate that in general, the detailed shape of the FUV spectrum is much more sensitive to the stellar metallicity, while the overall "slope" of the spectrum remains relatively constant.

The fact that age is poorly constrained by both fitting methods can be explained by the following argument: if most of the information about the stellar population age contained in the rest-UV spectrum comes from the overall "slope" rather than the detailed spectral shape, this information would be lost when both the observed and model spectra are continuum-normalized prior to fitting. On the other hand, when the continuum shape is preserved and the models are instead reddened to match the observed spectra, the degeneracy between reddening and age causes the fit to prefer unphysically old models with little dust reddening.

All in all, these results suggest that estimates of stellar population age from far-UV spectra should be used with caution, since spectral synthesis models such as BPASS are relatively insensitive to age in this wavelength regime. The righthand panels of Figure 4.5 show that the Balmer break is much more sensitive to age, and so SED fitting may be used to break the degeneracy between reddening and age. We found in Section 4.2 that in the SED fitting, both age and $E(B-V)$ had characteristic uncertainties of $< 0.1$ dex. Both of these parameters are subject to *systematic* uncertainties relating to the assumptions of SED model and attenuation curve—the BPASS models predict younger ages than Bruzual and Charlot (2003), and the SMC curve predicts older ages than Calzetti et al. (2000). Still, once a model has been assumed, SED fitting is a useful tool for comparing stellar population ages across the galaxy population.

*Chapter 5*

# SUMMARY AND CONCLUSIONS

The work presented in this thesis illustrates some of the fundamental differences between galaxies at the peak of galaxy assembly ($2 \lesssim z \lesssim 3$) and those we observe in the local Universe. In Chapter 2 I showed that compared to local galaxies, high-redshift galaxies have lower O/H (and/or higher nebular excitation) at fixed nebular reddening, and higher nebular reddening at fixed stellar mass, suggesting that while high-redshift galaxies have lower dust/gas ratios on average, their overall gas fractions are much higher, in line with previous observations (e.g. Erb et al., 2006a).

Chapter 3 confirms that large-scale galactic winds are a common occurrence at high-redshift, over a wide range in parameters such as stellar mass and nebular emission-line ratios. In fact, even those galaxies with emission-line ratios closest to those of low redshift star-forming galaxies still show evidence for outflows in their rest-UV absorption lines. The spectra of individual galaxies show a great variety in terms of optical depth, absorption line strength, and Ly$\alpha$ profiles. However, the maximum velocity extent of the UV absorption lines (at $v < 0$) is a relatively robust measure of outflow velocity, as it is not affected by the strength of the absorption component originating in ambient interstellar gas. On the other hand, the maximum velocity extent of the UV absorption lines at $v > 0$ is remarkably similar to that of H$\alpha$ in nearly every case, suggesting that the high-velocity wings of rest-optical emission lines are not useful tracers of outflowing gas.

The outflow velocity (as measured from low-ionization UV absorption lines) is most strongly correlated with star formation surface density, as has been found in several studies at lower redshifts. This result supports a common explanation for the ubiquity of galactic winds at high redshift: due to their higher SFRs and more compact sizes, nearly *every* galaxy at $z \sim 2-3$ has a high enough star formation surface density to launch a wind.

## 5.1 You must unlearn what you have learned

This thesis highlights the importance of developing appropriate calibrations for galaxy properties at high redshift that reflect their inherent differences. Steidel et al.

(2014), Steidel et al. (2016), and Strom et al. (2017, 2018) showed that galaxies at $z \sim 2-3$ exhibit enhanced O/Fe and harder ionizing radiation fields than their low-redshift counterparts, a natural consequence of differences in their star formation histories. Thus, several common assumptions do not apply—in particular, strong-line metallicity diagnostics such as O3N2, as well as the applicability of spectral synthesis models with solar abundance patterns that do not account for the effects of massive binary evolution.

In Chapter 2, I expanded upon this work and showed that SFRs inferred from both H$\alpha$ and SED fitting are strongly dependent on the assumed properties of the underlying massive stellar populations, as well as the IMF and dust attenuation curve. Harder ionizing radiation fields produce a higher H$\alpha$ luminosity at a given SFR, and the low-metallicity, binary BPASS models most appropriate at high redshift predict SFRs that are lower by a factor of $\sim$ 0.35 relative to the Kennicutt and Evans (2012) calibration that is commonly used at low redshift. When the most appropriate models are input into SED fitting, the SMC attenuation curve produces the best agreement between SED-based and H$\alpha$-based SFRs, rather than the more commonly used Calzetti et al. (2000) "starburst" curve.

In Chapter 4, I showed that the results of SED fitting are strongly dependent on several assumptions, including metallicity, binarity, attenuation curve, and star formation history. However, changing these assumptions generally results in a systematic offset in the inferred parameters rather than a change in rank-ordering, and thus are still useful for comparing galaxies across a population. Chapter 4 also demonstrates that while fitting these same models to rest-UV spectra is a powerful tool for characterizing the underlying massive stellar populations, the stellar populaton age is largely degenerate with reddening in this region of the spectrum.

## 5.2 Always in motion is the future

The work presented in this thesis highlights several future avenues of research. Given the many degeneracies involved in measuring physical parameters from stellar population synthesis models, leveraging multiple sources of information is a promising route forward. In this thesis, I have characterized some of the systematic uncertainties involved in fitting SPS models to rest-UV spectra as well as full SEDs. The next step is to perform these two techniques simultaneously with photoionization modeling of the nebular spectra of the same galaxies, and knowledge of the pitfalls of each step will help to streamline this process.

Chapter 3 shows that while outflow velocities in high-redshift star-forming galaxies clearly scale with the star formation surface density, the structure and geometrical distribution of outflowing gas varies from galaxy to galaxy. While this information is difficult to extract from line-of-sight observations, integral field unit (IFU) spectrographs such as the Keck Cosmic Web Imager (KCWI) are well-suited to obtain spatial as well as spectral information about galactic winds, as well as providing complementary information about the structure of the CGM into which these outflows propagate.

Finally, the current KBSS sample is somewhat biased against the most evolved galaxies at $z \sim 2-3$, i.e. those with declining star formation histories. The chemical abundance patterns of these galaxies are likely very different, and may contain a mixture of nucleosynthetic products from CCSNe and Type Ia SNe. Chapter 3 suggests that even those galaxies closest to the $z \sim 0$ star-forming locus of the N2-BPT diagram still host large-scale outflows; however, since the most evolved $z \sim 2-3$ galaxies are not represented in the subsample studied here, we are likely not seeing the full picture. Expanding the dynamic range of star formation histories probed by the KBSS dataset will help shed light on the evolution of galaxies over cosmic time.

# BIBLIOGRAPHY


Abazajian, K. N. et al. (June 2009). "The Seventh Data Release of the Sloan Digital Sky Survey". In: *ApJS* 182, 543-558, pp. 543–558. DOI: 10.1088/0067-0049/182/2/543. arXiv: 0812.0649.

Adelberger, K. L. and C. C. Steidel (Nov. 2000). "Multiwavelength Observations of Dusty Star Formation at Low and High Redshift". In: *ApJ* 544, pp. 218–241. DOI: 10.1086/317183. eprint: astro-ph/0001126.

Adelberger, Kurt L. et al. (May 2004). "Optical Selection of Star-forming Galaxies at Redshifts $1 \leq z \leq 3$". In: *ApJ* 607.1, pp. 226–240. DOI: 10.1086/383221. arXiv: astro-ph/0401445 [astro-ph].

Álvarez-Márquez, J. et al. (Mar. 2016). "Dust properties of Lyman-break galaxies at $z \sim 3$". In: *A&A* 587, A122, A122. DOI: 10.1051/0004-6361/201527190. arXiv: 1512.04120.

Armus, L. et al. (June 1995). "ROSAT Observations of NGC 2146: Evidence for a Starburst-driven Superwind". In: *ApJ* 445, p. 666. DOI: 10.1086/175729.

Asplund, M. et al. (Sept. 2009). "The Chemical Composition of the Sun". In: *ARA&A* 47, pp. 481–522. DOI: 10.1146/annurev.astro.46.060407.145222. arXiv: 0909.0948 [astro-ph.SR].

Baldwin, J. A., M. M. Phillips, and R. Terlevich (Feb. 1981). "Classification parameters for the emission-line spectra of extragalactic objects." In: *PASP* 93, pp. 5–19. DOI: 10.1086/130766.

Benson, A. J. et al. (Dec. 2003). "What Shapes the Luminosity Function of Galaxies?" In: *ApJ* 599.1, pp. 38–49. DOI: 10.1086/379160. arXiv: astro-ph/0302450 [astro-ph].

Berg, Danielle A. et al. (June 2018). "A Window on the Earliest Star Formation: Extreme Photoionization Conditions of a High-ionization, Low-metallicity Lensed Galaxy at z 2*". In: *ApJ* 859.2, 164, p. 164. DOI: 10.3847/1538-4357/aab7fa. arXiv: 1803.02340 [astro-ph.GA].

Bouwens, R. J. et al. (Dec. 2016). "ALMA Spectroscopic Survey in the Hubble Ultra Deep Field: The Infrared Excess of UV-Selected z = 2-10 Galaxies as a Function of UV-Continuum Slope and Stellar Mass". In: *ApJ* 833, 72, p. 72. DOI: 10.3847/1538-4357/833/1/72. arXiv: 1606.05280.

Bruzual, G. and S. Charlot (Oct. 2003). "Stellar population synthesis at the resolution of 2003". In: *MNRAS* 344, pp. 1000–1028. DOI: 10.1046/j.1365-8711.2003.06897.x. eprint: astro-ph/0309134.

Buat, V. et al. (Sept. 2011). "GOODS-Herschel: evidence of a UV extinction bump in galaxies at $z > 1$". In: *A&A* 533, A93, A93. DOI: 10.1051/0004-6361/201117264. arXiv: 1107.1049 [astro-ph.CO].

Calzetti, D., A. L. Kinney, and T. Storchi-Bergmann (July 1994). "Dust extinction of the stellar continua in starburst galaxies: The ultraviolet and optical extinction law". In: *ApJ* 429, pp. 582–601. DOI: 10.1086/174346.

Calzetti, D. et al. (Apr. 2000). "The Dust Content and Opacity of Actively Star-forming Galaxies". In: *ApJ* 533, pp. 682–695. DOI: 10.1086/308692. eprint: astro-ph/9911459.

Capak, P. L. et al. (June 2015). "Galaxies at redshifts 5 to 6 with systematically low dust content and high [C II] emission". In: *Nature* 522, pp. 455–458. DOI: 10.1038/nature14500. arXiv: 1503.07596.

Cardelli, J. A., G. C. Clayton, and J. S. Mathis (Oct. 1989). "The relationship between infrared, optical, and ultraviolet extinction". In: *ApJ* 345, pp. 245–256. DOI: 10.1086/167900.

Chabrier, Gilles (July 2003). "Galactic Stellar and Substellar Initial Mass Function". In: *PASP* 115.809, pp. 763–795. DOI: 10.1086/376392. arXiv: astro-ph/0304382 [astro-ph].

Charlot, S. and S. M. Fall (Aug. 2000). "A Simple Model for the Absorption of Starlight by Dust in Galaxies". In: *ApJ* 539, pp. 718–731. DOI: 10.1086/309250. eprint: astro-ph/0003128.

Chisholm, J., C. Tremonti, and C. Leitherer (Dec. 2018). "Metal-enriched galactic outflows shape the mass-metallicity relationship". In: *MNRAS* 481.2, pp. 1690–1706. DOI: 10.1093/mnras/sty2380. arXiv: 1808.10453 [astro-ph.GA].

Chisholm, J. et al. (Sept. 2019). "Constraining the Metallicities, Ages, Star Formation Histories, and Ionizing Continua of Extragalactic Massive Star Populations". In: *ApJ* 882.2, 182, p. 182. DOI: 10.3847/1538-4357/ab3104. arXiv: 1905.04314 [astro-ph.GA].

Chisholm, John et al. (Oct. 2015). "Scaling Relations Between Warm Galactic Outflows and Their Host Galaxies". In: *ApJ* 811.2, 149, p. 149. DOI: 10.1088/0004-637X/811/2/149. arXiv: 1412.2139 [astro-ph.GA].

Contursi, A. et al. (Jan. 2013). "Spectroscopic FIR mapping of the disk and galactic wind of M 82 with Herschel-PACS". In: *A&A* 549, A118, A118. DOI: 10.1051/0004-6361/201219214. arXiv: 1210.3496 [astro-ph.GA].

Crowther, P. A. (Sept. 2007). "Physical Properties of Wolf-Rayet Stars". In: *ARA&A* 45, pp. 177–219. DOI: 10.1146/annurev.astro.45.051806.110615. eprint: astro-ph/0610356.

Daddi, E. et al. (Nov. 2007). "Multiwavelength Study of Massive Galaxies at z~2. I. Star Formation and Galaxy Growth". In: *ApJ* 670, pp. 156–172. DOI: 10.1086/521818. arXiv: 0705.2831.

Daddi, E. et al. (Jan. 2008). "Vigorous Star Formation with Low Efficiency in Massive Disk Galaxies at z = 1.5". In: *ApJL* 673, L21, p. L21. DOI: 10.1086/527377. arXiv: 0711.4995.

Dekel, A. and J. Silk (Apr. 1986). "The Origin of Dwarf Galaxies, Cold Dark Matter, and Biased Galaxy Formation". In: *ApJ* 303, p. 39. DOI: 10.1086/164050.

Dominguez, A. et al. (Feb. 2013). "Dust Extinction from Balmer Decrements of Star-forming Galaxies at $0.75 \leq z \leq 1.5$ with Hubble Space Telescope/Wide-Field-Camera 3 Spectroscopy from the WFC3 Infrared Spectroscopic Parallel Survey". In: *ApJ* 763.2, 145, p. 145. DOI: 10.1088/0004-637X/763/2/145. arXiv: 1206.1867 [astro-ph.CO].

Eldridge, J. J. et al. (Nov. 2017). "Binary Population and Spectral Synthesis Version 2.1: Construction, Observational Verification, and New Results". In: *PASA* 34, e058, e058. DOI: 10.1017/pasa.2017.51. arXiv: 1710.02154 [astro-ph.SR].

Eldridge, John J. and Elizabeth R. Stanway (Jan. 2012). "The effect of stellar evolution uncertainties on the rest-frame ultraviolet stellar lines of C IV and He II in high-redshift Lyman-break galaxies". In: *MNRAS* 419.1, pp. 479–489. DOI: 10.1111/j.1365-2966.2011.19713.x. arXiv: 1109.0288 [astro-ph.CO].

Erb, D. K. et al. (July 2006a). "The Stellar, Gas, and Dynamical Masses of Star-forming Galaxies at $z \sim 2$". In: *ApJ* 646, pp. 107–132. DOI: 10.1086/504891. eprint: astro-ph/0604041.

Erb, Dawn K., Charles C. Steidel, and Yuguang Chen (July 2018). "The Kinematics of Extended Ly$\alpha$ Emission in a Low-mass, Low-metallicity Galaxy at $z = 2.3$". In: *ApJL* 862.1, L10, p. L10. DOI: 10.3847/2041-8213/aacff6. arXiv: 1807.00065 [astro-ph.GA].

Erb, Dawn K. et al. (Aug. 2006b). "H$\alpha$ Observations of a Large Sample of Galaxies at $z \sim 2$: Implications for Star Formation in High-Redshift Galaxies". In: *ApJ* 647.1, pp. 128–139. DOI: 10.1086/505341. arXiv: astro-ph/0604388 [astro-ph].

Erb, Dawn K. et al. (June 2006c). "The Mass-Metallicity Relation at z>~2". In: *ApJ* 644.2, pp. 813–828. DOI: 10.1086/503623. arXiv: astro-ph/0602473 [astro-ph].

Erb, Dawn K. et al. (Aug. 2010). "Physical Conditions in a Young, Unreddened, Low-metallicity Galaxy at High Redshift". In: *ApJ* 719.2, pp. 1168–1190. DOI: 10.1088/0004-637X/719/2/1168. arXiv: 1006.5456 [astro-ph.CO].

Erb, Dawn K. et al. (Nov. 2012). "Galactic Outflows in Absorption and Emission: Near-ultraviolet Spectroscopy of Galaxies at $1 < z < 2$". In: *ApJ* 759.1, 26, p. 26. DOI: 10.1088/0004-637X/759/1/26. arXiv: 1209.4903 [astro-ph.CO].

Esteban, C. et al. (Sept. 2014). "Carbon and oxygen abundances from recombination lines in low-metallicity star-forming galaxies. Implications for chemical evolution". In: *MNRAS* 443, pp. 624–647. DOI: 10.1093/mnras/stu1177. arXiv: 1406.3986.

Ferland, G. J. et al. (Apr. 2013). "The 2013 Release of Cloudy". In: *RevMexAA* 49, pp. 137–163. arXiv: 1302.4485 [astro-ph.GA].

Foreman-Mackey, Daniel et al. (Mar. 2013). "emcee: The MCMC Hammer". In: *PASP* 125.925, p. 306. DOI: 10.1086/670067. arXiv: 1202.3665 [astro-ph.IM].

Förster Schreiber, N. M. et al. (Apr. 2019). "The KMOS$^{3D}$ Survey: Demographics and Properties of Galactic Outflows at z = 0.6-2.7". In: *ApJ* 875.1, 21.

Freeman, William R. et al. (Mar. 2019). "The MOSDEF Survey: Broad Emission Lines at z = 1.4-3.8". In: *ApJ* 873.2, 102, p. 102. DOI: 10.3847/1538-4357/ab0655.

Genzel, R. et al. (June 2011). "The Sins Survey of z ~2 Galaxy Kinematics: Properties of the Giant Star-forming Clumps". In: *ApJ* 733.2, 101, p. 101. DOI: 10.1088/0004-637X/733/2/101. arXiv: 1011.5360 [astro-ph.CO].

Gordon, K. D. et al. (Sept. 2003). "A Quantitative Comparison of the Small Magellanic Cloud, Large Magellanic Cloud, and Milky Way Ultraviolet to Near-Infrared Extinction Curves". In: *ApJ* 594, pp. 279–293. DOI: 10.1086/376774. eprint: astro-ph/0305257.

Granato, G. L. et al. (Oct. 2000). "The Infrared Side of Galaxy Formation. I. The Local Universe in the Semianalytical Framework". In: *ApJ* 542, pp. 710–730. DOI: 10.1086/317032. eprint: astro-ph/0001308.

Heckman, T. M. (2002). "Galactic Superwinds Circa 2001". In: *Extragalactic Gas at Low Redshift*. Ed. by John S. Mulchaey and John T. Stocke. Vol. 254. Astronomical Society of the Pacific Conference Series, p. 292.

Heckman, T. M. et al. (Aug. 2000). "Absorption-Line Probes of Gas and Dust in Galactic Superwinds". In: *ApJS* 129, pp. 493–516. DOI: 10.1086/313421. eprint: astro-ph/0002526.

Heckman, Timothy M., Lee Armus, and George K. Miley (Dec. 1990). "On the Nature and Implications of Starburst-driven Galactic Superwinds". In: *ApJS* 74, p. 833. DOI: 10.1086/191522.

Heckman, Timothy M. and Todd A. Thompson (Jan. 2017). "Galactic Winds and the Role Played by Massive Stars". In: *arXiv e-prints*, arXiv:1701.09062, arXiv:1701.09062. arXiv: 1701.09062 [astro-ph.GA].

Heckman, Timothy M. et al. (Aug. 2015). "The Systematic Properties of the Warm Phase of Starburst-Driven Galactic Winds". In: *ApJ* 809.2, 147, p. 147. DOI: 10.1088/0004-637X/809/2/147. arXiv: 1507.05622 [astro-ph.GA].

Heinis, S. et al. (Jan. 2014). "HerMES: dust attenuation and star formation activity in ultraviolet-selected samples from z~ 4 to ~ 1.5". In: *MNRAS* 437.2, pp. 1268–1283. DOI: 10.1093/mnras/stt1960. arXiv: 1310.3227 [astro-ph.CO].

Hogarth, L. et al. (Apr. 2020). "Chemodynamics of green pea galaxies - I. Outflows and turbulence driving the escape of ionizing photons and chemical enrichment". In: *MNRAS* 494.3, pp. 3541–3561. DOI: 10.1093/mnras/staa851. arXiv: 2003.07187 [astro-ph.GA].

Kashino, D. et al. (Nov. 2013). "The FMOS-COSMOS Survey of Star-forming Galaxies at z ∼ 1.6. I. H$\alpha$-based Star Formation Rates and Dust Extinction". In: *ApJL* 777.1, L8, p. L8. DOI: 10.1088/2041-8205/777/1/L8. arXiv: 1309.4774 [astro-ph.CO].

Kauffmann, Guinevere (July 2014). "Quantitative constraints on starburst cycles in galaxies with stellar masses in the range $10^8 - 10^{10} M_\odot$ ". In: *MNRAS* 441.3, pp. 2717–2724. DOI: 10.1093/mnras/stu752.

Kauffmann, Guinevere et al. (Dec. 2003). "The host galaxies of active galactic nuclei". In: *MNRAS* 346.4, pp. 1055–1077. DOI: 10.1111/j.1365-2966.2003.07154.x. arXiv: astro-ph/0304239 [astro-ph].

Kennicutt Jr., R. C. (May 1998). "The Global Schmidt Law in Star-forming Galaxies". In: *ApJ* 498, pp. 541–552. DOI: 10.1086/305588. eprint: astro-ph/9712213.

Kennicutt, Robert C. and Neal J. Evans (Sept. 2012). "Star Formation in the Milky Way and Nearby Galaxies". In: *ARA&A* 50, pp. 531–608. DOI: 10.1146/annurev-astro-081811-125610. arXiv: 1204.3552 [astro-ph.GA].

Kewley, L. J. and M. A. Dopita (Sept. 2002). "Using Strong Lines to Estimate Abundances in Extragalactic H II Regions and Starburst Galaxies". In: *ApJS* 142.1, pp. 35–52. DOI: 10.1086/341326. arXiv: astro-ph/0206495 [astro-ph].

Kewley, L. J. et al. (July 2001). "Theoretical Modeling of Starburst Galaxies". In: *ApJ* 556.1, pp. 121–140. DOI: 10.1086/321545. arXiv: astro-ph/0106324 [astro-ph].

Koprowski, M. P. et al. (Sept. 2016). "A Resolved Map of the Infrared Excess in a Lyman Break Galaxy at z = 3". In: *ApJL* 828, L21, p. L21. DOI: 10.3847/2041-8205/828/2/L21. arXiv: 1608.05080.

Koprowski, M. P. et al. (Oct. 2018). "A direct calibration of thtae IRX-$\beta$ relation in Lyman-break Galaxies at z = 3-5". In: *MNRAS* 479.4, pp. 4355–4366. DOI: 10.1093/mnras/sty1527. arXiv: 1801.00791 [astro-ph.GA].

Kornei, Katherine A. et al. (Oct. 2012). "The Properties and Prevalence of Galactic Outflows at z ∼1 in the Extended Groth Strip". In: *ApJ* 758.2, 135, p. 135. DOI: 10.1088/0004-637X/758/2/135. arXiv: 1205.0812 [astro-ph.CO].

Kriek, M. and C. Conroy (Sept. 2013). "The Dust Attenuation Law in Distant Galaxies: Evidence for Variation with Spectral Type". In: *ApJL* 775, L16, p. L16. DOI: 10.1088/2041-8205/775/1/L16. arXiv: 1308.1099.

Kriek, Mariska et al. (June 2015). "The MOSFIRE Deep Evolution Field (MOSDEF) Survey: Rest-frame Optical Spectroscopy for ∼1500 H-selected Galaxies at 1.37 < z < 3.8". In: *ApJS* 218.2, 15, p. 15. DOI: 10.1088/0067-0049/218/2/15. arXiv: 1412.1835 [astro-ph.GA].

Law, David R. et al. (Jan. 2012). "An HST/WFC3-IR Morphological Survey of Galaxies at z = 1.5-3.6. I. Survey Description and Morphological Properties of Star-forming Galaxies". In: *ApJ* 745.1, 85, p. 85. DOI: 10.1088/0004-637X/745/1/85. arXiv: 1107.3137 [astro-ph.CO].

Lehnert, Matthew D., Timothy M. Heckman, and Kimberly A. Weaver (Oct. 1999). "Very Extended X-Ray and H$\alpha$ Emission in M82: Implications for the Superwind Phenomenon". In: *ApJ* 523.2, pp. 575–584. DOI: 10.1086/307762. arXiv: astro-ph/9904227 [astro-ph].

Leitherer, C. and T. M. Heckman (Jan. 1995). "Synthetic properties of starburst galaxies". In: *ApJS* 96, pp. 9–38. DOI: 10.1086/192112.

Leitherer, C. et al. (May 2014). "The Effects of Stellar Rotation. II. A Comprehensive Set of Starburst99 Models". In: *ApJS* 212, 14, p. 14. DOI: 10.1088/0067-0049/212/1/14. arXiv: 1403.5444.

Leitherer, Claus et al. (Apr. 2001). "Ultraviolet Line Spectra of Metal-poor Star-forming Galaxies". In: *ApJ* 550.2, pp. 724–736. DOI: 10.1086/319814. arXiv: astro-ph/0012358 [astro-ph].

Leroy, Adam K. et al. (Dec. 2015). "The Multi-phase Cold Fountain in M82 Revealed by a Wide, Sensitive Map of the Molecular Interstellar Medium". In: *ApJ* 814.2, 83, p. 83. DOI: 10.1088/0004-637X/814/2/83. arXiv: 1509.02932 [astro-ph.GA].

Madau, Piero and Mark Dickinson (Aug. 2014). "Cosmic Star-Formation History". In: *ARA&A* 52, pp. 415–486. DOI: 10.1146/annurev-astro-081811-125615. arXiv: 1403.0007 [astro-ph.CO].

Mannucci, F. et al. (Nov. 2010). "A fundamental relation between mass, star formation rate and metallicity in local and high-redshift galaxies". In: *MNRAS* 408, pp. 2115–2127. DOI: 10.1111/j.1365-2966.2010.17291.x. arXiv: 1005.0006.

Marques-Chaves, R. et al. (Feb. 2020). "Rest-frame UV properties of luminous strong gravitationally lensed Ly$\alpha$ emitters from the BELLS GALLERY Survey". In: *MNRAS* 492.1, pp. 1257–1278. DOI: 10.1093/mnras/stz3500. arXiv: 1912.04033 [astro-ph.GA].

Martin, Crystal L. (Mar. 2005). "Mapping Large-Scale Gaseous Outflows in Ultraluminous Galaxies with Keck II ESI Spectra: Variations in Outflow Velocity with Galactic Mass". In: *ApJ* 621.1, pp. 227–245. DOI: 10.1086/427277. arXiv: astro-ph/0410247 [astro-ph].

Martin, Crystal L. et al. (Dec. 2012). "Demographics and Physical Properties of Gas Outflows/Inflows at 0.4 < z < 1.4". In: *ApJ* 760.2, 127, p. 127. DOI: 10.1088/0004-637X/760/2/127. arXiv: 1206.5552 [astro-ph.CO].

Masters, Daniel, Andreas Faisst, and Peter Capak (Sept. 2016). "A Tight Relation between N/O Ratio and Galaxy Stellar Mass Can Explain the Evolution of Strong Emission Line Ratios with Redshift". In: *ApJ* 828.1, 18, p. 18. DOI: 10.3847/0004-637X/828/1/18. arXiv: 1605.04314 [astro-ph.GA].

Masters, Daniel et al. (Apr. 2014). "Physical Properties of Emission-line Galaxies at z ∼2 from Near-infrared Spectroscopy with Magellan FIRE". In: *ApJ* 785.2, 153, p. 153. DOI: 10.1088/0004-637X/785/2/153. arXiv: 1402.0510 [astro-ph.GA].

McLean, I. S. et al. (Sept. 2012). "MOSFIRE, the multi-object spectrometer for infra-red exploration at the Keck Observatory". In: *Ground-based and Airborne Instrumentation for Astronomy IV*. Vol. 8446. Proc. SPIE, 84460J. DOI: 10.1117/12.924794.

McLure, R. J. et al. (May 2018). "Dust attenuation in 2 < z < 3 star-forming galaxies from deep ALMA observations of the Hubble Ultra Deep Field". In: *MNRAS* 476.3, pp. 3991–4006. DOI: 10.1093/mnras/sty522. arXiv: 1709.06102 [astro-ph.GA].

Meurer, Gerhardt R., Timothy M. Heckman, and Daniela Calzetti (Aug. 1999). "Dust Absorption and the Ultraviolet Luminosity Density at z ∼ 3 as Calibrated by Local Starburst Galaxies". In: *ApJ* 521.1, pp. 64–80. DOI: 10.1086/307523. arXiv: astro-ph/9903054 [astro-ph].

Nanayakkara, Themiya et al. (Apr. 2019). "Exploring He II $\lambda$1640 emission line properties at z 2-4". In: *A&A* 624, A89, A89. DOI: 10.1051/0004-6361/201834565. arXiv: 1902.05960 [astro-ph.GA].

Narayanan, Desika et al. (Feb. 2018). "The IRX-$\beta$ dust attenuation relation in cosmological galaxy formation simulations". In: *MNRAS* 474.2, pp. 1718–1736. DOI: 10.1093/mnras/stx2860. arXiv: 1705.05858 [astro-ph.GA].

Nelson, Erica June et al. (Jan. 2016). "Spatially Resolved Dust Maps from Balmer Decrements in Galaxies at z ∼ 1.4". In: *ApJL* 817.1, L9, p. L9. DOI: 10.3847/2041-8205/817/1/L9. arXiv: 1511.04443 [astro-ph.GA].

Newman, Sarah F. et al. (Dec. 2012). "The SINS/zC-SINF Survey of z ∼2 Galaxy Kinematics: Outflow Properties". In: *ApJ* 761.1, 43, p. 43. DOI: 10.1088/0004-637X/761/1/43. arXiv: 1207.5897 [astro-ph.CO].

Nomoto, K. et al. (Oct. 2006). "Nucleosynthesis yields of core-collapse supernovae and hypernovae, and galactic chemical evolution". In: *Nuclear Physics A* 777, pp. 424–458. DOI: 10.1016/j.nuclphysa.2006.05.008. eprint: astro-ph/0605725.

Oke, J. B. et al. (Apr. 1995). "The Keck Low-Resolution Imaging Spectrometer". In: *PASP* 107, p. 375. DOI: 10.1086/133562.

Osterbrock, D. E. (1989). *Astrophysics of gaseous nebulae and active galactic nuclei*.

Oteo, I. et al. (Apr. 2014). "The ultraviolet to far-infrared spectral energy distribution of star-forming galaxies in the redshift desert". In: *MNRAS* 439, pp. 1337–1363. DOI: 10.1093/mnras/stt2468. arXiv: 1307.0971.

Pettini, M. and B. E. J. Pagel (Mar. 2004). "[OIII]/[NII] as an abundance indicator at high redshift". In: *MNRAS* 348, pp. L59–L63. DOI: 10.1111/j.1365-2966.2004.07591.x. eprint: astro-ph/0401128.

Pettini, M. et al. (Apr. 2002). "New Observations of the Interstellar Medium in the Lyman Break Galaxy MS 1512-cB58". In: *ApJ* 569, pp. 742–757. DOI: 10.1086/339355. eprint: astro-ph/0110637.

Pettini, Max et al. (Sept. 2003). "The C IV Mass Density of the Universe at Redshift 5". In: *ApJ* 594.2, pp. 695–703. DOI: 10.1086/377043. arXiv: astro-ph/0305413 [astro-ph].

Pilyugin, L. S., E. K. Grebel, and L. Mattsson (Aug. 2012). "'Counterpart' method for abundance determinations in H II regions". In: *MNRAS* 424, pp. 2316–2329. DOI: 10.1111/j.1365-2966.2012.21398.x. arXiv: 1205.5716.

Popping, Gergö, Annagrazia Puglisi, and Colin A. Norman (Dec. 2017). "Dissecting the IRX-$\beta$ dust attenuation relation: exploring the physical origin of observed variations in galaxies". In: *MNRAS* 472.2, pp. 2315–2333. DOI: 10.1093/mnras/stx2202. arXiv: 1706.06587 [astro-ph.GA].

Price, Sedona H. et al. (June 2014). "Direct Measurements of Dust Attenuation in z $\sim$ 1.5 Star-forming Galaxies from 3D-HST: Implications for Dust Geometry and Star Formation Rates". In: *ApJ* 788.1, 86, p. 86. DOI: 10.1088/0004-637X/788/1/86. arXiv: 1310.4177 [astro-ph.CO].

Prochaska, J. Xavier, Daniel Kasen, and Kate Rubin (June 2011). "Simple Models of Metal-line Absorption and Emission from Cool Gas Outflows". In: *ApJ* 734.1, 24, p. 24. DOI: 10.1088/0004-637X/734/1/24. arXiv: 1102.3444 [astro-ph.GA].

Quider, Anna M. et al. (Sept. 2009). "The ultraviolet spectrum of the gravitationally lensed galaxy 'the Cosmic Horseshoe': a close-up of a star-forming galaxy at z $\sim$2". In: *MNRAS* 398.3, pp. 1263–1278. DOI: 10.1111/j.1365-2966.2009.15234.x. arXiv: 0906.2412 [astro-ph.CO].

Quider, Anna M. et al. (Mar. 2010). "A study of interstellar gas and stars in the gravitationally lensed galaxy 'the Cosmic Eye' from rest-frame ultraviolet spectroscopy". In: *MNRAS* 402.3, pp. 1467–1479. DOI: 10.1111/j.1365-2966.2009.16005.x. arXiv: 0910.0840 [astro-ph.CO].

Reddy, N. A. et al. (Sept. 2016a). "Spectroscopic Measurements of the Far-Ultraviolet Dust Attenuation Curve at z $\sim$ 3". In: *ApJ* 828, 107, p. 107. DOI: 10.3847/0004-637X/828/2/107. arXiv: 1606.00434.

Reddy, N. A. et al. (Sept. 2016b). "The Connection Between Reddening, Gas Covering Fraction, and the Escape of Ionizing Radiation at High Redshift". In: *ApJ* 828, 108, p. 108. DOI: 10.3847/0004-637X/828/2/108. arXiv: 1606.03452.

Reddy, N. A. et al. (May 2017). "The HDUV Survey: A Revised Assessment of the Relationship between UV Slope and Dust Attenuation for High-Redshift Galaxies". In: *ArXiv e-prints*. arXiv: 1705.09302.

Reddy, N. et al. (Jan. 2012a). "GOODS-Herschel Measurements of the Dust Attenuation of Typical Star-forming Galaxies at High Redshift: Observations of Ultraviolet-selected Galaxies at z $\sim$ 2". In: *ApJ* 744.2, 154, p. 154. DOI: 10.1088/0004-637X/744/2/154. arXiv: 1107.2653 [astro-ph.CO].

Reddy, Naveen A. and Charles C. Steidel (Mar. 2004). "X-Ray and Radio Emission from Ultraviolet-selected Star-forming Galaxies at Redshifts 1.5$\lesssim$z$\lesssim$3.0 in the GOODS-North Field". In: *ApJL* 603.1, pp. L13–L16. DOI: 10.1086/383087. arXiv: astro-ph/0401432 [astro-ph].

Reddy, Naveen A. et al. (June 2006). "Star Formation and Extinction in Redshift z$\sim$2 Galaxies: Inferences from Spitzer MIPS Observations". In: *ApJ* 644.2, pp. 792–812. DOI: 10.1086/503739. arXiv: astro-ph/0602596 [astro-ph].

Reddy, Naveen A. et al. (Apr. 2010). "Dust Obscuration and Metallicity at High Redshift: New Inferences from UV, H$\alpha$, and 8 $\mu$m Observations of z $\sim$ 2 Star-forming Galaxies". In: *ApJ* 712.2, pp. 1070–1091. DOI: 10.1088/0004-637X/712/2/1070. arXiv: 1002.0837 [astro-ph.CO].

Reddy, Naveen A. et al. (July 2012b). "The Characteristic Star Formation Histories of Galaxies at Redshifts z $\sim$ 2-7". In: *ApJ* 754.1, 25, p. 25. DOI: 10.1088/0004-637X/754/1/25. arXiv: 1205.0555 [astro-ph.CO].

Reddy, Naveen A. et al. (June 2015). "The MOSDEF Survey: Measurements of Balmer Decrements and the Dust Attenuation Curve at Redshifts z $\sim$ 1.4-2.6". In: *ApJ* 806.2, 259, p. 259. DOI: 10.1088/0004-637X/806/2/259. arXiv: 1504.02782 [astro-ph.GA].

Rivera-Thorsen, Thøger E. et al. (May 2015). "The Lyman Alpha Reference Sample. V. The Impact of Neutral ISM Kinematics and Geometry on Ly$\alpha$ Escape". In: *ApJ* 805.1, 14, p. 14. DOI: 10.1088/0004-637X/805/1/14. arXiv: 1503.01157 [astro-ph.GA].

Rix, S. A. et al. (Nov. 2004). "Spectral Modeling of Star-forming Regions in the Ultraviolet: Stellar Metallicity Diagnostics for High-Redshift Galaxies". In: *ApJ* 615, pp. 98–117. DOI: 10.1086/424031. eprint: astro-ph/0407296.

Rudie, Gwen C. et al. (May 2012). "The Gaseous Environment of High-z Galaxies: Precision Measurements of Neutral Hydrogen in the Circumgalactic Medium of z $\sim$ 2-3 Galaxies in the Keck Baryonic Structure Survey". In: *ApJ* 750.1, 67, p. 67. DOI: 10.1088/0004-637X/750/1/67. arXiv: 1202.6055 [astro-ph.CO].

Rupke, David S., Sylvain Veilleux, and D. B. Sanders (Sept. 2005). "Outflows in Infrared-Luminous Starbursts at z < 0.5. II. Analysis and Discussion". In: *ApJS* 160.1, pp. 115–148. DOI: 10.1086/432889. arXiv: astro-ph/0506611 [astro-ph].

Sana, H. et al. (July 2012). "Binary Interaction Dominates the Evolution of Massive Stars". In: *Science* 337, p. 444. DOI: 10.1126/science.1223344. arXiv: 1207.6397 [astro-ph.SR].

Sanders, Ryan L. et al. (Jan. 2016). "The MOSDEF Survey: Electron Density and Ionization Parameter at z ∼ 2.3". In: *ApJ* 816.1, 23, p. 23. DOI: 10.3847/0004-637X/816/1/23. arXiv: 1509.03636 [astro-ph.GA].

Scarlata, C. and N. Panagia (Mar. 2015). "A Semi-analytical Line Transfer Model to Interpret the Spectra of Galaxy Outflows". In: *ApJ* 801.1, 43, p. 43. DOI: 10.1088/0004-637X/801/1/43. arXiv: 1501.07282 [astro-ph.GA].

Seaton, M. J. (June 1979). "Interstellar extinction in the UV". In: *MNRAS* 187, 73P–76P. DOI: 10.1093/mnras/187.1.73P.

Shapiro, Kristen L. et al. (Aug. 2009). "The SINS Survey: Broad Emission Lines in High-Redshift Star-Forming Galaxies". In: *ApJ* 701.2, pp. 955–963. DOI: 10.1088/0004-637X/701/2/955. arXiv: 0902.4704 [astro-ph.CO].

Shapley, Alice E. et al. (May 2003). "Rest-Frame Ultraviolet Spectra of z∼3 Lyman Break Galaxies". In: *ApJ* 588.1, pp. 65–89. DOI: 10.1086/373922. arXiv: astro-ph/0301230 [astro-ph].

Shapley, Alice E. et al. (June 2005). "Ultraviolet to Mid-Infrared Observations of Star-forming Galaxies at z∼2: Stellar Masses and Stellar Populations". In: *ApJ* 626.2, pp. 698–722. DOI: 10.1086/429990. arXiv: astro-ph/0503485 [astro-ph].

Shapley, Alice E. et al. (Mar. 2015). "The MOSDEF Survey: Excitation Properties of z 2.3 Star-forming Galaxies". In: *ApJ* 801.2, 88, p. 88. DOI: 10.1088/0004-637X/801/2/88. arXiv: 1409.7071 [astro-ph.GA].

Shivaei, Irene et al. (Apr. 2016). "The MOSDEF Survey: The Strong Agreement between H$\alpha$ and UV-to-FIR Star Formation Rates for z ∼ 2 Star-forming Galaxies". In: *ApJL* 820.2, L23, p. L23. DOI: 10.3847/2041-8205/820/2/L23. arXiv: 1603.02284 [astro-ph.GA].

Shivaei, Irene et al. (Mar. 2017). "The MOSDEF Survey: Metallicity Dependence of PAH Emission at High Redshift and Implications for 24 $\mu$m Inferred IR Luminosities and Star Formation Rates at z∼2". In: *ApJ* 837.2, 157, p. 157. DOI: 10.3847/1538-4357/aa619c. arXiv: 1609.04814 [astro-ph.GA].

Shopbell, P. L. and J. Bland-Hawthorn (Jan. 1998). "The Asymmetric Wind in M82". In: *ApJ* 493.1, pp. 129–153. DOI: 10.1086/305108. arXiv: astro-ph/9708038 [astro-ph].

Smit, Renske et al. (Dec. 2016). "Inferred H$\alpha$ Flux as a Star Formation Rate Indicator at z $\sim$ 4-5: Implications for Dust Properties, Burstiness, and the z = 4-8 Star Formation Rate Functions". In: *ApJ* 833.2, 254, p. 254. DOI: 10.3847/1538-4357/833/2/254. arXiv: 1511.08808 [astro-ph.GA].

Somerville, Rachel S. and Joel R. Primack (Dec. 1999). "Semi-analytic modelling of galaxy formation: the local Universe". In: *MNRAS* 310.4, pp. 1087–1110. DOI: 10.1046/j.1365-8711.1999.03032.x. arXiv: astro-ph/9802268 [astro-ph].

Sparre, M. et al. (Apr. 2017). "(Star)bursts of FIRE: observational signatures of bursty star formation in galaxies". In: *MNRAS* 466, pp. 88–104. DOI: 10.1093/mnras/stw3011. arXiv: 1510.03869.

Stanway, E. R. and J. J. Eldridge (Sept. 2018). "Re-evaluating old stellar populations". In: *MNRAS* 479, pp. 75–93. DOI: 10.1093/mnras/sty1353. arXiv: 1805.08784.

Steidel, C. C. et al. (Aug. 2016). "Reconciling the Stellar and Nebular Spectra of High-redshift Galaxies". In: *ApJ* 826, 159, p. 159. DOI: 10.3847/0004-637X/826/2/159. arXiv: 1605.07186.

Steidel, Charles C. et al. (Apr. 2004). "A Survey of Star-forming Galaxies in the 1.4$\lesssim$z$\lesssim$2.5 Redshift Desert: Overview". In: *ApJ* 604.2, pp. 534–550. DOI: 10.1086/381960. arXiv: astro-ph/0401439 [astro-ph].

Steidel, Charles C. et al. (July 2010). "The Structure and Kinematics of the Circumgalactic Medium from Far-ultraviolet Spectra of z $\sim$ 2-3 Galaxies". In: *ApJ* 717.1, pp. 289–322. DOI: 10.1088/0004-637X/717/1/289. arXiv: 1003.0679 [astro-ph.CO].

Steidel, Charles C. et al. (Nov. 2014). "Strong Nebular Line Ratios in the Spectra of z $\sim$ 2-3 Star Forming Galaxies: First Results from KBSS-MOSFIRE". In: *ApJ* 795.2, 165, p. 165. DOI: 10.1088/0004-637X/795/2/165. arXiv: 1405.5473 [astro-ph.GA].

Steidel, Charles C. et al. (Dec. 2018). "The Keck Lyman Continuum Spectroscopic Survey (KLCS): The Emergent Ionizing Spectrum of Galaxies at z 3". In: *ApJ* 869.2, 123, p. 123. DOI: 10.3847/1538-4357/aaed28. arXiv: 1805.06071 [astro-ph.GA].

Strickland, David K. and Timothy M. Heckman (Mar. 2007). "Iron Line and Diffuse Hard X-Ray Emission from the Starburst Galaxy M82". In: *ApJ* 658.1, pp. 258–281. DOI: 10.1086/511174. arXiv: astro-ph/0611859 [astro-ph].

Strickland, David K. et al. (Apr. 2004). "A High Spatial Resolution X-Ray and H$\alpha$ Study of Hot Gas in the Halos of Star-forming Disk Galaxies. I. Spatial and Spectral Properties of the Diffuse X-Ray Emission". In: *ApJS* 151.2, pp. 193–236. DOI: 10.1086/382214. arXiv: astro-ph/0306592 [astro-ph].

Strom, Allison L. et al. (Feb. 2017). "Nebular Emission Line Ratios in z ∼ 2-3 Star-forming Galaxies with KBSS-MOSFIRE: Exploring the Impact of Ionization, Excitation, and Nitrogen-to-Oxygen Ratio". In: *ApJ* 836.2, 164, p. 164. DOI: 10.3847/1538-4357/836/2/164. arXiv: 1608.02587 [astro-ph.GA].

Strom, Allison L. et al. (Dec. 2018). "Measuring the Physical Conditions in High-redshift Star-forming Galaxies: Insights from KBSS-MOSFIRE". In: *ApJ* 868.2, 117, p. 117. DOI: 10.3847/1538-4357/aae1a5. arXiv: 1711.08820 [astro-ph.GA].

Tacconi, L. J. et al. (Feb. 2010). "High molecular gas fractions in normal massive star-forming galaxies in the young Universe". In: *Nature* 463, pp. 781–784. DOI: 10.1038/nature08773. arXiv: 1002.2149.

Tacconi, L. J. et al. (May 2013). "Phibss: Molecular Gas Content and Scaling Relations in z ∼1-3 Massive, Main-sequence Star-forming Galaxies". In: *ApJ* 768.1, 74, p. 74. DOI: 10.1088/0004-637X/768/1/74. arXiv: 1211.5743 [astro-ph.CO].

Theios, R. L. et al. (Jan. 2019). "Dust Attenuation, Star Formation, and Metallicity in z ∼ 2-3 Galaxies from KBSS-MOSFIRE". In: *ApJ* 871, 128, p. 128. DOI: 10.3847/1538-4357/aaf386. arXiv: 1805.00016.

Theios, R. L. et al. (2020). "Galactic Outflows in z ∼ 2-3 Galaxies from KBSS-MOSFIRE". (in preparation).

Topping, Michael W. et al. (Dec. 2019). "The MOSDEF-LRIS Survey: The Interplay Between Massive Stars and Ionized Gas in High-Redshift Star-Forming Galaxies". In: *arXiv e-prints*, arXiv:1912.10243, arXiv:1912.10243. arXiv: 1912.10243 [astro-ph.GA].

Trainor, Ryan F. et al. (Aug. 2015). "The Spectroscopic Properties of Ly$\alpha$-Emitters at z∼2.7: Escaping Gas and Photons from Faint Galaxies". In: *ApJ* 809.1, 89, p. 89. DOI: 10.1088/0004-637X/809/1/89. arXiv: 1506.08205 [astro-ph.GA].

Tremonti, Christy A. et al. (Oct. 2004). "The Origin of the Mass-Metallicity Relation: Insights from 53,000 Star-forming Galaxies in the Sloan Digital Sky Survey". In: *ApJ* 613.2, pp. 898–913. DOI: 10.1086/423264. arXiv: astro-ph/0405537 [astro-ph].

Veilleux, Sylvain, Gerald Cecil, and Joss Bland-Hawthorn (Sept. 2005). "Galactic Winds". In: *ARA&A* 43.1, pp. 769–826. DOI: 10.1146/annurev.astro.43.072103.150610. arXiv: astro-ph/0504435 [astro-ph].

Veilleux, Sylvain and Donald E. Osterbrock (Feb. 1987). "Spectral Classification of Emission-Line Galaxies". In: *ApJS* 63, p. 295. DOI: 10.1086/191166.

Weiner, B. J. et al. (Feb. 2009). "Ubiquitous Outflows in DEEP2 Spectra of Star-Forming Galaxies at z = 1.4". In: *ApJ* 692, pp. 187–211. DOI: 10.1088/0004-637X/692/1/187. arXiv: 0804.4686.

Weisz, Daniel R. et al. (Jan. 2012). "Modeling the Effects of Star Formation Histories on H$\alpha$ and Ultraviolet Fluxes in nearby Dwarf Galaxies". In: *ApJ* 744.1, 44, p. 44. DOI: 10.1088/0004-637X/744/1/44. arXiv: 1109.2905 [astro-ph.CO].

Williams, Christina C. et al. (Feb. 2015). "The Interstellar Medium and Feedback in the Progenitors of the Compact Passive Galaxies at z $\sim$2". In: *ApJ* 800.1, 21, p. 21. DOI: 10.1088/0004-637X/800/1/21. arXiv: 1407.1834 [astro-ph.GA].

Wood, Corey M. et al. (Sept. 2015). "Supernova-driven outflows in NGC 7552: a comparison of H $\alpha$ and UV tracers". In: *MNRAS* 452.3, pp. 2712–2730. DOI: 10.1093/mnras/stv1471. arXiv: 1507.00346 [astro-ph.GA].

Zahid, H. J., L. J. Kewley, and F. Bresolin (Apr. 2011). "The Mass-Metallicity and Luminosity-Metallicity Relations from DEEP2 at z $\sim$ 0.8". In: *ApJ* 730.2, 137, p. 137. DOI: 10.1088/0004-637X/730/2/137. arXiv: 1006.4877 [astro-ph.CO].